Dual-Band Planar Wide-Angle Scanning Phased Arrays

Dual-Band Planar Wide-Angle Scanning Phased Arrays

Proefschrift

ter verkrijging van de graad van doctor
aan de Technische Universiteit Delft,
op gezag van de Rector Magnificus prof.ir. K.C.A.M. Luyben,
voorzitter van het College voor Promoties,
in het openbaar te verdedigen op 7 mei 2014 om 12:30 uur

door

Shenario Ezhil Valavan

Master of Science (Electrical Engineering)

geboren te Madras, India.

Dit proefschrift is goedgekeurd door de promotor:
Prof. DSc. A. G. Yarovoy

Samenstelling promotiecomissie:

Rector Magnificus,	voorzitter
Prof. DSc. A. G. Yarovoy,	Technische Universiteit Delft, promotor
Prof. F. Le Chevalier,	Technische Universiteit Delft
Prof. Ir. P. van Genderen,	Technische Universiteit Delft
Prof. Dr. A. Neto,	Technische Universiteit Delft
Prof. Ir. P. Hoogeboom,	Technische Universiteit Delft
Prof. Dr. Ir. B. Smolders,	Technische Universiteit Eindhoven
Prof. Dr. Ir. G. Vandenbosch,	Katholieke Universiteit Leuven

This research was supported by Sensor Technology Applied in Reconfigurable systems for sustainable Security (STARS) project.

ISBN: 978-94-6259-142-4
Dual-Band Planar Wide-Angle Scanning Phased Arrays
PhD Dissertation, Delft University of Technology.

Cover Design by Amudhan Ignatius.

Author e-mail: shenario1@gmail.com

To Sathya and Josphine Amma ....

Contents

List of Figures

List of Tables

Chapter 1

Introduction

1.1 Overview and motivation

The field of radar has seen phenomenal developments during the past two decades, especially with the advent of high performance computing and rapid progress in the solid-state and digital signal processing domain [1]. These advancements have facilitated in endeavours primarily aimed at increasing the functional capabilities of these radar systems. Enhancing the system's capability to support traditional radar, as well as communication and navigation features, has led to the concept of multifunction radars, which serve as advanced and sophisticated systems catering to various functional needs. Of late, the research on the development of reconfigurable multifunction radars has generated a large interest in both industry and academia. Several ongoing as well as recently completed research projects [2–8] have strongly reiterated this interest. The development of new system concepts capable of handling multiple functions, either simultaneously or sequentially, without compromising the system's quality-of-service for individual target functions, has been the prime focus in most of these high-profile projects. Furthermore, multifunction wireless systems reduce the need to depend on several systems each focussing on a single operational capability. The integrated mast or *'i-mast'* concept [9], developed by Thales, is one such system, which serves as an example of a modern and functional multifunction radar (primarily used for naval applications). Different functions are realized by different physical front-ends, catering to a variety of surveillance, tracking and communication oriented needs. Integration of various wireless systems and sharing physical radiating apertures between different functions presents a principal way to further multifunction radar and communication system development.

Radar systems can, in principle, be reconfigured in terms of functional tasks or functional modes. For example, reconfigurable radars combining the functional tasks of weather surveillance and air traffic control (ATC) [3], are envisioned as a promising idea, wherein a single sensor system, apart from serving ATC purposes, can also carry out weather monitoring, useful for both local and nation-wide meteorology. Reconfiguration with respect to different functional modes, for instance, switching between tracking (with pencil beam), and search scan (involving fan-beams), can also be implemented with the same aperture. A schematic representation of a reconfigurable radar front-end with multifunction capability is shown in Fig. 1.1.

Antenna array front-ends form a pivotal part in all multifunction radar systems for the transmission and reception of signals of interest, based on which information processing is carried out [10]. The reconfigurable antenna arrays required for these systems are traditionally termed as 'smart' antennas, which primarily refers to the various ways in which the antenna can be reconfigured, for instance operational bands, bandwidth, beam-width, polarisation, scanning directions, multiple beams etc., all of which can be directly translated into many system level functions.

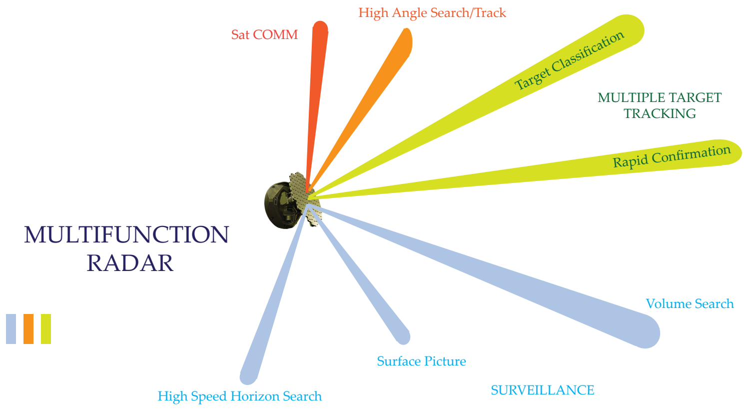

Figure 1.1: Reconfigurable radar front-end with multifunction capability. Colour labels refer to different operational frequencies.

In this dissertation, the primary focus is with the development of multi-frequency phased arrays, specifically, dual-band phased arrays, with wide-angle beamforming capability. The frequency reconfiguration capability of the array is functionally both attractive and useful. The ability of the array to operate in and switch faster between different operational bands (possibly with different instantaneous bandwidths), spread over large frequency ratios, provides an extra edge over traditional single-band systems with regard to ESM/ECM features. On the other hand, wide-angle scanning or beamforming is pivotal for modern radar applications, as it not only enables the system to have a wider field-of-view, but also helps in maximising the advantages offered by digital beamforming (DBF) techniques. For example, the stacked or multibeam capability, along with wide-angle scanning capabilities can help in achieving advanced features like multiple-target tracking over wide coverage areas, aspects vital for multifunction radars. Furthermore, functional tasks requiring different types of beams (for example, surveillance and tracking), in most cases are executed in different operational bands, which reiterates the inter-relationship between and need to have both frequency and beamforming agility. Thus frequency reconfigurable widescan phased arrays are ideally suited for application in future multifunction radars, providing strong performance advantages.

1.1.1 State-of-the-art review on frequency agile antenna arrays

Several approaches, with different concept maturity levels, aimed at achieving frequency and wide-angle beamforming agility have been proposed over the last decade. Some of the main approaches are summarised in the following paragraphs.

Firstly, the use of ultra-wideband (UWB) antenna arrays, mostly with the use of either Vivaldi antennas [11–16] or connected dipole arrays [17–27], are prescribed for large frequency range coverage encompassing many operational bands. Frequency ratios between 3:1 and 10:1 have been proposed as possible targets for these arrays [11,13,20]. However, these ultra-wideband arrays require highly precise filters in order to effectively filter out the out-of-band signals when operating and switching between different sub-bands. Further, the ultra-wideband antenna elements require excellent phase characteristics to provide optimum performances. Many of the ultra-wideband array concepts also have limits with respect to scanning capability, the performance of which require considerable improvements. These operational challenges need further refinement for implementation in practical systems.

The next approach, proposed very recently, is with the use of layered array architectures [28, 29], which aim to achieve frequency agility with the use of arrays separated in layers with different operational bands. Apart from increasing the complexity of the feeding configurations, these proposals also have serious limitations with respect to scanning capabilities [28]. Nevertheless, these could be considered as possible candidates for applications like airborne SAR.

The third approach is the shared aperture or interleaved array approach [30–35], which involves the use of different radiator sets distributed aperiodically over the same aperture, with each set functioning in different operational frequencies. However, the aperiodic distribution of elements results in limited scanning performance [32, 33] as well as making it impractical to achieve modular array architectures. Furthermore, the sparse distributions also results in high sidelobe levels, another performance drawback of the shared aperture concept. Satellite arrays with switched beams and radio astronomy are possible areas of application for this concept.

Finally, an approach, which involves the use of external switches, is the so-called arrays with 'super-elements' [36–38]. Frequency agility is achieved by reconfiguring the radiator sizes with the use of diode switches placed in between radiator elements, which are turned on/off as per requirements. The use of external circuits in the design poses major limitations for the deployment of these arrays, as the impacts of the circuitry on the array performance are non-trivial. Besides, the scanning performances of these arrays are also limited [36]. Furthermore, the interleaved arrays and arrays with 'super-elements' concepts are laboratory solutions, with concept maturity levels still in their infancy.

With this background on the state-of-the-art on multi-frequency and ultra-wideband phased arrays, the development of dual-band phased arrays with large frequency ratios and wide-angle beamforming capability was selected as the main goal for the thesis research. The use of dual- or multi-band arrays, as compared to ultra-wideband arrays, is advantageous, in that, part of the filtering process can be transferred to the antenna element itself, thereby relaxing the requirements on the RF back-end components in terms of efficiency as well as avoid interference problems due to out-of-band signals.

The key specifics and motivation for the research scheme are as follows. Patch antennas were chosen for their attractiveness and suitability for the development of planar and conformal array architectures. Many of the dual- or multi-band antennas proposed for arrays [39–48] suffer from one of three major performance limitations viz., non-symmetric radiation patterns [40], narrow sub-band bandwidths and large electrical dimensions, especially at the high frequency band of operation [42]. Designs, similar to [39,44,46], have large electrical dimensions, especially at the high frequency band, making them unsuitable for array applications. The performances of other dual- or multi-band antennas [40, 42, 43, 45, 47], which are prescribed specifically as array elements, do not demonstrate convincing performances in arrays, with many designs seldom illustrating embedded patterns or scanning performances (in arrays) in the respective articles. The u-slot antennas [40, 47], in particular, are virtually non-functional in arrays, with large electrical dimensions and inconsistent radiation patterns. Many variants of this antenna also lack design regularity when used to achieve dual- or tri-band operations. Further, the multi-band antennas also need to support good bandwidths at the operational bands. Slot-loaded patch antenna designs with consistent radiation patterns and electrical dimensions, similar to [41,42,46,48], support extremely narrow sub-band bandwidths. Large shifts in the bands' position become evident when scanned off broadside. Thus, it is vital to demonstrate the performances of the dual-band patch antennas developed in both stand-alone and array configurations. In addition to this, the array antennas need to support frequency ratios between 1.5:1 and 2:1, as it can help in covering different target bands of practical interest and importance (for eg, L/S-bands or X/Ku-bands).Although, larger frequency ratios (between 3:1 and 10:1) are proposed with ultra-wideband antenna solutions, the scope of the research in this thesis is limited to dual-band patch antenna arrays targeting frequency ratios between 1.5:1 to 2:1.

Secondly, wide-angle scanning up to a maximum of $\pm 60^o$, along the principal planes of interest, needs to be supported at both the operational bands. This scanning range provides the possibility to support full-azimuthal coverage, as achieved with the four-face *'i-mast'* structure [9].

Thirdly, the use of dual-band patch antennas in arrays with regular dense grids would require the maintenance of optimal inter-element spacing at both the operational bands. In this regard, very small inter-element spacing results at the low frequency band, if frequency ratios greater than 1.5:1, as targeted in the research, are considered. The maintenance of low levels of mutual coupling between array elements is hence pivotal to support embedded element performance and wide-angle scanning. The design and development of dual-band wide-scanning phased arrays hence forms a multilevel problem, with the major research targets as presented above.

Finally, it is worthwhile to discuss the current state-of-the-art in dual-band wide-scanning phased arrays briefly before proceeding further. As previously mentioned, the most important aspect of array is with the performance of the antenna in array. Although few designs, similar to the u-slot antennas, have been implemented in arrays, these cases often have large inter-element spacing between elements and do not demonstrate any scanning performances off-broadside, typically ranging between $10^o - 20^o$. Other slot-loaded elements, including the dual-slit and e-slot antennas, have extremely narrow sub-bands (50-70 MHz in each sub-band). Although, larger sub-band bandwidth (200-500 MHz) have been demonstrated with u-slot elements, the bandwidth are drastically reduced when ascertained with respect to the scanning angle off-broadside. Finally, the frequency ratios supported are also limited to the range of 1.1:1-1.2:1, for the majority of the currently existing dual- or multi-band antenna solutions. Few variants of the u-slot antenna [40] have improved frequency ratio of up to 1.3:1, but, the large electrical dimensions of these elements, at the high frequency bands, as previously stated, drastically reduces the scanning capability. A summary of the existing dual- or multi-band antenna solutions is presented in Table 1.1 (Electrical size is defined in terms of wavelength λ_H at the highest operational band).

The thesis research and its outputs, which resulted in dual-band phased array concepts, henceforth, represent one of the first successful demonstrations of dual-band arrays with large frequency ratios and wide-angle beamforming capability. The 'array-capable' characteristics of the dual-band antenna concepts, along with wide-angle impedance matching and beamforming agility, define a new benchmark in the domain of dual- or multi-band antenna arrays.

Table 1.1: Performance summary of the major existing multi-band antennas

Antenna	**Sub-band bandwidth**	**Electrical size**	**Frequency ratio**	**Radiation patterns**
U-slot antennas	100-500 MHz	$0.6\lambda_H$-$0.75\lambda_H$	1.2-1.7:1	Tilted patterns due to slot asymmetry
Dual-slot antennas	40-60 MHz	$0.5\lambda_H$-$0.7\lambda_H$	1.5-2:1	Consistent patterns
E-slot antennas	50-100 MHz	$0.6\lambda_H$-$0.75\lambda_H$	1.2-1.5:1	Tilted patterns due to slot asymmetry
Symmetric-slot and circular-slot antennas	50-100 MHz	$0.6\lambda_H$-$0.8\lambda_H$	1.2-1.6:1	Consistent, but sometimes with high cross polarisation levels

1.1.2 Research framework

The thesis research was carried out within the framework of the ongoing *STARS* project [8], which aims to develop concepts and technologies for defining the future in the domain of networked multifunction sensor systems, with a special emphasis on the reconfigurable capabilities of the associated systems and sub-systems. Various degrees of possible reconfigurable features for the array were explored during the course of the research striving to define new concepts and techniques to achieve array reconfigurability. Antenna array research within this framework encompasses the a) investigation of possible set of features which could be effectively combined or reconfigured, b) development of new concepts and designs for implementing these features, c) performance optimisation and d) proof-of-concept demonstrations using simulator and experimental prototypes, all of which have been successfully carried out during this doctoral research.

1.2 Research objectives and challenges

The research in the domain of dual-band arrays is still in its infancy, which in turn leads to several new challenges as well as opportunities for providing novel solutions to achieve array-level reconfigurability. The major research objectives, addressed in this thesis, can be broadly classified into two main tasks 1) the design and development of dual-band wide-angle scanning phased arrays with large frequency ratios (1.5:1 to 2:1), sub-band bandwidths greater than 100 MHz and wide-angle scanning up to $\pm 60^o$ along the principal planes, and 2) investigation and development of technique to reduce mutual coupling between radiators in these arrays, which inevitably, due to the large frequency ratio, leads to very small inter-element spacing, especially at the low frequency band of operation. In this regard, the key research problems or challenges addressed are elucidated in this subsection. The interrelation existent between these challenges reiterate the complex nature of this multilevel research and development problem.

- The development of a methodology for the analysis of the scanning performance of arrays with dual-band radiators in dense grid arrangements forms the first of the major challenges. In order to develop dual-band array-capable antennas, it becomes important to derive the inter-relation between the antenna dimensions, mutual coupling and frequency ratios. The methodology of the analysis should be capable of taking into account the different metrics of interest and also be representative and generic enough, such that the results are applicable to the design of antenna arrays with similar dual-band radiators and array architectures. Further, a specific focus on dual-band array radiators is required as the results of similar analysis with wideband radiators cannot be directly extrapolated for application in dual-band arrays.

- Secondly, employing dual-band antenna elements in regular dense grid arrangements would, by virtue of the large frequency ratios, result in very close inter-element spacing, particularly at the low frequency band of operation. Therefore, the analysis of the impact of mutual coupling on scanning performance and development of technique(s) to mitigate mutual coupling collectively served as another major research challenge. The techniques developed should be capable of reducing mutual coupling without introducing external structures (like EBGs) and jeopardising the scanning performance, either of which are the major limitations of many existing solutions [49–51].

- The design of array-capable antenna elements constitutes the next major research challenge. The dual-band antenna needs to have electrical dimensions suitable for supporting wide-angle scanning at all sub-bands, good sub-band bandwidths, large frequency ratio ($FR \geq 1.5:1$) and consistent radiation patterns. Therefore, the development of antenna elements with the aforementioned characteristics was a substantial challenge addressed in the research.

- The task of developing a single array architecture with frequency agility is highly challenging, particularly with the inclusion of the wide-scan capability in all the sub-bands. Hence, the fourth major challenge was the development and experimental validation of linear and planar dual-band arrays with wide-scan ($\pm 60\,^{\circ}$) beamforming capability. Antenna array architectures developed should also be scalable over a wide range of operational bands, maintaining similar levels of performance. This in turn necessitates the performance validation of the proposed designs in different bands, for instance dual-band arrays in X-band or L/S-bands. Associated analyses on the impact of the grid types and truncation on the performance of finite-sized arrays, in both the operational sub-bands, also form part of this challenge, due to the large frequency ratios considered.

- Finally, the exploration of possible extension of the antenna concepts for the development of multi-band antennas for SatComm applications, completes the set of research challenges addressed.

1.3 Research approach

Since the problem undertaken includes multilevel challenges, the research was hence compartmentalised as 1) analysis of mutual coupling characteristics and development of a non-invasive technique to reduce mutual coupling between array elements, 2) design and development of dual-band antenna concepts and 3) development of experimental prototypes for concept demonstration. The major steps in the research approaches and the associated novelty are presented below.

- Analyses on the influence of the antenna and array parameters (dimensions, substrate properties etc,.) on the performance of both finite and infinite arrays with wideband radiators [52–54] including printed dipoles and Vivaldi antennas, and rectangular microstrip and stacked patch antennas [55–57] are available in literature. However, similar analyses for dual- or multi-band patch antenna arrays are currently, to the best of our knowledge, absent. In this regard, the analysis of the scanning characteristics at the operational sub-bands and the evaluation of the impact of coupling on scanning formed an essential first step in the array research. The large frequency ratios targeted (between 1.5:1 and 2:1), along with the array modularity requirements, which necessitate the use of regular dense grids, result in very small inter-element spacing, especially at the low frequency band of operation. This, in turn, requires the need to properly understand and capture the differences in scanning performance at both the operational sub-bands, as the radiation patterns, inter-element spacing and impact of mutual coupling on scanning varies between the operational sub-bands. A systematic investigation of the scanning performance, including mutual coupling, of linear dual-band patch antenna arrays with full-wave numerical simulations was hence carried out. The main goal of this research step was to obtain useful insights into the scanning limits and impact of mutual coupling on scanning performance of the arrays, for the design and development of the dual-band antenna and array prototypes. The array performance metrics considered in the analysis are related to the dual-band frequency ratio with respect to different radiator dimensions, dielectric permittivity and substrate thickness. Furthermore, the scanning performances were to be quantified separately for E-plane and H-plane dual-band arrays.

- As the scanning performance of an array depends highly on the mutual coupling between the array elements, the next logical step in research was focussed on the development of coupling reduction techniques. Reduction of mutual coupling through the use of electromagnetic band gap (EBG) structures [51, 58], frequency selective surfaces (FSS) [50] and ground slits [49, 59], have been proposed in literature to suppress propagation of surface waves. These techniques however, have severe performance limitations and, in most cases, increase the fabrication complexity as well. The use of electromagnetic band gap (EBG) and frequency selective surface (FSS) structures in between radiators, to reduce coupling, inevitably increases the inter-element spacing, whereby the scanning capability of the arrays employing these structures are severely compromised. On the other hand, techniques that involve the use of ground slits ([49,59]) have serious limitations in practical array applications as the presence of the slits in the ground planes increase the backward radiation, which, in turn, would pose serious integration problems for the electronic components behind the radiator elements. This hence necessitates the development of a new technique to reduce mutual coupling between closely-spaced $(0.3\lambda - 0.5\lambda)$ patch antennas in array. Furthermore, the technique should also retain the scanning capability of the array. The technique's effectiveness has to be investigated both theoretically and experimentally with the use of linear arrays.

- The next step in the research was the development of dual-band antenna elements with low-profile electrical dimensions, suitable for supporting wide-angle scanning in arrays. Reduction of the antenna unit-cell's electrical dimensions at the lowest operational frequency and providing sufficiently large operational bandwidths at both sub-bands were the most important design challenges addressed. In addition to this, the maintenance of consistent radiation patterns and wide-angle impedance matching characteristics were also key aspects of interest in the antenna design. To achieve these objectives, a novel approach to the design and development of dual-band antenna, which supports the combination of both electric and magnetic type radiators in a single element, has been proposed. Compared to the other well-known dual- or multi-band antennas [39–48], which primarily support only electric radiation characteristics, the proposed dual-band antenna simultaneously utilizes both the patch-band electric radiation characteristics and the slot-based magnetic radiation characteristics in the overall radiation mechanism. Finally, in order to excite and support the electric and magnetic radiation characteristics, a novel feeding apparatus had to be developed.

- An alternative approach to the design of dual- or multi-band antenna, considered in the thesis, was the use of bended radiating elements. The approach can result in the creation of multi-resonant structure in a single antenna element, whereby, multiple current propagation paths can be accommodated in the same structure. This design approach was used for the development of an antenna element, capable of supporting a maximum of four operational sub-bands. With the use of bended planar structures, it is possible to increase the electrical dimensions at the low frequency band, without increasing the unit-cell size of the antenna. The development of dual-band antenna with extremely small unit-cell dimensions was carried out as the first step. Next, as with the previous antenna element, the performance evaluation and optimisation in arrays had to be carried out. Due to the use of bended planar structures, capable of being excited with pin feed, it is also possible to achieve simple antenna architectures.

- Finally, both the above mentioned dual-band antenna elements, by virtue of their low-profile architectures, were used for the development of dual-band phased array demonstrators in the X-, X/Ku and the K-bands. Wide-angle beamforming up to a maximum of $\pm 50^o - 60^o$ was targeted in all these cases. Numerical analysis of the performance of the dual-band arrays was carried out as the first step. The development of experimental demonstrators was foreseen for both linear and planar arrays, forming the next step in this research block. Coupling and scanning performance were investigated in these arrays. In addition to this, analysis on the array size sufficient to demonstrate the array performance were also carried out.

1.4 Organisation of the thesis

The remainder of this dissertation is organised as follows:

Chapter 2 presents the results of the systematic investigation of the scanning performance, with the inclusion of mutual coupling, of arrays with dual-band patch antennas. The investigation carried out evaluates the realised gain and radiation patterns, and relates scanning performance of the array to the dual-band frequency ratio with respect to different radiator dimensions, dielectric permittivity and substrate thickness.

The development of the dielectric-contrast technique for mitigating mutual coupling between array radiators is described in Chapter 3. The modal characteristics based evaluation is also used to provide insights into the difference in surface-wave phenomena between homogeneous and the proposed multilayer substrate architectures. The experimental verification of the effectiveness of the proposed technique is also provided.

Chapter 4 presents the development of dual-band phased arrays in L/S and X-bands. The first part of the chapter presents the design concepts of the dual-band comb-slot-loaded array antenna. A special emphasis is given to the description of the quasi-magneto-electric radiation characteristics and the antenna's novel feeding architecture, which helps in enhancing the bandwidths at the operational bands. The second part of the chapter focuses on the development and experimental validation of prototype demonstrators of linear and planar dual-band phased arrays, operational in the X-band, with large frequency ratio (nearly 1.5:1) and wide-scan capability.

The development of the novel multi-band crossed L-bar antenna forms the core focus of Chapter 5. Dual-band phased arrays with larger frequency ratios ($\geq 1.8 : 1$), with the dual-band version of the crossed L-bar antenna have been developed . The array design also has two variants, with one variant operational in the X/Ku-bands, and the other in the K-band. Detailed information on the antenna design and optimisation are described, following which the development of the dual-band prototypes operational in the above mentioned bands are presented. Experimental validation of both the stand-alone quad-band antenna and the dual-band phased arrays are also provided.

Finally, the dissertation concludes with a summary of the major contributions of the research and prescriptions for future research topics in the domain of dual/multi-band phased array development and applications.

Chapter 2

Investigation of Scanning Performance of Dual-Band Patch Arrays

In this chapter, the systematic investigation of the scanning performance, including mutual coupling, of linear dual-band patch antenna arrays is presented. The main goal of this research step was to obtain useful insights into the scanning limits and impact of mutual coupling on scanning performance of the arrays, for the design and development of the dual-band antenna and array prototypes. The array performance metrics considered in the analysis are related to the dual-band frequency ratio with respect to different radiator dimensions, dielectric permittivity and substrate thickness. Furthermore, the scanning performances have also been quantified separately for E-plane and H-plane arrays. The investigation was carried out using full-wave numerical simulations in CST-Microwave Studio (MWS) and the post-processing of the scanning performance was evaluated with a tailor-made Matlab script. It is worth mentioning, that the scope of the investigation was limited to linearly-polarised slot-loaded patches in arrays. Also, frequency ratios greater than an octave were not considered in the investigation. The approach used for the analysis, major results and discussions are described in the following sections of this chapter.

2.1 Research approach

The investigation approach consists of three main steps viz., the selection of suitable dual-band patch radiator, implementation of array models in full-wave solvers and post processing of the scanning performance of the array, each of which are summarised in the following subsections.

2.1.1 Dual-band reference antenna

The selection of the radiator element was pivotal for the investigation, in that the chosen antenna element should be generic enough, that results obtained can eventually be extended for the development of dual-band wide-scan phased arrays. The dual slot-loaded patch antenna (Fig. 2.1), proposed in [41], was used for the investigation. The slots, placed on either ends, along the length (L) of the patch, induce a modification of the surface current distribution on the patch by which symmetric radiation patterns, along both E- and H-planes, is achieved at the high frequency band of operation. Symmetric radiation pattern, similar to that obtained with a typical rectangular patch antenna, exists at the low frequency band of operation. Another attractive feature of this radiator is the possibility to tune the frequency ratio, between the two operational sub-bands, from 1.5:1 to a maximum of 1.9:1. This can be achieved by the careful optimisation of the slot's position and dimensions. Furthermore, dual-band characteristic can also be maintained for different dimensions of the patch, which made it possible to evaluate the scan performance with different antenna dimensions. The combination of all these attractive features served as the main driving factor for the choice of this dual slot-loaded radiator as the *'reference'* radiator for this investigation.

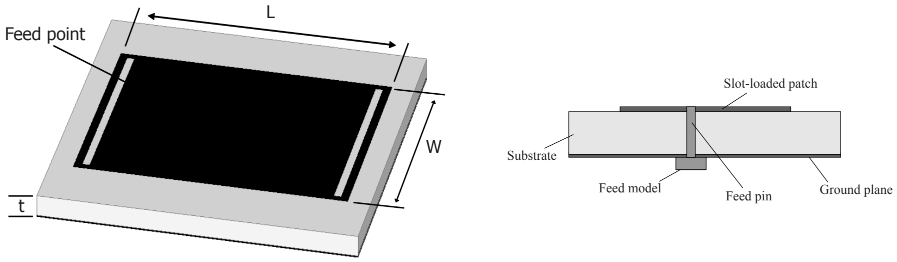

(a) (b)

Figure 2.1: (a)- Dual slot-loaded dual-band patch antenna. L - patch length, W - patch width, U_{cell} - unit-cell dimension and t - substrate thickness. E-plane(x-z) and H-plane(y-z). (b)- Side-view of the dual-band element.

In order to perform the parametric analysis, the radiator was retuned for all frequency ratios of interest between 1.5:1 and 2:1, with a step increment of 0.1. The dimensions of the array radiators were scaled in terms of wavelength (λ_L), with λ_L

defined at the low frequency band of operation (f_L). The step increments for both the length and width of the patch was set at $0.1\lambda_L$. An important metric is the ratio of the length to width (L/W) of the patch, which was maintained at around 1.3 for all the cases considered in the analysis, as this ratio ensures best possible symmetric radiation patterns at the high frequency of operation. Other ratios tend to 'tilt' the pattern's peak off boresight. Patch dimensions (L and W) less than or equal to $0.15\lambda_L$ were not considered in the analysis as it becomes extremely difficult to maintain dual-band operation and symmetric radiation patterns for all frequency ratios of interest with these dimensions. For the investigation carried out, the radiators with different frequency ratios and dimensions were individually optimised in CST-MWS, following which the radiators were implemented in E-plane (x-z plane in Fig. 2.1) and H-plane (y-z plane in Fig. 2.1) linear arrays in periodic arrangements replicating the unit-cell. In order to demonstrate the dual-band and symmetric radiation pattern characteristics of the *'reference'* antenna, the magnitude of the input reflection coefficient ($|\Gamma_{in}|$) characteristic of the individual radiator (39mm (L) × 30mm (W), $\epsilon_r = 2.33$, t = 3.04mm, unit-cell- 42mm × 42mm) supporting the maximum frequency ratio of 1.9:1 is shown in Fig. 2.2(a). The corresponding radiation patterns at both operational sub-bands ($f_L = 2.27$ GHz and $f_H = 4.3$ GHz) are presented in Fig. 2.2(b).

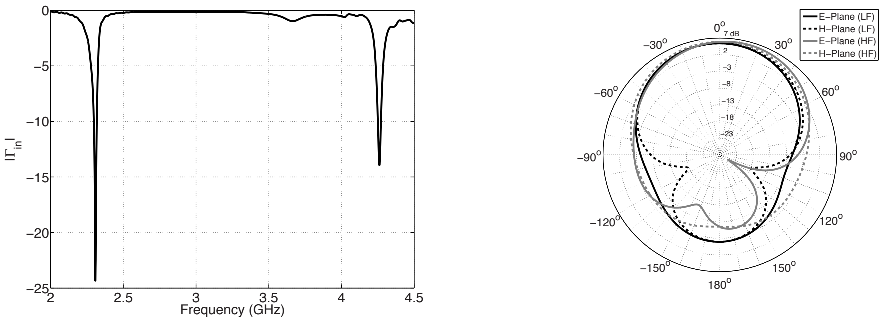

(a)

(b)

Figure 2.2: Dual slot-loaded dual-band antenna characteristics (FR = 1.9:1). (a) Input reflection coefficient and (b) Radiation patterns at operational sub-bands (2.27 GHz and 4.3 GHz).

2.1.2 Array modelling

The key aspects of the array modelling and evaluation of the scanning performance are summarised in this subsection. The radiator elements were modelled and implemented in finite arrays in CST-MWS to obtain the embedded patterns of the array elements and the scattering matrices. Finite array models were used for the investigation for capturing the impact of the edge elements on the radiation patterns of the array. In order to ensure that the results computed do not vary with array lengths, it becomes imperative to maintain array lengths which would appropriately take into account the behaviour of the edge elements and emulate large or infinite arrays as well. The sizes of the finite array models used for the analysis, were therefore finalised based on the truncation analysis on finite-sized arrays with dual-band radiators presented in [60]. Array lengths of $12\lambda_L$ and $10\lambda_L$ were used for the E-plane and H-plane arrays respectively, larger than the lengths prescribed in [60]. Furthermore, it was also verified that the use of array lengths larger than the ones mentioned above ($12\lambda_L$ and $10\lambda_L$) do not result in significant variation of the edge elements' behaviour and thereby the array performance. Schematic representations of sections of the linear arrays with the radiators oriented along their E- and H-planes are shown in Fig. 2.3. The center-to-center element spacing for the E-plane and H-plane arrays were

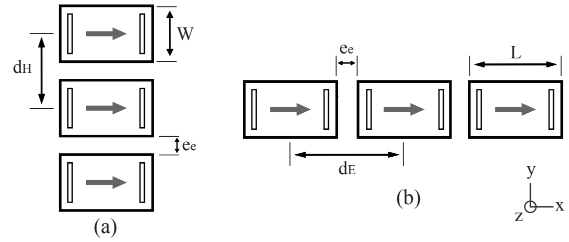

Figure 2.3: Schematic representation of section of linear array models with radiators oriented along their (a) H-plane and (b) E-plane. d_E and d_H represent the inter-element spacing for the E- and H-plane arrays respectively. e_e refers to edge-to-edge gap between adjacent radiators, and L and W the length and width of patch radiator. Arrowhead represents orientation of the E-plane.

maintained at $d_E \geq L + 0.11\lambda_L$ and $d_H \geq W + 0.11\lambda_L$, respectively for all radiator dimensions considered. The numerical value of $0.11\lambda_L$ represents the minimum edge-to-edge spacing (e_e) required between the radiators in order to preserve the dual-band characteristic. Having smaller edge-to-edge spacing (e_e) results in very high (> -8 dB) mutual coupling levels distorting the dual-band characteristic of the embedded array radiators.

The next key aspect deals with the evaluation of the array pattern. The procedure used for the computation of the array pattern in this analysis includes the effects of the mutual coupling and embedded patterns of the array elements, similar to the methods elucidated in [61–64]. The use of the embedded element pattern makes the analysis more realistic as compared to the case of using individual 'stand-alone' element patterns [64], as the impact of mutual coupling on the element pattern and thereby the array performance are taken into consideration. The array directivity pattern (G_{AR}) is evaluated using the following expression,

$$G_{AR}(\theta, \phi) = [A]^T [S][g] \tag{2.1}$$

Where $[g]$ refers to the matrix containing the embedded patterns of the individual elements in the array and $[S]$, the scattering matrices for respective arrays considered here, both of which were obtained from the full-wave solver. Matrix $[A]$ represents the excitation vector of the array. The i^{th} embedded pattern $g_i(\theta, \phi)$, represents the pattern obtained in CST-MWS by exciting the generic i^{th} element while terminating all the other array elements on matched loads. The excitation applied to the generic i^{th} element in the linear array is given by $A_i.e^{-j\theta_i}$, where $e^{-j\theta_i}$ represents the progressive phase shift applied at the i^{th} element for array scanning. The analysis presented focuses only on uniform linear arrays and hence the excitation amplitude A_i is identically equal to unity for all array elements. The scanning patterns of the array ($G_{AR}(\theta, \phi)$) for different angles were computed with a Matlab script based on equation (2.1), with the application of appropriate phase shifts.

The procedure used for the calculation of the scanning performance can be summarised based on the following steps. Firstly, for every patch dimension and frequency ratio, the patches with the respective specifications were modelled, optimised and implemented in linear array configurations in the full-wave solver. Following this, the $[g]$ matrix, representing the embedded pattern of the array elements, and the scattering matrices $[S]$ were computed for the respective E-plane or H-plane architectures. Thirdly, for the computation of the scanning performance, coupling between the adjacent radiators pairs after the second immediate pair was neglected, as coupling levels drop below -30 dB. In other words, for the calculation of the array pattern, the main coupling coefficients in the $[S]$ matrices was limited to the $S_{(i+1),i}, S_{(i+2),i}, S_{(i-1),i}$ and $S_{(i-2),i}$ terms (only two of the four terms will be accounted for edge elements), when considering the coupling terms for the generic i^{th} element. From the full-wave analysis, it was observed that the maximum coupling levels (at lowest operational band) between adjacent radiators were around -9.0 dB and -13.5 dB for the E-plane and H-plane arrays respectively.

The maximum scanning angle (θ_{max}) at the high frequency of operation was chosen as the metric for carrying out the comparative analysis. It (θ_{max}) refers to the angle at and above which the realised gain at the respective scanning angle ($G_r(\theta)$) equals or reduces to less than half of the realised gain expected from the ideal case $G_{ideal}(\theta)$, where ideal gain refers to the product of array factor and stand-alone radiator pattern (excluding mutual coupling).

$$\frac{G_r(\theta)}{G_{ideal}(\theta)} \leq 0.5 \tag{2.2}$$

Compared to the ideal case, the inclusion of the mutual coupling into the analysis would result in more power being spread in the side-lobes resulting in the deterioration of the main beam performance. The approach thus ensures the inclusion of the qualitative impact of the mutual coupling on scanning performance of the arrays. The main results of the investigation are summarised in the upcoming sections.

2.2 Results of the investigation

The results of the investigation with respect to each of the target metrics of interest are elucidated in this section. This is followed by a discussion on the insights gained through the analysis, whereby the major conclusions of this investigation are drawn out.

2.2.1 Radiator dimensions

The scanning performances of the E-plane and H-plane arrays are quantified based on the variation of the length (L) and width (W) of the patch respectively, due to the orientation (by definition) of the length and width of the patch along the E-plane and H-plane of the radiator (refer Fig. 2.1). As previously mentioned, the ratio of the patch length to width (L/W) was maintained around 1.3 for all cases presented. Substrates with dielectric permittivity $\epsilon_r = 2.33$ were used for this analysis. The variation of the maximum scanning angle (θ_{max}) for different lengths (L) and widths (W) of the patch at the high frequency of operation for the E-plane and H-plane arrays, with respect to the dual-band frequency ratio, are presented Figs. 2.4a and 2.4b respectively. The inter-element spacing for all cases presented in Fig. 2.4 were maintained at $d_E(or d_H) = L(or W) + 0.11\lambda_L$. Larger inter-element spacing were not considered as the main focus of the investigation resides with the analysis of dual-band arrays suitable for wide-angle scanning, which inevitably requires small inter-element spacing at the low frequency band of operation. Furthermore, the extrapolated scanning performance for frequency ratio of 2:1 (based on the performances for frequency ratios of 1.8:1 and 1.9:1) has been included in the plots for the sake of completeness in covering the range between 1.5:1 and 2:1. This frequency ratio however, was not supported with any of the radiator dimensions presented in the analysis. This is mainly because of the increase in the levels of coupling at the low frequency band, which consequently results in the destruction of the dual-band impedance matching when implemented in arrays.

From the plots presented, it can be inferred that the scanning performance of the H-plane array shows behaviour similar to the E-plane array, although θ_{max} at the high frequency of operation is slightly less affected. This can mainly be attributed to

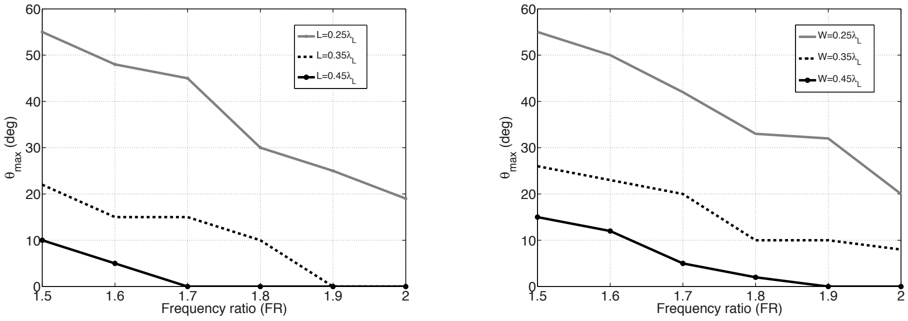

(a)

(b)

Figure 2.4: (a) Variation of θ_{max} with patch length (L), $d_E = L + 0.11\lambda_L$ (E-Plane). (b) Variation of θ_{max} with patch width (W), $d_H = W + 0.11\lambda_L$ (H-Plane).

the comparatively low levels of coupling between radiators arranged along their H-plane. Nevertheless, maintaining patch widths (W) less than or equal to $0.3\lambda_L$ is still essential, in order to achieve bigger scanning angles at the high frequency of operation with larger frequency ratios. The scanning performance of the array for the ideal case (excluding coupling) is shown in Fig. 2.5a for the sake of comparison. For all the cases analysed, the reduction in θ_{max} mainly occurs due to the deterioration of the main lobe as well as drastic increase of the side-lobe levels due to coupling. An example case (L $= 0.35\lambda_L$) of deterioration of the scanning performance at the high frequency when scanned beyond the respective maximum scanning angle ($\theta_{max} = 22^o$), along the E-plane is illustrated in Fig. 2.5b. Finally, in order to complete the analysis, the variation of the maximum scanning angle (θ_{max}) for the E- and H-plane arrays with different radiator dimensions at the low frequency of operation is presented in Fig. 2.6. The plot serves well for the comparative analysis summary presented in a latter section (2.3).

2.2.2 Substrate permittivity

For each value of dielectric permittivity considered, the radiator was retuned and the appropriate dimensions taken into account for the analysis. The procedure was repeated for all the dimensions of interest in the analysis. Only practical values of relative dielectric permittivity ($\epsilon_r = 2.33$ ($tan\delta = 0.0004$), 3.38 ($tan\delta = 0.0017$), 4.5 ($tan\delta = 0.0020$) and 6.2 ($tan\delta = 0.0027$)), commonly used for fabrication were considered. The realised gain at the maximum scanning angle ($G_R(\theta_{max})$) normalised to the broadside gain ($G_R(\theta_0)$) has been used as the metric for the assessment. Both

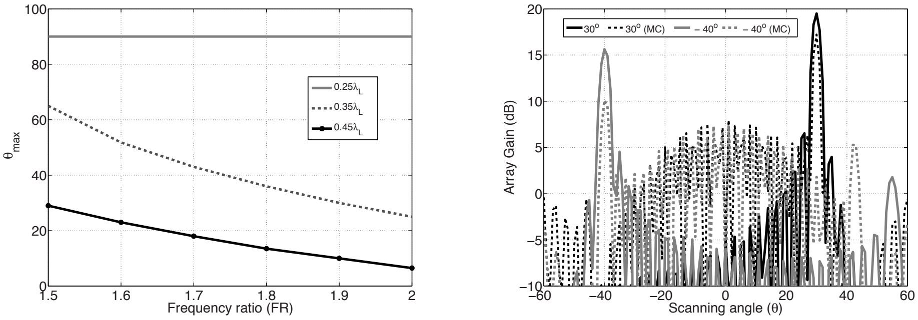

(a)

(b)

Figure 2.5: (a) θ_{max} for ideal case (excludes coupling). (b) Illustration of deterioration of scanning performance beyond θ_{max} (E-plane) for L = $0.35\lambda_L$, $d_E = 0.45\lambda_L$, FR = 1.5.

gain values used take the effect of mutual coupling into account. This is an important difference as compared to the previous section where only the evaluation of the maximum scanning angle is used (Eqn. 2.2). In this regard, the evaluation of the impact of permittivity on the pattern is accounted for. The inter-element spacing along the E-plane and H-plane were maintained at $d_E(d_H) = L(orW) + 0.11\lambda_L$. It is also worth stating that the substrate thickness for all cases presented varies only marginally between $0.02\lambda_L$ and $0.025\lambda_L$. The variations in performance with dielectric permittivity(ϵ_r) for the E and H-plane arrays are presented in Fig. 2.7.

There are two important observations which can be made from these plots. Firstly, with increased permittivity, the realised gain at the maximum scanning angle (θ_{max}) increases for the E-plane array and decreases for the H-plane array. Secondly, the performance variation with higher permittivity is more pronounced for radiators with lengths or widths higher than $0.3\lambda_L$, whereas the impact is not very significant for smaller values ($L, W < 0.3\lambda_L$). The first inference can be attributed to the variation of the radiator pattern with increase in substrate permittivity. For the chosen reference radiator, the substrate permittivity increases, for given radiator dimensions (L and W), the pattern's peak broadside gain decreases slightly in addition to the broadening of the pattern along the E-plane. The corresponding H-plane pattern however, becomes more directive, compensating for the pattern broadening along the E-plane. This behaviour hence results in the reduction of the realised gain at angles more than $\pm 30^o$ (in the element's embedded pattern) along the H-plane and a slight increase in realised gain for the same angular values along the E-plane. However, for radiators with smaller dimensions ($L, W < 0.3\lambda_L$), the difference in peak gain at angles larger than $\pm 30^o$ (in the embedded element's pattern) along both E- and

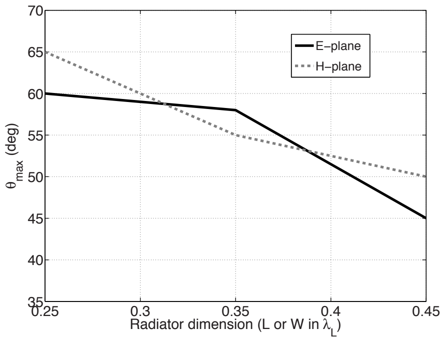

Figure 2.6: Variation of θ_{max} at low frequency of operation with radiator dimensions (L and W) for E-plane and H-plane arrays.

H-planes with increasing permittivity is only marginal, resulting in almost constant realised gain levels at the maximum scan angle(θ_{max}), which thereby explains the second inference.

Substrate thickness

Another related parameter of interest is the thickness of the dielectric substrate. However, based on the analysis carried out, it was observed that this parameter (varied between $0.02\lambda_L$ and $0.04\lambda_L$), does not have any noticeable impact on the scanning performance of both E- and H-plane arrays. Graphical illustrations are hence dispensed with.

2.3 Discussion

Based on the results of the investigation, the marked difference in scanning performance between arrays with radiator dimensions less than and greater than $0.3\lambda_L$ has been observed. However, even with smaller $(L, W < 0.3\lambda_L)$ dimensions, the high frequency scanning performance is severely limited for frequency ratios (FR) greater than 1.7:1. Another important inference is the manner in which the permittivity impacts the scanning performance. The increase in the substrate permittivity typically results in higher coupling levels between radiators, as small inter-element spacing $(d_E(ord_H) = L(orW) + 0.11\lambda_L)$ were maintained for all the cases considered in the analysis. For radiators with patch dimensions less than $0.3\lambda_L$, as a consequence of their broader element patterns, the impact of the increase in the permittivity, and therefore the mutual coupling, on the scanning performance remains nearly constant. On the other hand, the reduction in the normalised realised gain, with larger patch

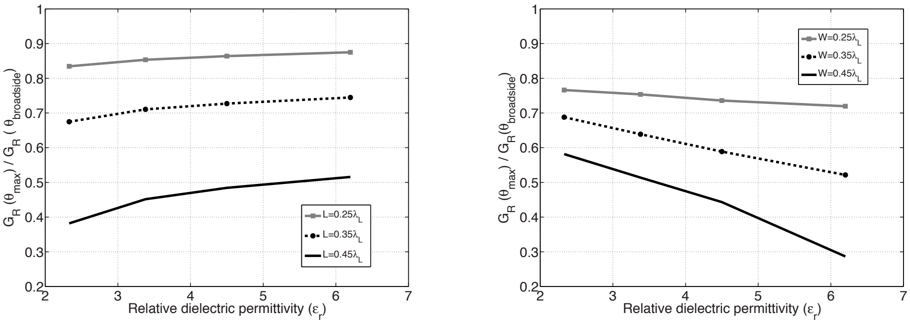

(a) (b)

Figure 2.7: Influence of relative dielectric permittivity (ϵ_r) on realised gain at maximum scan angle (θ_{max}) along E/H-planes (normalised to broadside gain). Dimension scaling in λ_L.

dimensions ($L, W > 0.3\lambda_L$), is more pronounced due to the variation of the embedded element pattern with increasing permittivity, as explained in the previous section. In other words, maintaining smaller patches ($L, W < 0.3\lambda_L$) permits the use of substrates with higher higher permittivity without causing significant difference in the peak gain performance at the maximum scanning angle (θ_{max}). A permittivity value of $\epsilon_r = 3$ provides an acceptable compromise for maintaining realised gain with scanning in both E- and H-plane arrays. The investigation has hence demonstrated the limitations existent on the radiator dimensions, frequency ratio and dielectric permittivity for achieving wide-angle scanning in the operational sub-bands for arrays with printed dual-band patch radiators.

2.4 Summary

In this chapter, the impact of mutual coupling on the scanning performance of phased arrays of printed dual-band patch radiators was presented. The realised-gain based investigation provided insights into the practical dependence of the maximum scanning angle (at which the realised gain drops to half of the ideal case) on the frequency ratios (between sub-bands), as functions of patch dimensions, substrate permittivity and thickness. The detailed analysis provided insights into the performance limitations with respect to each of these metrics. Furthermore, the differences in performance between the E-plane and H-plane arrays have also been analysed separately.

The major conclusions, with respect to this type of slot-loaded dual-band element, can be summed up as follows. Firstly, scanning is practically achievable, up to a maximum of 50-60 degrees, with small element dimensions (L, W $< 0.3\lambda_L$), at both bands when the frequency ratio (FR) is less than or equal to 1.6:1. For ratios greater than 1.7:1, scanning is extremely limited ($< 25\,^{\circ}$), even with these dimensions. Secondly, it is observed that for radiators with patch dimensions less than $0.3\lambda_L$, the impact of the increase in the permittivity, and therefore the coupling, on the scanning performance remains nearly constant. However, even with slightly larger patch dimensions (L, W $> 0.3\lambda_L$), the reduction in normalised realised gain is more pronounced due to the variation of the embedded element pattern with increasing permittivity. These insights reiterate the need to develop novel solutions to address both the problem of having radiators with low-profile electrical dimensions and low levels of mutual coupling. Finally, it is worth reiterating that the analysis presented here is specific to this particular type of dual-band patch antenna and is limited to linear arrays, and therefore do not represent any fundamental limit on the performance of dual-band antennas in arrays. The analysis of the mutual coupling characteristics of planar arrays would require a separate study.

The approach carried out in this investigation, introduces a new way analysing dual- or multi-band arrays, by relating the scanning performance to practical antenna design metrics. The limitation with respect to the maximum achievable frequency ratio, supporting wide-angle scanning, also provided important considerations. Finally, the reference dual slot-loaded radiator, used in the analysis, represents a wide class of dual- or multi-band slot-loaded patch radiators. These aspects of the investigation ensured direct application of the insights gained from the analysis for the development of novel dual- and multi-band antenna designs, presented in the following chapters.

Chapter 3

Dielectric-Contrast Technique

Mutual coupling between patch antennas is, in most cases, detrimental to the array performance. The effects of mutual coupling on the scanning performance of the array are well understood and have been systematically documented in literature [65–73]. In the context of dual- or multi-band antenna arrays, the requirement for supporting wide-angle scanning capability at the operational bands would impose strict constraints on the electrical dimensions of the unit-cell, especially at the low frequency band. Consequently, the inter-element spacings, typically $< 0.4\lambda$, result in increased levels of coupling. The development of a technique to maintain low levels of mutual coupling with small inter-element spacing hence formed one of the major research challenges. Inter-element spacing less than half-a-wavelength, between 0.3λ and 0.4λ, formed the primary target range of interest.

Recently, many techniques, including the use of electromagnetic band gap (EBG) structures [51, 58], frequency selective surfaces (FSS) [50] and ground slits [49, 59], have been proposed in literature to suppress propagation of surface waves and reduce coupling between array elements. These techniques however, have severe performance limitations and, in most cases, increase the fabrication complexity as well. The use of electromagnetic band gap (EBG) and frequency selective surface (FSS) structures in between radiators, to reduce coupling, inevitably increases the inter-element spacing, whereby the scanning capability of the arrays employing these structures are severely compromised. On the other hand, techniques that involve the use of ground slits ([49, 59]) have serious limitations in practical array applications as the presence of the slits in the ground planes increase the backward radiation, which, in turn, would pose serious integration problems for the electronic components behind the radiator elements.

In this chapter, the development of the dielectric-contrast technique, based on multilayer substrate architectures, to reduce mutual coupling between closely-spaced $(0.3 - 0.5\lambda)$ patch antennas in array, is presented. The idea behind the technique proposed is based on studies of patch antennas on heterogeneous substrates [74, 75], in which the possibility to change the lateral wavenumber due to spatial variations of the permittivity profile of the dielectric has been shown. The proposed technique removes the need to employ external structures (like EBGs etc.) and can be realized without any fabrication-related complications. Further, with the use of the proposed technique, it is also possible to maintain very small inter-element spacing, thereby leaving the scanning performance of the array unaffected. The concept basis, scope, its application to patch-based antenna arrays and experimental demonstration are described in the following sections of this chapter.

3.1 Dielectric-contrast technique

The dielectric-contrast technique was developed to achieve two main objectives. Firstly, the mutual coupling needs to be reduced maintaining similar inter-element spacing, as that maintained with a homogeneous substrate. This is, as previously mentioned, pivotal for dual- or multi-band array applications requiring wide-angle scanning. Secondly, the operational bandwidth needs to be maintained without any drastic reduction or detuning. The proposed technique involves the modification of the substrate characteristics through the use of multilayer architectures, which, in turn, modifies the characteristics of the operational mode and lowers the coupling along the lateral direction. It is also demonstrated, through experimental validation, that the technique does not increase the fabrication complexity, making it useful for practical applications. Finally, it is worth mentioning, that the current scope of the technique is limited to application in patch antenna arrays, which forms the primary research topic of interest in this thesis.

3.1.1 Concept basis and multilayer substrate architecture

The mutual coupling between adjacent antennas as a function of the inter-element spacing exhibits a periodic behaviour. For patch antennas, high levels of coupling are present for inter-element spacings less than half wavelength. Hence, coupling levels can be reduced by modifying the surface wave characteristics, whereby, the electrical inter-element spacing between adjacent antennas are increased. This rationale forms the concept basis behind the use of the proposed multilayer substrate architecture, shown in Fig. 3.1a.

The use of three layers results in two points of material discontinuity, as marked in Fig. 3.1a. Further, the permittivity (ϵ_{r1}) of the top and bottom layers are maintained the same, whereas the substrate constituting the middle layer has a different

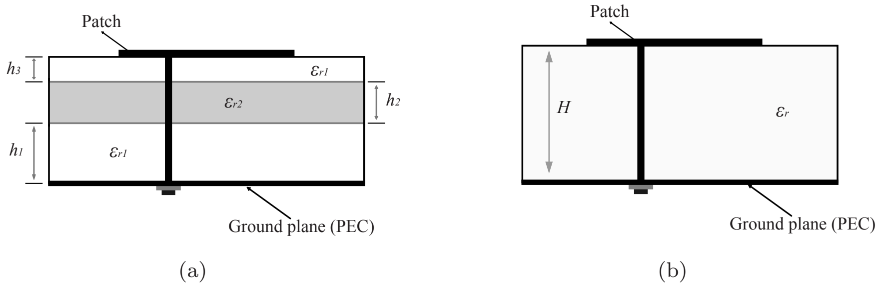

Figure 3.1: Side view comparison. (a)- proposed multilayer substrate and (b)- homogeneous substrate. Layer thickness not to scale, only for illustration.

permittivity (ϵ_{r2}) value. The contrast provided between the layers ($\epsilon_{r2}/\epsilon_{r1}$) form the basis of the proposed technique. Another motivating factor for the choice of the three layer architecture is that the use of more layers would complicate the fabrication process, especially if the individual layers possess different values of permittivity ($\epsilon_{r1}, \epsilon_{r2}, ...\epsilon_{rn}$).

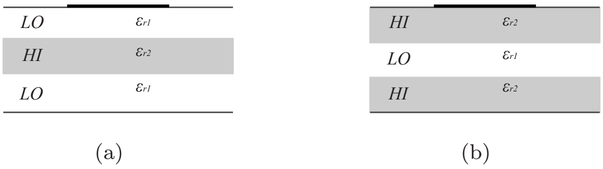

Figure 3.2: (a)- LO-HI-LO architecture and (b)- HI-LO-HI architecture. In both cases $\epsilon_{r2} > \epsilon_{r1}$.

There are two possible variations of the proposed multilayer architecture, as shown in Fig. 3.2. Both the 'LO-HI-LO' and the 'HI-LO-HI' architectures result in dielectric contrast. However, if the inter-element spacing and dielectric thickness are to be maintained similar to that of homogeneous substrates, the use of the 'HI-LO-HI' architecture would, as a consequence of having a higher value of effective permittivity (ϵ_{eff}), impact the operational bandwidth. Hence, the 'LO-HI-LO' architecture (Fig. 3.2a) is chosen, wherein the permittivity of 'LO' layers (ϵ_{r1}) are maintained similar to that of the homogeneous substrate (ϵ_r). The concept can be viewed as the use of a high permittivity substrate inserted into the homogeneous substrate through which the characteristics of the operational mode are modified. The dielectric contrast ratio ($\epsilon_{r2}/\epsilon_{r1}$) needs to be small enough, such that the effective permittivity of the substrate (ϵ_{eff}) is not drastically changed compared to that of the homogeneous substrate. A high contrast ratio would also result in detuning of the antenna and impact the operational bandwidth as well.

There are three important factors associated with optimisation of the performance. Firstly, the inter-element spacing (d_e), which, in conjunction with the position of the high permittivity layer (along the axial direction), forms the major factor in determining the coupling level between adjacent antenna elements. The dielectric contrast ratio ($\epsilon_{r2}/\epsilon_{r1}$) and the thickness of the high permittivity layer (h_2) constitute the other two factors.

In the upcoming sections, the application and optimisation of the dielectric-contrast technique for coupling reduction in patch antenna arrays are used to demonstrate effectiveness of the proposed technique.The importance of having a three layer architecture, impact of the position of the high permittivity substrate and inter-element spacing (d_e), and performance comparison with a homogeneous substrate are presented in a sequential manner. In addition to this, modal analysis, supporting the conceptual basis, illustrating the modification of the operational mode characteristics, are also presented for the optimised versions of the patch antennas with both the homogeneous and multilayer substrates. It is worth mentioning, that the technique presented here specifically focuses on the reduction of surface coupling, as the space coupling between the array elements would still be present.

3.2 Application of the dielectric-contrast technique - Patch antenna arrays

In order to evaluate the variation of the mutual coupling with both the position of the high permittivity substrate and inter-element spacing (d_e), a full-wave patch antenna model, simulated in CST-MWS, and operational in the S-band, was considered. Two patch antennas were arranged in a linear array along the E-plane (x-z plane in Fig. 3.3b). The main reason for this approach was to evaluate the coupling variation along the maximum coupling plane, which in the case considered, was along the radiator's E-plane. A dielectric permittivity (ϵ_r) of 2.2 was maintained for the homogeneous substrate.

3.2.1 Impact of position of high permittivity substrate

The thicknesses of the substrate layers, used in the analysis, were defined based on standard thickness available for fabrication [76]. As a consequence, the position of the high permittivity layer was also moved along the axial direction (from the ground plane up) in steps equal to the selected thickness of the substrates. For all the cases presented in this section, the middle layer's permittivity (ϵ_{r2}) was kept at 4.5 and its thickness equal to 0.508mm. The ϵ_{r2} values equal to 3.38 and 4, which

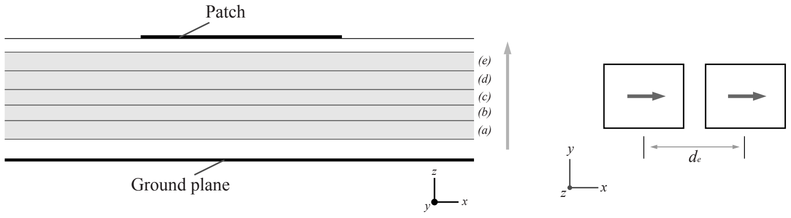

(a) (b)

Figure 3.3: (a)- Positions of high permittivity substrate (ϵ_{r2}) along axial (z) direction. (b)- Schematic of section of linear E-plane array. Arrowhead represents polarisation.

provide different contrast ratios ($\epsilon_{r2}/\epsilon_{r1}$), were also evaluated in the analysis, with performance characteristics similar to that presented in this section (These cases need similar optimisation with respect to inter-element spacing and middle layer positions). The best possible results were obtained for a permittivity (ϵ_{r2}) of 4.5. The other cases (ϵ_{r2}=3.38 or 4) are hence not repeated here to avoid redundancy. On the other hand, permittivity values greater than 4.5 were not considered in the analysis, as these values are not typical for use in patch antenna applications. Furthermore, high permittivity values which result in very large contrast also impact the operational bandwidths.

The impact of the position of the high permittivity layer along the axial direction (z-axis) of the patch antenna needs to be evaluated in conjunction with the inter-element spacing (d_e). As previously mentioned, the inter-element spacing (d_e) needs to be small enough, at the low frequency band, for dual- or multi-band array elements, in order to maintain wide-angle scanning capability at the high frequency bands operation. In this regard, inter-element spacings between 0.3λ and 0.5λ formed the target range of interest for the optimisation. The variation of the position of the high permittivity layer was carried out to achieve the lowest possible mutual coupling levels in the targeted range of the inter-element spacing (d_e). For the illustration presented in this section, five different positions of the high permittivity layer, along the axial direction, were considered. These regions are sequentially marked (a)-(e) in Fig. 3.3a, from the ground plane up. The total substrate thickness (H) is maintained constant for all the cases presented here.

As a first step, the variation of the mutual coupling (between the patch antennas) with inter-element spacing (d_e) for the homogeneous substrate, presented in Fig. 3.4a, is discussed. Although coupling levels below -20 dB are achieved for spacings in excess of 0.5λ, high levels of coupling are nevertheless existent inside the target range of spacing $(0.3 - 0.5\lambda)$, with maximum of -9.1 dB for a spacing of $d_e = 0.36\lambda$.

With the introduction of the high permittivity layer into the homogeneous substrate, the behavioural patterns of the mutual coupling with inter-element spacing for

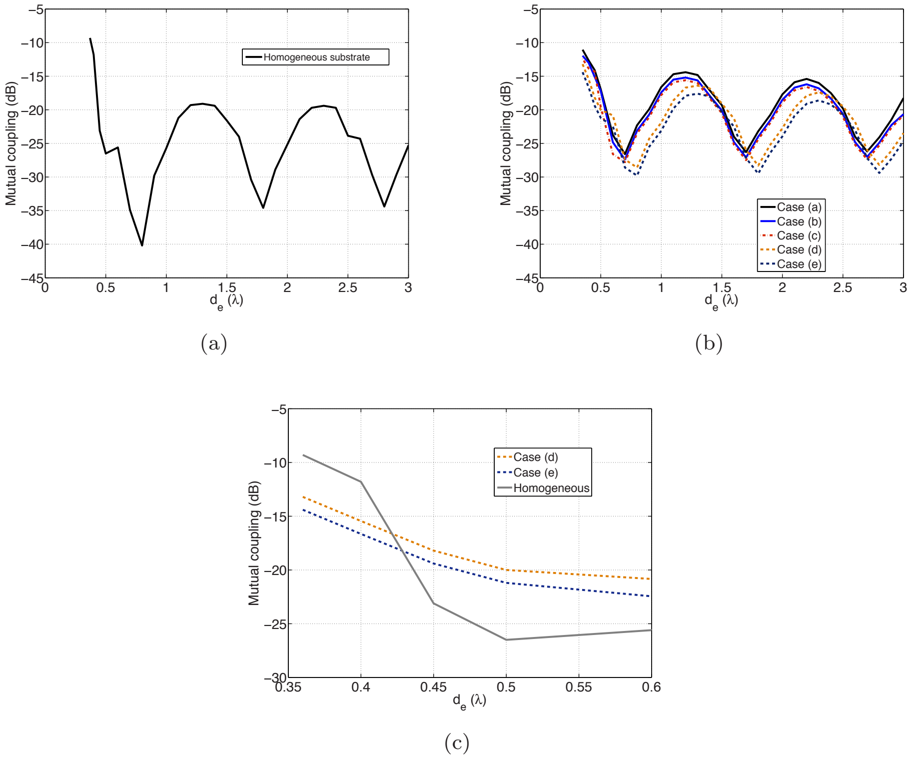

Figure 3.4: Variation of mutual coupling with inter-element spacing (d_e). (a)- homogeneous substrate, (b)- for different positions of high permittivity layer in multilayer substrate and (c)- comparison between homogeneous and best cases of the multilayer substrate.

different positions of the high permittivity layer were analysed, and are summarised in Fig. 3.4b. A clear reduction in the mutual coupling levels for all the cases analysed can be seen from Fig. 3.4b. However, for the target range of inter-element spacing, curves (d) and (e), which correspond to the position of the high permittivity layer closer to the radiating patch, demonstrate the best possible match. Other positions exhibit better match (lower levels of mutual coupling) for different inter-element spacing values. For example, curve (c) provides the best performance (in terms of coupling) for a spacing of nearly 0.65λ. The main reason for this variation being the modification of the operational mode's characteristics, as per the position of the high permittivity substrate. This reasoning is substantiated through modal analysis curves, presented in Section 3.2.3. The plots clearly illustrate the need to co-optimise the position of the high permittivity layer and the inter-element spacing (d_e).

The position of the high permittivity layer also impacts the field distribution beneath the patch region, which is more uniform, when the layer is placed closer to the radiating patch. The variation in the field distribution for the different positions considered is presented in Fig. 3.5. The variation of the field distribution is also responsible for the difference in the mutual coupling levels achieved for different positions (of the high permittivity layer) considered. The more uniform field distributions achieved with the placement of the high permittivity layer closer to the radiating patch, aid in reducing the field and power distribution along the lateral directions compared to that of the homogeneous substrate. This difference in the power flow characteristics are presented in Section 3.3.

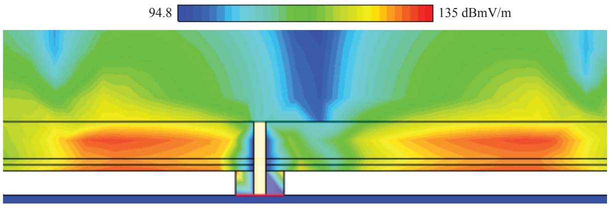

(a) Case (a)

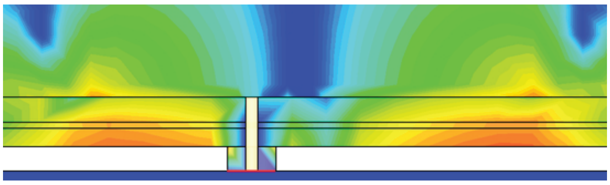

(b) Case (c)

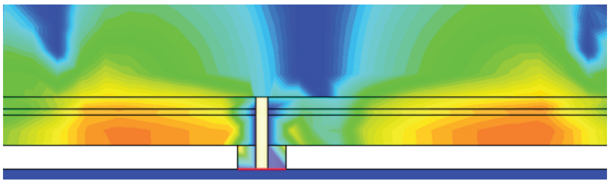

(c) Case (e)

Figure 3.5: Variation of the E-field distribution (E_z) along the axial *(z)* direction.

Two layer architecture

A limiting case of the movement of the high permittivity substrate, beyond case (e) in Fig. 3.3a, results in a two layered substrate. The high permittivity layer is, in this case, placed right beneath the radiating patch. The mutual coupling achieved with this case is however larger than the ones achieved with all the cases of the three layer substrate architecture, especially in the target range of interest of the inter-element spacing ($d_e = 0.3-0.5\lambda$). A maximum of -10.7 dB (Fig. 3.6) was achieved for an inter-element spacing (d_e) of 0.38λ, which is nearly 4 dB higher than that achieved with the best case of the three layer architecture (case (e) in Fig. 3.4b). This translates into an improvement of only 1.2 dB compared to that of the homogeneous substrate. This clearly demonstrates the performance advantage, reiterating the need to maintain a three layer architecture, as proposed in the technique.

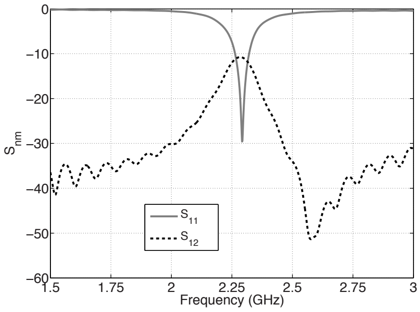

Figure 3.6: Embedded reflection coefficient (S_{11}) and mutual coupling (S_{12}) with a two layer substrate configuration.

3.2.2 Impact of thickness of high permittivity substrate

The impact of the thickness of the high permittivity layer is discussed next. For all the cases presented previously, the thickness of the high permittivity layer was maintained at 0.508mm. The main reasons for the choice of this thickness are twofold. Firstly, thicker substrates reduce the operational bandwidth and secondly, substrates thinner than 0.508mm do not provide the required contrast to achieve the reduction in mutual coupling. The impact of the variation of the thickness of the high permittivity substrate (h_2 in Fig. 3.1a) on the operational bandwidth of the patch antenna is shown in Fig. 3.7. The operational bandwidth is reduced by about 7-8% for every step increment ($n.h_2$) of the thickness of the high permittivity substrate layer. It can also be inferred from Fig. 3.7, that increasing the substrate thickness more than 2.040mm (a 4-step increment) reduces the operational bandwidth by as much as 28%. The observed behaviour is primarily due to the increase in the effective permittivity (ϵ_{eff}) of the multilayer substrate.

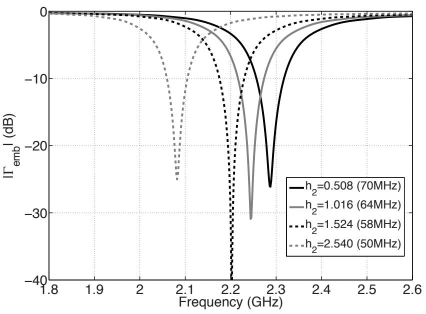

Figure 3.7: Impact of variation of thickness of high permittivity layer (h_2) on operational bandwidth.

3.2.3 Modal characteristics

The evaluation of the modal characteristics of both the homogeneous and multilayer substrates, through use of the concept of propagators, as presented in [74, 75], was carried out. The technique, presented in [74, 75], is well suited for the evaluation of inhomogeneous grounded substrates with permittivity variation along the axial direction. Constant permittivity values are assumed for lateral directions. The flexibility to define the dielectric permittivity as a function of axial direction, as defined by Equation (5) in [74, 75], makes it directly applicable to both the dielectric architectures of interest. In this regard, the dielectric permittivity profiles for the homogeneous substrate and the (optimised) multilayer substrate (case (e) in Fig. 3.3a and 4.4b) can be defined as follows:

Homogeneous substrate

$$\epsilon(z) = 2.2 \quad \text{for } 0 \leq z/h \leq 1$$

Multilayer substrate

$$\epsilon(z) = \begin{cases} 2.2 & \text{for } 0 \leq z/h \leq 0.75 \\ 4.5 & \text{for } 0.75 \leq z/h \leq 0.875 \\ 2.2 & \text{for } 0.875 \leq z/h \leq 1 \end{cases}$$

Where, z refers to the axial index, h refers to the overall substrate thickness and $\epsilon(z)$ refers to the permittivity profile for the substrate architectures. For both the profiles the relative permeability μ=1. The permittivity profile of the multilayer substrate forms a step discontinuous profile, with two points of discontinuity.

The corresponding modal curves for the grounded homogeneous and multilayer substrates are shown in Fig. 3.8. The graphs illustrate the variation of the modal

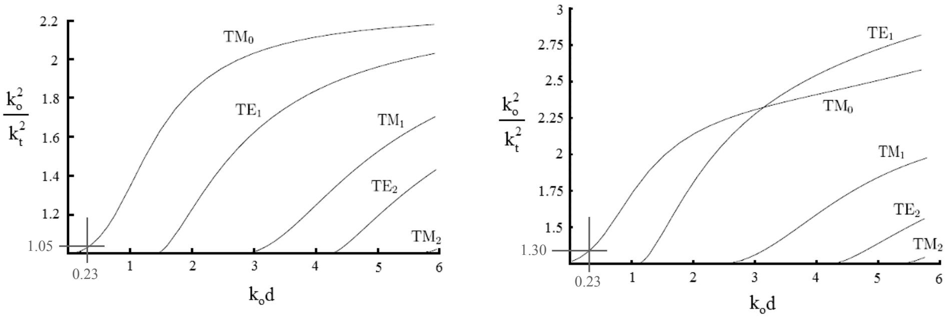

(a) (b)

Figure 3.8: Modal characteristic of grounded substrates. (a)- homogeneous substrate and (b)- multilayer substrate. $k_o d$=0.23 corresponds to thickness values used in the array models.

properties through the use of lateral wavenumber k_t, scaled in terms of the free-space wavenumber k_o. For both the homogeneous and multilayer substrates, the $k_o d$ values are marked in the respective graphs as per the thickness of the substrates maintained in both the cases. It can be inferred that the lateral wavenumber k_t shows a larger magnitude (1.33 in Fig. 3.8b) with the multilayer substrate as compared to the homogeneous substrate (1.07 in Fig. 3.8a). This clearly demonstrates the modification of the propagation velocity of the operational mode, which is slower along the lateral direction (x-y plane), with the multilayer substrate.

The decrease of the lateral propagation velocity of the surface wave results in an increase in the electrical spacing between neighbouring antennas. While this results in lower levels of coupling in dense antenna arrays, the increase in the effective permittivity (ϵ_{eff}) with this multilayer substrate slightly lowers the operational frequency of the patch antenna.

The modal characteristic plots reiterate the functional impact of the multilayer substrate architecture, whereby, the operational mode's characteristics are modified, achieving lower levels of mutual coupling between elements. As the lateral propagation characteristics of the operational mode are modified, it is also clear why the inter-element spacing forms a key part in the optimisation procedure. The interested reader is referred to [74, 75, 77] for further details on the propagators based technique.

3.3 Mutual coupling reduction in arrays

Linear array implementations with both the homogeneous and multilayer substrates were modelled and optimised in CST-MWS. Due to the large levels of coupling along the E-plane compared to that along the H-plane, linear E-plane arrays were chosen to demonstrate the effectiveness of the proposed dielectric-contrast technique (Refer Fig. 3.3b for a schematic representation of section of the linear array).

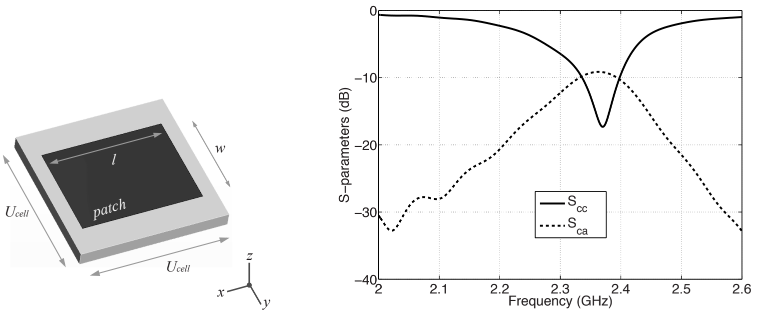

(a) (b)

Figure 3.9: (a)- Patch antenna model. (b)- Computed embedded reflection coefficient (S_{cc}) and adjacent element coupling (S_{ca}) of the centre element in linear array (S-band).

3.3.1 S-band array

The unit-cell dimensions of the individual patch radiators used in the linear arrays measure $49mm \times 49mm$. The length (l) and width (w) of the radiating patch were kept at 39 mm and 31 mm respectively. The radiator exhibits a well defined operational bandwidth of 72 MHz centred at 2.37 GHz. The E- and H-planes of the radiator are defined along the x-z and y-z planes respectively (Fig. 3.9a). The inter-element spacing (d_e) is maintained at 49 mm, which translates into a spacing of 0.38λ (at f_c = 2.37 GHz). The thickness of the homogeneous substrate (H) was kept at 4.57 mm with ϵ_r=2.2 ($tan\delta$ = 0.0004). The patch antenna is excited by means of standard SMA-feed model. It is found through full-wave simulations that the coupling level between adjacent radiators in the E-plane array (-9.14 dB) is higher as compared to the same in the H-plane array (-12.56 dB). This justifies the choice of the E-plane linear arrays for the concept demonstration. The embedded reflection coefficient (Γ_{emb}) and adjacent element coupling of the centre element in linear (1×7) E-plane array are shown in Fig. 3.9b.

The inter-element spacing falls within the range ($0.3 - 0.5\lambda$) of interest where the mutual coupling needs to be reduced with multilayer substrate configuration. The multilayer architecture is introduced into the antenna design, maintaining similar inter-element spacing as that of the homogeneous substrate (0.38λ). Based on the results of the optimisation, presented in the previous section, the high permittivity layer is introduced at 3.558mm from the ground plane. This corresponds to case (e), presented in Fig. 3.3a. The respective specifications of the multilayer architecture are as follows: $\epsilon_{r1} = 2.2$, $\epsilon_{r2} = 4.5$, $h_1 = 3.558$mm, $h_2 = 0.508$mm, $h_3 = 0.381$mm and $d_e = 51$mm (0.387λ). It is worth reiterating, that the dimensions of the radiating patch are maintained the same as that of the original version with the homogeneous substrate. The electrical inter-spacing is maintained to be same in both cases to ensure a direct comparison.

The reduction in the mutual coupling between adjacent radiators with the use of the proposed multilayer technique is illustrated through Fig. 3.10. A reduction of nearly 5.5 dB is achieved with the proposed dielectric-contrast technique, with the same inter-element spacing and similar substrate thickness. The operational band is shifted slightly to the low frequency due to the use of the high permittivity substrate. It is worth noting that the centre frequency, with the multilayer substrate, is not explicitly retuned to be the same as that of the element with the homogeneous substrate as the prime focus is with the demonstration of the effectiveness of the proposed technique in reducing the coupling with identical inter-element (electrical) spacing for both the cases considered. To this end, the same (electrical) spacing and patch dimensions have been maintained to provide a fair and direct comparison.

The field and power flow distributions in the E-plane array, obtained by exciting the centre element of the array, with both the homogeneous and multilayer dielectric substrates, are presented in Figs. 3.11-3.12. The region marked A-A' represents the two edges of the metal patch of the centre element. The edge of the adjacent patch is marked as B and the feed point of the adjacent element is marked C. Comparing Figs. 3.11 and 3.12, it can be inferred that with the use of multilayer substrate, the field distribution (of the dominant component - E_z) patterns in array remains similar to that of the stand-alone element configuration. The field distribution is well confined within the region marked A-A'. This helps in decreasing the lateral field spreading reducing the mutual coupling. The plots also show a marked difference in the field strengths at the edge of the adjacent patch (B) and at the feed point (C) of the adjacent element. Furthermore, it can be observed that with the use of the multilayer substrate the field distribution is also uniformly maintained along the vertical axis of the array (from ground plane to patch). Finally, the computed radiation efficiencies are at 0.98 and 0.97 respectively for the homogeneous and multilayer substrates illustrating the non-negative impact of the multilayer substrate on the radiation characteristics of the array elements

The power flow distribution plots, presented in Fig. 3.13, reiterate the behavioural patterns similar to the ones presented in Figs. 3.11-3.12. Comparing the power flow values at points B and C (edge and feed positions of the adjacent patch element), there exists a difference of around 4.5 to 5.5 dB (around 59-61 dB for single layer and 54-56 dB for multilayer substrate). This clearly implies that with the use of the dielectric contrast technique, lower amount of power is coupled to the adjacent elements achieving reduced levels of coupling between the array elements. Table 3.1 presents a comparative summary on the coupling performance between the homogeneous and multilayer substrate cases for the S-band linear array model.

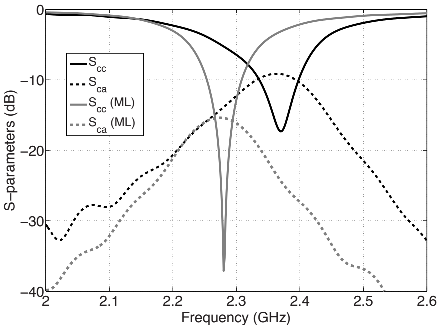

Figure 3.10: Computed embedded reflection coefficient (S_{cc}) of centre element in E-plane array (S-band). $S_{cc}-$ single layer substrate and $S_{cc}(ML)-$ multilayer substrate. Adjacent element coupling (S_{ca}) between adjacent radiators in E-plane array, $S_{ca}-$ with single layer substrate and $S_{cc}(ML)-$ with multilayer substrate.

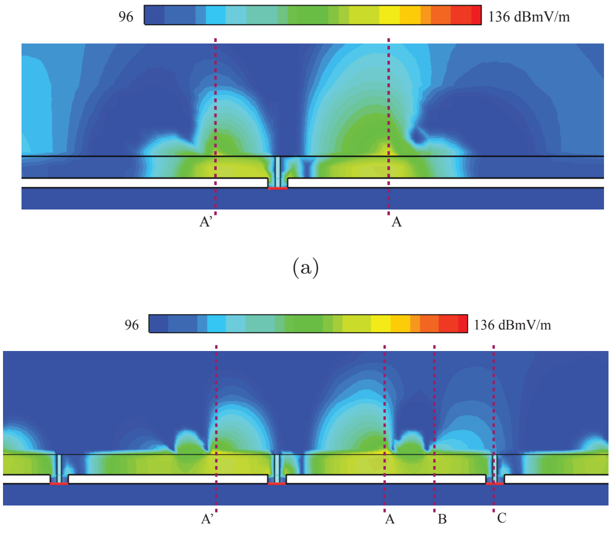

(a)

(b)

Figure 3.11: Electric field component (E_z) distribution of element with homogeneous substrate. (a) in stand-alone configuration with axially (along x-axis) extended substrate and (b) in E-plane array.

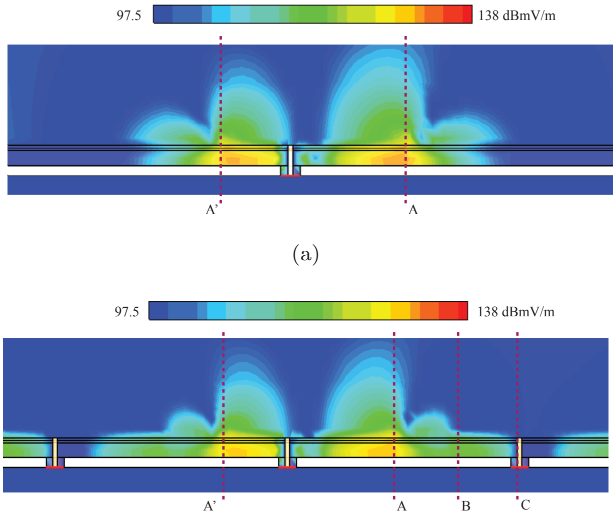

(a)

(b)

Figure 3.12: Electric field component (E_z) distribution of element with multilayer substrate. (a) in stand-alone configuration with axially (along x-axis) extended substrate and (b) in E-plane array.

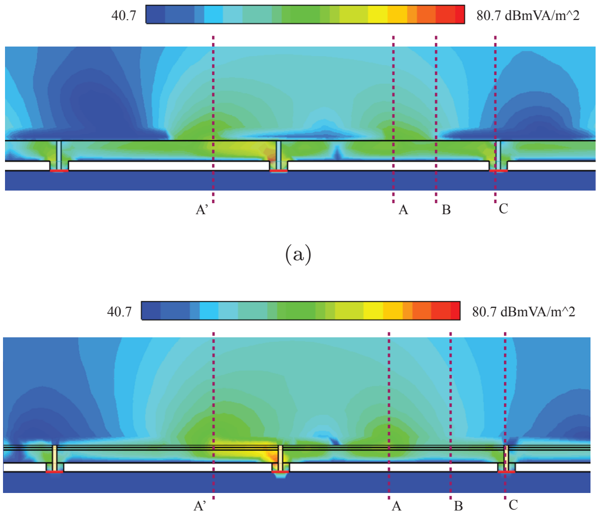

(a)

(b)

Figure 3.13: Power flow distribution in E-plane array. (a) with homogeneous substrate and (b) with multilayer substrate.

Table 3.1: Computed performance - Homogeneous vs. multilayer substrate (S-band).

Type	Substrate thickness (mm)	f_c (GHz)	d_e (λ)	Coupling level (dB)	Directivity (dB)
Homogeneous	4.57	2.37	0.382	-9.6	5.57
Multilayer	4.32	2.29	0.387	-15.1	5.25

3.3.2 X-band array

To further validate the effectiveness of the proposed technique at another operational band, an X-band linear array was considered. For the X-band linear E-plane array the inter-element spacing (d_e) was maintained at 0.375λ, for both the homogeneous and multilayer substrates. An optimisation procedure, similar to the one presented in the previous section, was carried out for this case as well. The optimised values of the dielectric thicknesses and permittivity for both the single and multilayer substrates are as follows: homogeneous substrate - $H = 1.57$mm, $\epsilon_r = 2.2$, $d_e = 13.5$mm (0.378λ), multilayer architecture - $h_1 = 1.041$mm, $h_2 = 0.254$mm, $h_3 = 0.254$mm, $\epsilon_{r1} = 2.2$, $\epsilon_{r2} = 4.5$ and $d_e = 14$mm (0.375λ).

The reduction in the mutual coupling achieved with the use of the multilayer substrate architecture is illustrated through Fig. 3.14. Mutual coupling reduction by about 4.8 dB was achieved with the multilayer substrate architecture, exhibiting performance improvement levels similar to that achieved in the S-band linear array (presented in the previous sub-section). The homogeneous and multilayer substrate architectures, operational in the X-band, were used for the development of experimental linear array prototypes, the associated details and results of which are presented in the next section.

Table 3.2: Computed performance - Homogeneous vs. multilayer substrate (X-band).

Type	Substrate thickness (mm)	f_c (GHz)	d_e (λ)	Coupling level (dB)
Homogeneous	1.57	8.20	0.378	-9.7
Multilayer	1.549	7.95	0.375	-14.6

3.4 Experimental verification

The experimental verification of the dielectric-contrast technique is presented in this section. The fabricated linear E-plane (1 × 3) array prototypes, operational in the X-band, with both the homogeneous substrate and the proposed multi-layer substrate

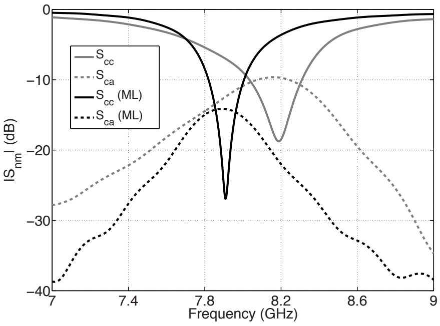

Figure 3.14: Computed embedded reflection coefficient (S_{cc}) of centre element in E-plane array (X-band). $S_{cc}-$ single layer substrate and $S_{cc}(ML)-$ multilayer substrate. Adjacent element coupling (S_{ca}) between adjacent radiators in E-plane array, $S_{ca}-$ with single layer substrate and $S_{cc}(ML)-$ with multilayer substrate.

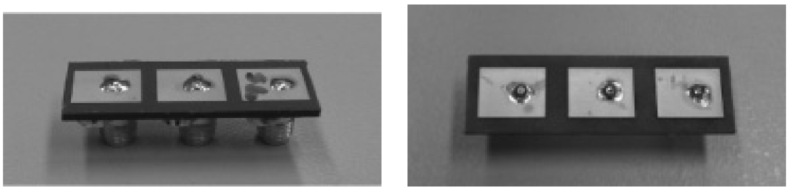

(a) (b)

Figure 3.15: Fabricated linear array prototypes. (a)- with homogeneous substrate ($\epsilon_r = 2.2$) and (b)- with multilayer substrate ($\epsilon_{r1} = 2.2$, $\epsilon_{r2} = 4.5$).

architectures are shown in Fig. 5.15. The mutual coupling between the array elements and the embedded reflection coefficient (Γ_{emb}) and radiation patterns of the array elements were measured. The measured embedded reflection coefficient (Γ_{emb}) and mutual coupling characteristics of the centre element (no: 2) in the linear (1×3) arrays, with both the substrate architectures, are presented in Fig. 5.16.

A reduction of 4.5 dB is achieved with the proposed multilayer substrate with dielectric-contrast. This conforms well with the results of the simulations. Furthermore, the operational bandwidth also remains unaffected with the use of the multilayer substrate. The measured embedded radiation patterns of the centre element of both the arrays are presented in Fig. 3.17. The embedded patterns achieved with both the types of substrates exhibit similar characteristics in terms of both the co- and cross-polarisation, demonstrating that the use of multilayer substrate is not detrimental to the radiation characteristics of the array elements. The only difference between the two cases being the reduction of the peak gain by around 0.5-0.6 dB with the mul-

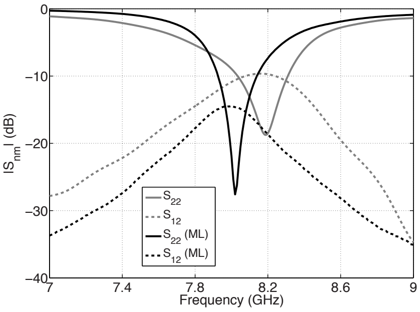

Figure 3.16: Measured embedded reflection coefficient and mutual coupling characteristics of centre element (no:2) in linear array with homogeneous and multilayer (ML) substrates.

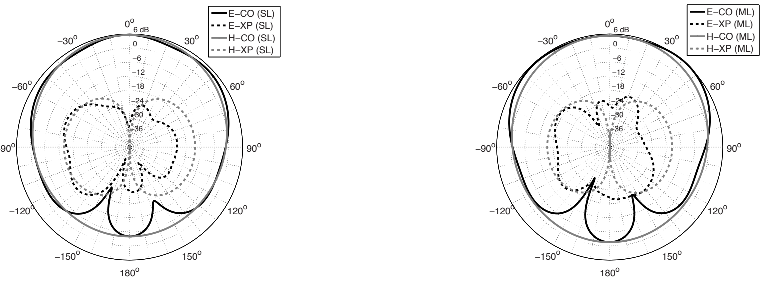

(a)

(b)

Figure 3.17: Measured embedded radiation patterns of the centre element (no:2) in linear array. (a)- homogeneous substrate and (b)- multilayer substrate (ML).

tilayer substrate (dB) as compared to that achieved with a homogeneous substrate (dB). Table 3.3 summarises the difference in measured performance between the two cases.

The experimental results hence, demonstrate the effectiveness of the proposed technique to reduce the mutual coupling without the use of EBGs or even metal cavities, which are commonplace in many antenna array designs. Large increase in inter-element spacing ($0.6 - 1\lambda$) are required for coupling reduction of about 4-6 dB, which are typical reduction levels achieved with the use of EBGs, FSS or defected ground-plane techniques. Further, the reduction in coupling is achieved without modifying the radiator patch dimensions or any increase in the inter-element (electrical) spacing between adjacent radiators. The demonstrated performance, achieved with very small inter-element spacing (0.375λ), is extremely useful for application in dual-or multi-band phased arrays, which would almost always, due to the band separation, require very small spacing between elements.

Table 3.3: Performance comparison summary - Homogeneous vs. multilayer substrate (Measured).

Type	Substrate thickness (mm)	f_c (GHz)	d_e (λ)	Coupling level (dB)
Homogeneous	1.57	8.20	0.378	-9.6
Multilayer	1.55	8.01	0.375	-14.2

3.5 Summary

In this chapter, the development and validation of the dielectric-contrast technique, for the reduction of mutual coupling between closely-spaced ($0.3 - 0.5\lambda$) patch array antennas, was presented. The conceptual basis of the technique rests with the modification of the substrate properties, whereby the mutual coupling levels between the adjacent array elements are reduced with the alteration of the operational mode's characteristics, with the use of a multilayer substrate. In this regard, compared to the use of a homogeneous substrate, the multilayer substrate modifies the propagation characteristics of the operational mode along the later directions, reducing the coupling.

A three layer architecture is chosen to demonstrate the effectiveness of the proposed dielectric-contrast technique. The performance analysis was carried out with numerical linear patch array models simulated in a full-wave solver. The impact of the dielectric contrast ratio ($\epsilon_{r2}/\epsilon_{r1}$), and the need to co-optimise the position of the high permittivity layer (in the multilayer architecture) and the inter-element spacing d_e has been elucidated in detail. In addition to this, the impact of the thickness of the high permittivity layer on the operational bandwidth was also illustrated. Finally, the evaluation of the modal characteristics of both the homogeneous and multilayer substrate architectures was carried out, based on the concept of propagators, as introduced in [74, 75]. The modal analysis clearly demonstrated the difference in the operational modes characteristics along the lateral direction with the use of the multilayer substrate as compared to that of the homogeneous substrate. This difference manifests itself in the variation of the lateral wavenumber (k_t) between the two cases.

Based on the optimisation carried out, the reduction in coupling between adjacent array elements was demonstrated separately in both S-band and X-band full-wave linear array models. Following this, linear E-plane array prototypes, operational in the X-band, were fabricated to experimentally validate the performance. The experimental results demonstrated a reduction in the mutual coupling by 4.6 dB, similar to the levels obtained with the simulated full-wave models (both S- and X-band versions). The embedded radiation patterns of the array elements were measured and compared, demonstrating that the use of the multilayer substrate with dielectric contrast does not have any negative impact the radiation pattern characteristics or the radiation efficiencies.

The ‘non-invasive’ nature of the technique, which focuses only on the modification of the characteristics of the operational, removes the need to employ external structures (like EBGs and FSS), leaving the scanning performance unaffected. Furthermore, the multilayer architecture with dielectric contrast, is also simpler in terms of its fabrication complexity compared to the use of external structures (like EBGs and FSS) or ground slits.

The current scope of the technique is limited to single-band patch antennas with very small inter-element spacing $(0.3 - 0.5\lambda)$. Extension of the proposed technique to wideband patch antennas can be carried out as part of future research. Additionally, the impact, or improvement, in terms of mutual coupling with more substrate layers can also be evaluated as part of the future research. These studies, if carried further, would help consolidate the understanding on the scope of the proposed technique.

Chapter 4

Dual-Band Wide-Scan Phased Arrays

Dual-band phased arrays with well-separated operational bands and wide-angle scanning capability are very attractive for future multifunction radar front-ends. Apart from covering different target bands of practical interest, and compared to wideband arrays with similar frequency ratios, the use of dual- or multi-band arrays, facilitate in transferring part of the filtering to the antenna element itself, thereby relaxing the requirements on the RF back-end components in terms of efficiency. The frequency band selectivity offered also aids in reducing the interference problems due to out-of-band signals. The developmental details of novel dual-band antenna and array solutions for future multifunction radar front-ends are described in this chapter.

4.1 Existing solutions and proposed concept

In the development of dual- or multi-band antennas, the use of slot-loaded patches has often been the major type of interest. The dual-slot, u-slot and e-slot antennas [40–42, 47, 78] are arguably the most popular of the multi-band antenna concepts proposed in literature. A close scrutiny of the dual-slot antenna [41, 42], reveals the antenna's performance limitation with respect to the sub-band bandwidths, which are extremely narrow and exhibit large variation of band placements when scanned off-broadside. The u-slot antennas [40, 47], on the other hand, have serious limitations with inconsistent radiation patterns, and are virtually non-functional in arrays. Designs validating their performance in planar arrays and wide-scan applications are almost absent in current literature. This negates their consideration for wide-scan array applications, of prime interest in this thesis. Similar limitations on radiation patterns and array performance apply for the e-slot antennas as well [78].

In this chapter, the development of a novel array antenna design based on a concept using dual radiation characteristics in a single antenna element is presented. The dual electric and magnetic radiator elements are combined in a single antenna element for the development of this dual-band patch antenna. To realise a magnetic radiator in a patch, a wide comb-shaped slot has been introduced. This enables the use of both the slot-based magnetic excitation and the patch's electrical radiation characteristics in the overall radiation mechanism.

The concept of self-complementarity, proposed by Mushiake [79], introduces the possibility to combine electric and magnetic radiation components in a single radiator element. Further, it is also illustrated that ultra-wideband characteristics can be realised with proper impedance balance between the electric and magnetic components. In this regard, the duality condition of Babinet's principle is applied for the development of a class of self-complementary antennas supporting ultra-wideband operation [79]. The condition of duality, useful for microwave applications (as developed by Booker [80]), is expressed as follows:

$$Z_s . Z_e = \eta^2 / 4 \tag{4.1}$$

Where, Z_s refers to impedance of the slot antenna, Z_e refers to the impedance of the equivalent electric dipole antenna and η refers to the free-space impedance. A magnetic radiator can hence be realised using a slot in metal surface, and the performance of such a radiator can be analysed using Babinet's principle [80].

The self-complementarity principle has previously been successfully applied for the development of ultra-wideband quasi-magnetic loop or 'tulip-loop' antennas (at TU-Delft), presented in [81,82]. Linear array implementations of this quasi-magnetic antenna have also been carried out [83,84]. In both the stand-alone and linear array implementations of the 'tulip-loop' antenna, the design was primarily focussed only on achieving the quasi-magnetic radiation characteristic, through the use of CPW-feed mechanism. The antenna concept, proposed in this thesis, has been developed to incorporate both the electric and magnetic radiation characteristics, and realise multi-band instead of wideband characteristics (as achieved in [81,82]). The shape and sizes of both radiators (electric and magnetic) can be selected to support two operational bands. While the combination of electric and magnetic radiators in a single element forms the first crucial aspect, a novel *'lamppost'* feeding architecture, which offers simultaneous excitation of both electric and magnetic radiators, constitutes the other key aspect of the proposed concept. It is important to emphasise that the concept proposed allows for development of an 'array-capable' element, suitable for achieving wide-angle scanning capability, when implemented in arrays.

4.2 Comb-slot-loaded array antenna

There are two key functional aspects of the comb-slot-loaded patch antenna design. Firstly, the radiating element of the antenna, presented in Fig. 4.1a, consists of a metallic patch loaded with a four-arm comb-slot. The inner arms of the comb-slot aid in achieving band notch characteristics which result in dual-band operation with low-profile electrical dimensions of the patch. The absence of these arms would result in a u-slot arrangement, which could be used to achieve wideband operation [85] (the wideband u-slot presented in [85] is however completely non-functional in array configurations requiring scanning).

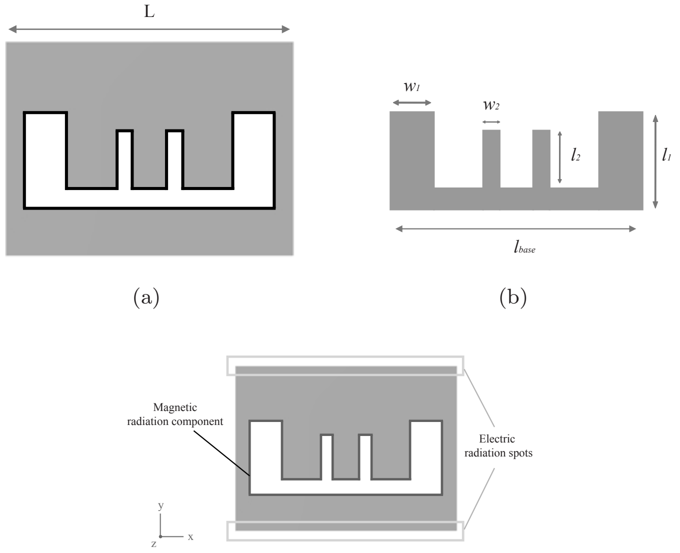

(a) (b)

(c)

Figure 4.1: (a)- Comb-slot-loaded patch and (b)- four-arm comb-shaped metallic patch.

The rationale behind the choice of this slot shape can be explained as follows. Consider a metallic patch shaped similar to the four-arm comb-slot, as shown in Fig. 4.1b. Exciting this patch by means of a simple pin-fed excitation over an infinite substrate and ground plane demonstrates the capability of this patch to support dual-resonances, as shown in Fig. 4.2. For the example case presented, the base length (l_{base} in Fig. 4.1b) was kept nearly equal to $\lambda/2$ at the 12 GHz. This comb-shaped patch radiator however, supports only electric radiation characteristics, similar to a typical patch antenna. To create an antenna architecture which can support both electric and magnetic radiation characteristics, the complementary component

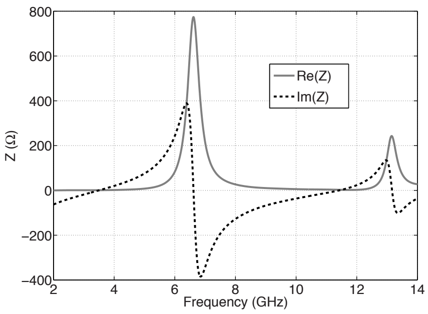

Figure 4.2: Computed impedance response of comb-shaped patch antenna.

of this comb-shaped patch, which results in a comb-shaped slot, is loaded on to a metallic rectangular patch, as previously shown in Fig. 4.1a. In this way, the electric (patch) and magnetic (comb-slot) elements are combined in the same radiator. The diagrammatic illustration of this radiation behaviour is shown in Fig. 4.1c. The widths (w_1 and w_2) can be varied to tune the frequency ratio between the bands, whereas the lengths (l_1 and l_2) can be used to vary the impedance matching achieved at the operational bands. It is worth mentioning that although the shape of the comb-slot has some semblance with the u-slot designs, pivotal functional differences exist in terms of both the radiation characteristics and sub-band bandwidths, both of which will be described and demonstrated in the upcoming sections.

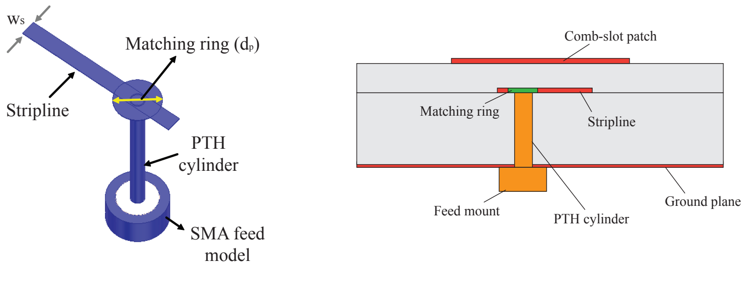

(a) (b)

Figure 4.3: Architecture of the "*lamppost*" feeding configuration.

The second major aspect of the proposed antenna is with its feeding architecture. In order to achieve electric and magnetic radiation characteristics the antenna's feed needs to be capable of exciting both the electric and magnetic characteristics. In this regard, exciting this comb-slot-loaded antenna with a pin feed, similar to other multi-band stand-alone antennas ([40–42, 47, 78]), would only result in an electric antenna, whereby, the slot's presence only aids in the modification of the surface current distribution at the operational bands. A novel *'lamppost'* feed apparatus (refer Fig. 4.3a) is hence introduced into the antenna design. The feed apparatus (Fig. 4.3a) consists of a plate-through-hole (PTH) cylinder, field-matching ring and stripline transition. The antenna architecture's side view, presented in Fig. 4.3b, is used as reference for explaining the specifics of the radiation mechanism. The stripline transition, separated from the metallic patch by a dielectric layer (refer Fig. 4.3b), excites the comb-slot inducing the magnetic characteristics. This, results in the magnetic radiation from the comb-slot, which, along with the electric radiation characteristic of the patch, are simultaneously utilised in the overall radiation mechanism. As a consequence of the position of the stripline transition, the E- and H- planes of the antenna are defined along the y-z and x-z planes respectively (refer Fig. 4.4a for axis). This dual radiation characteristic hence fundamentally differs from the conventional pin-fed or proximity-coupled excitations of single-layer narrowband or multi-band antennas [40–42, 47, 78], which predominantly make use of only the electric radiation characteristics of the patch.

The *'lamppost'* architecture, apart from serving as the antenna's feed, also provides bandwidth enhancement capability at the operational sub-bands. The plate-through-hole (PTH) cylinder (refer Fig. 4.3a) results in an inductive reactance, similar to the pin-fed excitations in conventional patch antennas. The outer diameter of the PTH cylinder can be varied to tune the slope of the inductive reactance at the operational bands. The diameter of a standard SMA connector pin (1.28 mm) is used as the inner diameter of the PTH cylinder. This inductive reactance is balanced out by the capacitive reactance offered by the stripline. The matching ring's diameter (d_p) presents an additional parameter for increasing or decreasing the capacitive reactance, as per requirements. Thus, this reactance balancing mechanism made possible with the use of the components of the feeding apparatus aids in achieving good bandwidths at the targeted operational bands. It is worth mentioning, that the optimisation procedure necessary to obtain the required sub-band bandwidths, involve the collective optimisation of the width of the stripline (w_s), matching ring diameter (d_p) and the height of the plate-through-hole (h_{PTH}) cylinder.

Other components of the antenna geometry include the dielectric substrate, which is used in two parts, the first between the ground plane and the stripline transition, and a thinner substrate separating this transition from the metal patch above it (refer Fig. 4.3b). Cavity backing is appended to the design for reducing mutual coupling, when implemented in array. The component details of the antenna unit-cell geometry are presented in Fig. 4.4.

The comb-slot design and the *'lamppost'* feeding architecture complement each other resulting in a novel dual-band array antenna supporting dual radiation characteristics, with low-profile electrical dimensions and good sub-band bandwidths. The demonstration of the antenna's radiation characteristic and bandwidth enhancement capability through full-wave numerical simulations are presented in Section 4.3.2.

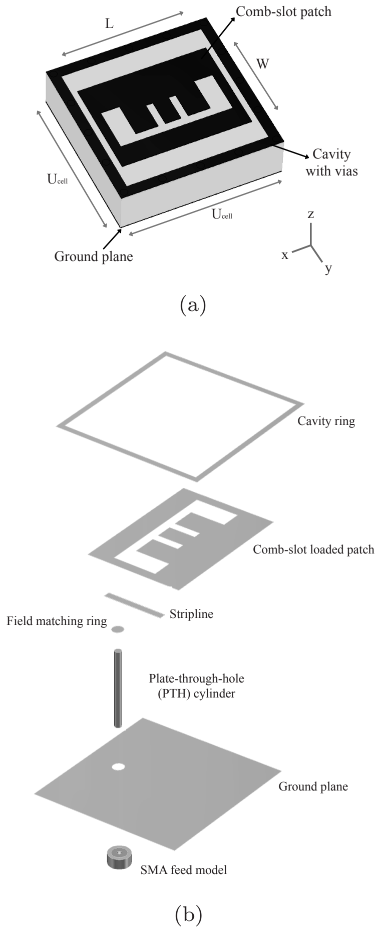

Figure 4.4: Architecture of the proposed dual-band comb-slot-loaded patch antenna unit-cell. (a)- perspective view of simulated model and (b)- exploded view of the antenna's make-up (cavity vias are excluded).

4.3 Dual-band antenna performance

The full-wave modelling of the dual-band antenna was carried out in CST-Microwave Studio (MWS). A characteristic impedance of 50Ω was used for the simulations. The wide-angle scanning prerequisite, results in small inter-element spacing, especially at the low frequency band of operation. Metal cavity backing was thus, as previously mentioned, appended to the antenna unit-cell model.

4.3.1 Impact of design parameters

The performance optimisation of the stand-alone antenna was carried out using the time-domain solver of CST-MWS. Antenna performances was optimised for operation in the X-band, which along with the S-band, were identified as the principal bands of interest for front-end development in the STARS project [8]. The main goals of the optimisation were (1) the maintenance of frequency ratios greater than or equal to 1.5:1, (2) electrical dimensions satisfying scanning requirements, (3) consistent radiation patterns at both the operational bands and (4) good sub-band bandwidths. In this regard, the first part of the optimisation process dealt with the realisation of the dual-band characteristic with the targeted frequency ratio, following which the optimisation of the sub-band bandwidths was carried out.

Electrical dimensions and frequency ratio

In order for the proposed dual-band antenna to be *"array-capable"*, its electrical dimensions needs to be suitable for supporting wide angle scanning, as dictated by the condition $d_e \leq \lambda_{op}/(1 + sin(\theta_{max}))$. The inter-element spacing (d_e) is equal to the unit-cell's dimensions, defined at the operational frequency (λ_{op}), and θ_{max} refers to the maximum scanning angle targeted for array operations. A maximum scanning angle of 60 degrees was kept as the target for the optimisation carried out. Although the collective optimisation of the patch's length and width was important for achieving the required performance, the impact of the variation of the patch length and width are presented separately in this section, for illustrating the specific impact of either quantity. For this optimisation, the maintenance of the dual-band characteristic with a frequency ratio greater than or equal to 1.5:1 was kept as the main target.

The variation of the width (W) of the patch around the final optimised value of 9.5 mm is shown in Fig. 4.5a. For larger widths, the dual-band characteristic was still maintained, with the low band shifting towards lower operational frequencies. In a similar manner, the reduction in the width below 9.5 mm, resulted in the movement of both the bands to higher operational frequencies. The difference in the electrical lengths was the principal reason behind the shift in the bands to lower or higher operational bands. The frequency ratio was also reduced for values both above and below W = 9.5 mm.

The impact of the variation of the patch length (L) is presented next. The variation in the length impacts the impedance matching at both the operational bands. The optimised value of the patch length (L) largely depends on the value of the patch's width (W). This is illustrated in Fig 4.5b, where the impact of the variation of the patch length (L) for a given patch width (W) of 9.5 mm, is presented. The patch length (L) demonstrated a best-fit for a value of 12.8 mm. Other values resulted in either lower impedance matching or marked distortion of the dual-band characteristics itself. The optimised patch length (L) and width (W) were equal to 12.8 mm and 9.5 mm respectively.

Although the lengths and widths of the comb-slot (l_1, l_2, w_1 and w_2 in Fig. 4.1b) can be used as additional parameters for fine-tuning the frequency ratio and impedance matching, the required performance was achieved with the above mentioned procedure and hence, the dimensions of the comb-slot were maintained constant for the optimisation procedure. The interested reader can make use of these additional parameters for performance optimisation, if required.

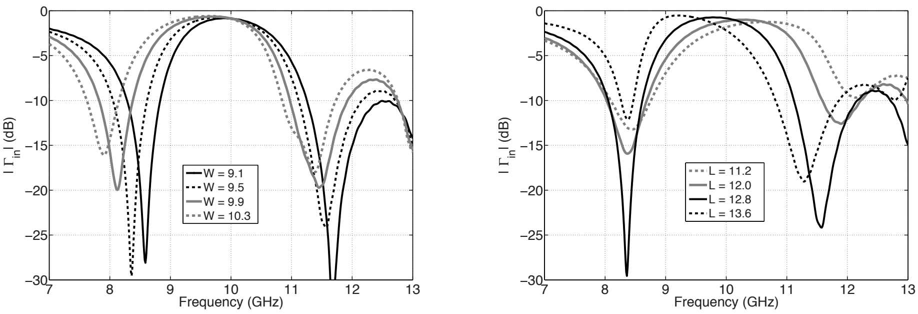

(a) (b)

Figure 4.5: Optimisation of the patch dimensions. (a)- influence of patch width (W) and (b)- influence of patch length (L).

Sub-band bandwidth

The optimisation of the sub-band bandwidths, as mentioned in the previous section, primarily depend on the feeding apparatus' dimensions, including the width of the stripline (w_s), the height of the PTH cylinder (h_{PTH}) and diameter of the matching ring (d_p). The permittivity of substrate (ϵ_r) provided another related parameter of interest.

For a given matching ring diameter d_p and stripline width w_s, an increase in the PTH cylinder's height (h_{PTH}), which implies an increase in the inductive reactance offered by the feed cylinder, resulted in the disturbance of the reactance balance, which manifests itself by both reducing the bandwidths at the sub-bands and considerably shifting the band placements (in frequency). This effect is demonstrated through Fig. 4.6a, which summarises the impact of increasing the height of the plate-through-hole cylinder. The maintenance of the right reactance balance is key to achieve good sub-band bandwidths.

Finally, the possibility of achieving low-profile dimensions, with the use of high permittivity substrates was analysed. Only standard values of dielectric permittivity (ϵ_r) and substrate thickness (t), available for fabrication [76], were used for the optimisation procedure, thus avoiding the need to retune the substrate thickness for prototype fabrications. The use of permittivity (ϵ_r) higher than 2.2, distorts the dual-band characteristic of the antenna, resulting in multiple resonances with very narrow bandwidths. The frequency ratio is also affected as a consequence of this shift. Furthermore, permittivity values higher than 4.5 were not considered in the optimisation, in order not to increase the coupling between elements when implemented in array. The corresponding optimisation summary is presented in Fig. 4.6b.

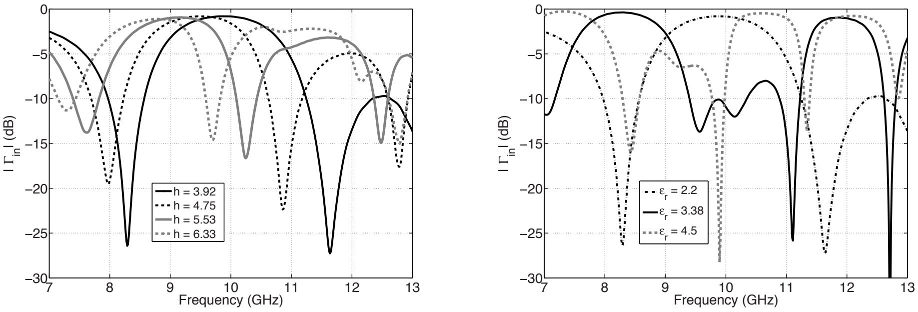

(a)

(b)

Figure 4.6: (a)- Impact of variation of PTH cylinder height (h_{PTH}) and (b)- Impact of variation of dielectric permittivity (ϵ_r).

4.3.2 Performance summary

In order to demonstrate the characteristics of the proposed dual-band antenna, the computed input reflection coefficient and radiation patterns of the optimised standalone antenna (unit-cell), operational at the X-band, are presented in Figs. 4.7-4.8. The dimensions of the ground plane are kept equal to that of the unit-cell, and a substrate with dielectric permittivity (ϵ_r) of 2.2 was used in this optimised antenna model. The antenna supports well-defined dual-band operation with a maximum frequency ratio of 1.5:1. Consistent radiation patterns with low levels of cross-polarisation ($< -16dB$) are achieved at both the operational bands. Computed radiation efficiencies of 0.91 and 0.90 are obtained at the low and high frequency bands respectively. The inherent asymmetry of the comb-slot is largely responsible for the marginal tilt in the radiation pattern along the E-plane at the high frequency band (refer Fig. 4.8b). Bandwidths of 610 MHz and 1.1 GHz are achieved at the low and high frequency bands respectively. Further, the unit-cell of the antenna measures only $0.38\lambda_L \times 0.38\lambda_L$, at the low frequency band. This provides the possibility to achieve grating lobe free scanning up to a maximum (θ_{max}) of 60 degrees, as it satisfies the respective grid spacing requirement, $d_e = \lambda_{op} \ / \ (1 + sin(\theta_{max}))$. The full-wave numerical results illustrate the proposed dual-band antenna's capability for achieving good bandwidths and consistent radiation patterns, with a large frequency ratio and low-profile electrical dimensions.

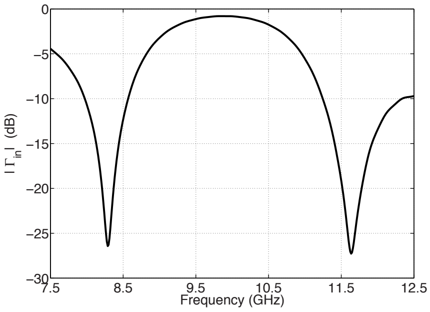

Figure 4.7: Computed input reflection coefficient ($|\Gamma_{in}|$) of the dual-band antenna.

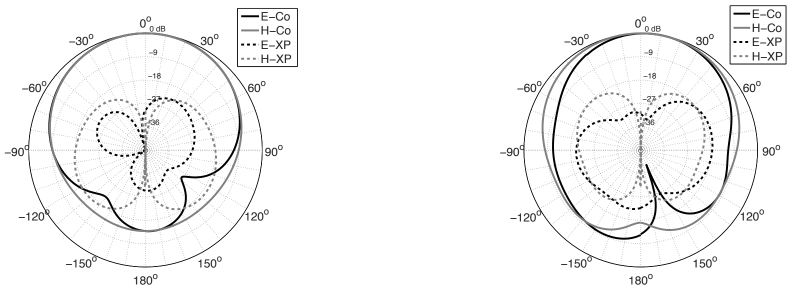

(a)

(b)

Figure 4.8: Computed radiation patterns of the stand-alone dual-band antenna. (a)- 8.2 GHz and (b)- 11.4 GHz.

The impact of the reactance balance offered by the *'lamppost'* feed on the sub-band bandwidths is demonstrated through the impedance plot of the optimised stand-alone antenna, shown in Fig. 4.9a. The optimised dual-band antenna must have a reactance characteristic which would remain 'flat' in both the operational bands, as per the reactance balance offered by the feeding architecture. The impedance response, presented in Fig. 4.9a, exhibits the exact behaviour as expected from the configuration. The corresponding VSWR plot is also presented in Fig. 4.9b. This 'flat' reactance response aids in achieving the bandwidths at the respective operational sub-bands, demonstrating the *'lamppost'* feed's effectiveness in improving bandwidths through the reactance balance mechanism. A novel feeding mechanism for slot-loaded patch antenna, which also enables bandwidth enhancement at the operational bands, has hence been introduced.

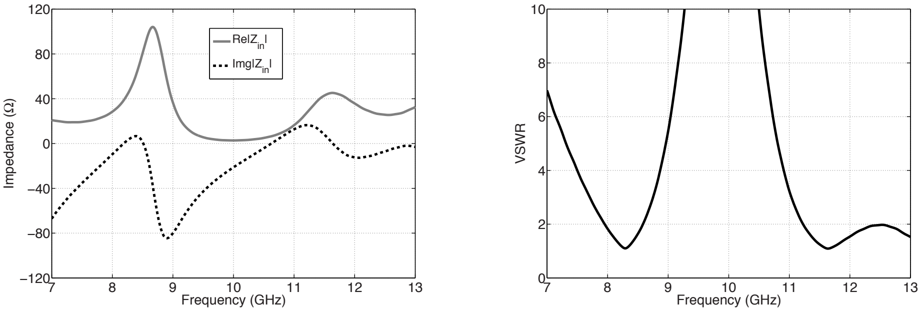

(a) (b)

Figure 4.9: (a)- Input impedance (Z_{in}) of the dual-band antenna. (b)- VSWR plot.

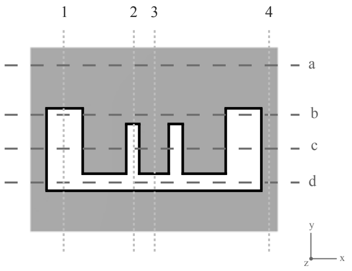

Figure 4.10: 2D field plot position marking. E-plane (y-z) and H-plane (x-z).

To discuss further on the antenna's performance characteristics, the impedance plot, shown in Fig. 4.9a, is considered first. The resonant bands, achieved with the comb-shaped patch (Fig. 4.2) exists close to the resonances achieved with the comb-slot-loaded patch antenna (Fig. 4.7). This makes it possible to use the slot's resonant characteristics at both the operational bands. The difference in the resonance placements, between Fig. 4.2 and Fig. 4.9a, is mainly due to the use of cavity and *'lamppost'* feed, along with the unit-cell dimensions, which are maintained to satisfy scanning requirements (The impedance response presented in Fig. 4.2 are with infinite substrate and ground plane). Another related inference is the difference in the slope of the reactance curves and the resonant resistance values obtained with the comb-slot-loaded patch antenna. The use of the *'lamppost'* feed reduces the slope of the reactance curves at the operational bands, as compared to that presented in Fig. 4.2. Further, the resistance (Re(Z)) levels at the operational bands also exhibit values suitable for matching with standard characteristics impedances (50Ω). Both these characteristics aid in achieving the broader bandwidths at the sub-bands.

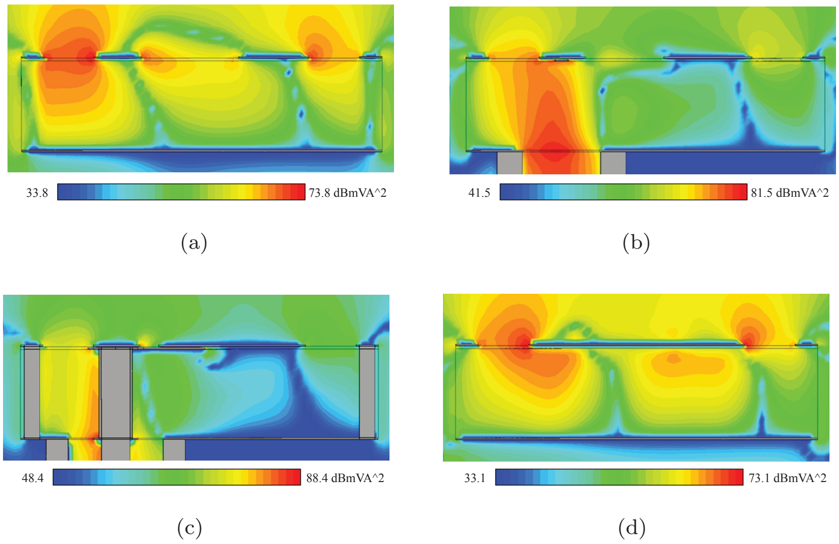

(a) (b) (c) (d)

Figure 4.11: Power flow distribution (P_z). E-plane cuts at 8.2 GHz. From points 1 to 4.

Secondly, to demonstrate the active role of the slot-based magnetic radiation in the overall radiation mechanism, the characteristics of the power flow distribution along the vertical axis (z-axis) of the antenna's unit-cell is considered. The two-dimensional E- and H-plane cuts of the P_z component at different positions on the patch, as shown in Fig. 4.10, at both the operational bands, are presented in Figs. 4.11-4.14. Considering Figs. 4.11-4.14, it is clearly demonstrated that the net outward power flow (along the positive z-axis) exists both at the ends of the metallic patch and inside the slot regions. The characteristic is maintained in all the progressive cuts along the

E-plane (points 1,2,3,4 in Fig. 4.10), which also show the variation in the slot gap size, as per the position.

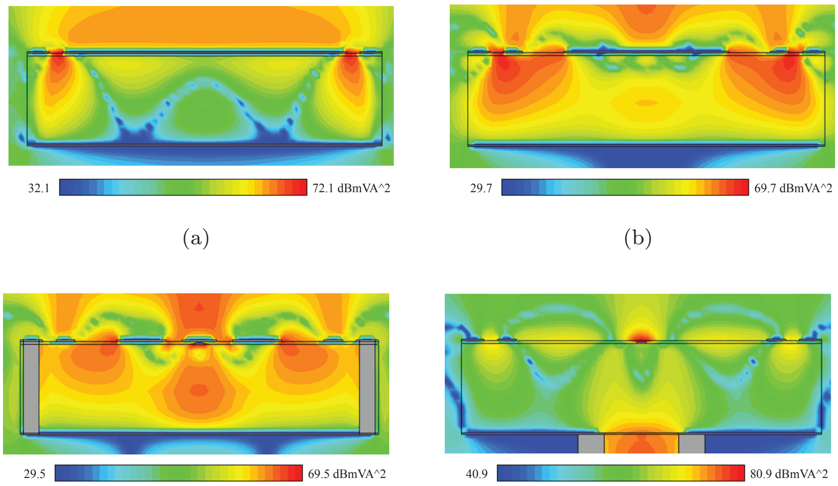

(a) (b)

(c) (d)

Figure 4.12: Power flow distribution (P_z). H-plane cuts at 8.2 GHz. From points a to d.

The H-plane cuts (points a,b,c,d in Fig. 4.10) reiterate this behaviour from a difference planar perspective. The presence of the slot-based radiation, as shown through the progressive cuts from points a to d, is also clearly illustrated. The behavioural patterns exhibits similar characteristics at the high frequency band (Figs. 4.13-4.14) for both the E- and H-plane cuts. The main difference being the comparatively stronger presence of the P_z component in the smaller arms at the low frequency band of operation. The plots strongly reiterate the role of the slot-based radiation at both the operational bands. Hence, the fundamental and major difference of the proposed comb-slot-loaded patch antenna, compared to the other dual- or multi-band patch antennas, has been illustrated.

Finally, the effectiveness of the cavity in confining the fields within its geometrical area is demonstrated through the cross-sectional cuts of the computed E-field distribution at the centre frequencies of the operational bands, shown in Fig. 4.15. The x-y plane cuts (refer Fig. 4.4a for axis) presented are at a height of 4.21 mm from the ground plane, which corresponds to the position of the metal patch on the substrate in the simulated antenna model. The plots illustrate the cavity's capability in confining the field within its region, at both the bands, which in turn would reduce the mutual coupling between the antennas when implemented in arrays. The substrate dimensions, for this plot, were kept larger than that of the unit-cell for the purpose of illustration.

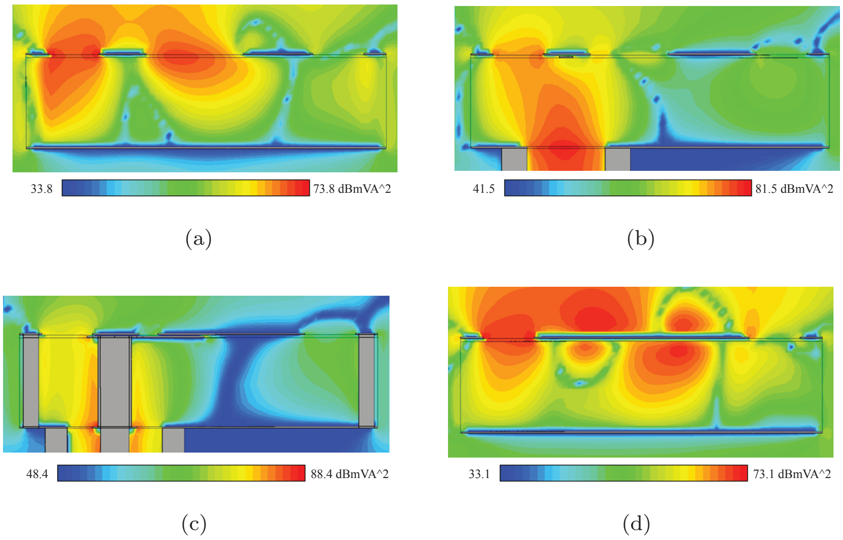

Figure 4.13: Power flow distribution (P_z). E-plane cuts at 11.4 GHz. From points 1 to 4.

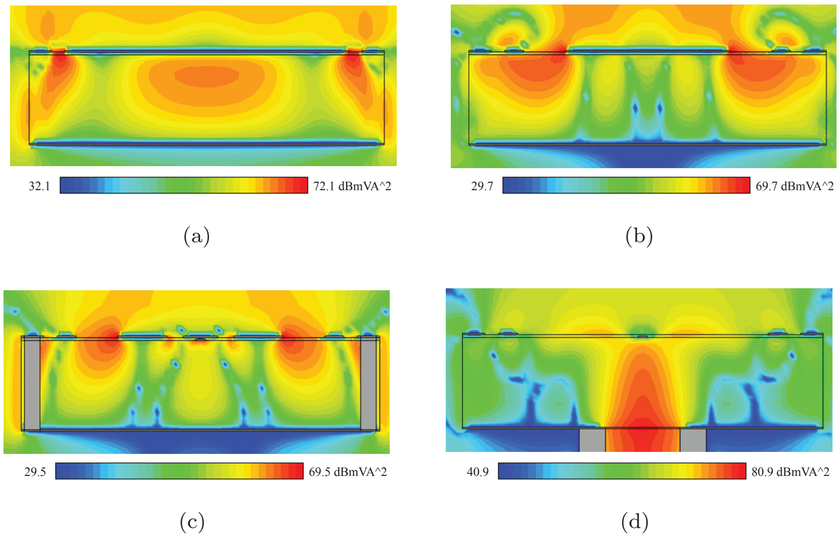

Figure 4.14: Power flow distribution (P_z). H-plane cuts at 11.4 GHz. From points a to d.

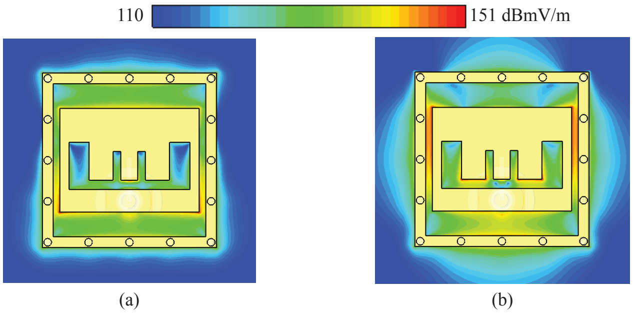

Figure 4.15: E-field (tangential-component) distribution at the operational bands. (a)- 8.2 GHz and (b)- 11.4 GHz.

4.4 Array analysis

The analysis and optimisation of the proposed dual-band antenna in infinite, linear and planar arrays are described in this section.

4.4.1 Infinite array optimisation

The first step in the array analysis involves the evaluation and optimisation of the antenna performance in infinite array. The maintenance of the impedance matching characteristics over wide scanning angles is indispensable for any array antenna. Hence, the infinite array simulations primarily focussed on the sustenance of the dual-band characteristics of the proposed antenna, up to a maximum of 60 degrees, along both the principal E- and H-planes. This requirement on the maximum scanning angle (θ_{max}) is motivated due to the same reasons as mentioned in the previous section. The frequency domain solver of CST-MWS was used for the analysis and performance optimisation of the antenna in infinite array. The Floquet modes based analysis of the infinite array is not available with the time domain solver of CST-MWS. Although, the unit-cell, presented in the previous section, was optimised for both the impedance and radiation pattern characteristics, marginal retuning of the patch's dimensions and the diameter of the matching ring (d_p), was still required when implemented in the infinite array. This formed the major part of the optimisation procedure, and was especially important for maintaining the dual-band characteristics with scanning. The importance of the metal cavity in maintaining the dual-band performance in infinite array is presented in Appendix A.

The antenna with the optimised dimensions (for infinite array) retains the dual-band characteristic up to a maximum of 60 degrees along both the E- and H-planes. The variation of the active reflection coefficient ($|\Gamma_{act}|$) with scanning angle is presented in Fig. 4.16a. The performance is more affected at the high frequency band along the E-plane, particularly for a scan of 60 degrees. However, the dual-band performance is still maintained for this scanning angle, along the H-plane. Wide-angle impedance matching up to 45^o and 60^o are achieved along the E- and H-planes respectively. The corresponding VSWR curves with scanning are presented in Fig. 4.16b, supporting the wide-angle dual-band impedance matching characteristics. Table 4.1 provides the optimised antenna dimensions (for the infinite array) comparing it with the starting values of the dimensions.

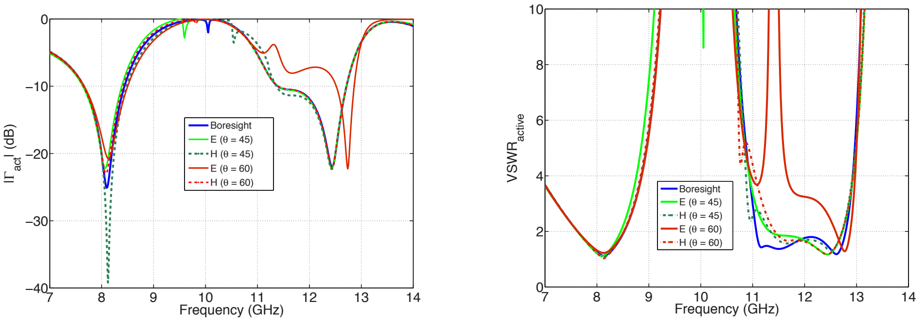

(a) (b)

Figure 4.16: (a)- Variation of the active reflection coefficient ($|\Gamma_{act}|$) and (b)- variation of the active VSWR, of the dual-band antenna with scanning angles in infinite array.

Table 4.1: Optimised antenna dimensions (infinite array)

Dimension	Start value (mm)	Optimised value (mm)
L	15	13.0
W	11.6	10.2
U_{cell}	20	17
d_p	2.7	2.51
w_s	0.5	0.45
l_s	5	4.35
t	4.22	4.22
ϵ_r	2.2	2.2

4.4.2 Finite arrays

The modelling and optimisation of finite-sized linear and planar arrays, essential for practical applications, were carried out as the next step in the array analysis.

The array element's dimensions were re-optimised, albeit only marginally, for both the linear and planar arrays. The principal aim of this research step was with the development of experimental prototypes to demonstrate the validity and practicality of the proposed antenna concepts. Apart from this, finite-sized arrays provide useful insights into the difference in performance between the edge and centrally embedded elements, impact of truncation on the radiation patterns, differences in the mutual coupling between elements along the principal operational planes and the array's scanning capability.

Linear arrays

Firstly, 13-element linear E-plane and H-plane arrays were modelled and optimised. The corresponding electrical lengths of both the E- and H-plane linear arrays were more than $5\lambda_L$, where λ_L is defined at the low frequency band. These lengths were chosen based on the analysis of the impact of truncation on the performance of linear arrays with dual-band radiators, provided in [60]. The use of linear arrays provide useful insights into the differences in coupling behaviour and impact of the embedded radiation patterns between the E- and H-planes. In this regard, the analysis of the performance in linear arrays, served as an intermediate step, following which the development of finite-sized planar arrays were carried out.

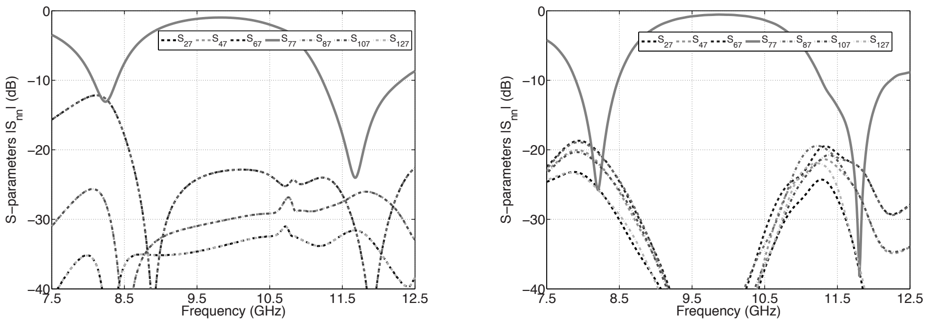

(a)

(b)

Figure 4.17: Simulated embedded reflection coefficient ($|\Gamma_{emb}|$) and mutual coupling characteristics of the centre element (no: 7) in (a)- linear E-plane array and (b)- H-plane linear array.

The embedded reflection coefficient of the centre element of the E- and H-plane linear arrays, along with the mutual coupling behaviour in the respective cases are presented in Fig. 4.17. As expected, the coupling between adjacent radiators was higher in the E-plane array compared to the same in the H-plane array. Despite very small inter-element spacing ($0.38\lambda_L$) at the low frequency band, the maximum coupling levels were still less than -13 dB in both the E- and H-planes arrays (refer Fig. 4.17). This demonstrates the vitality of the cavity-backed architecture in both cases.

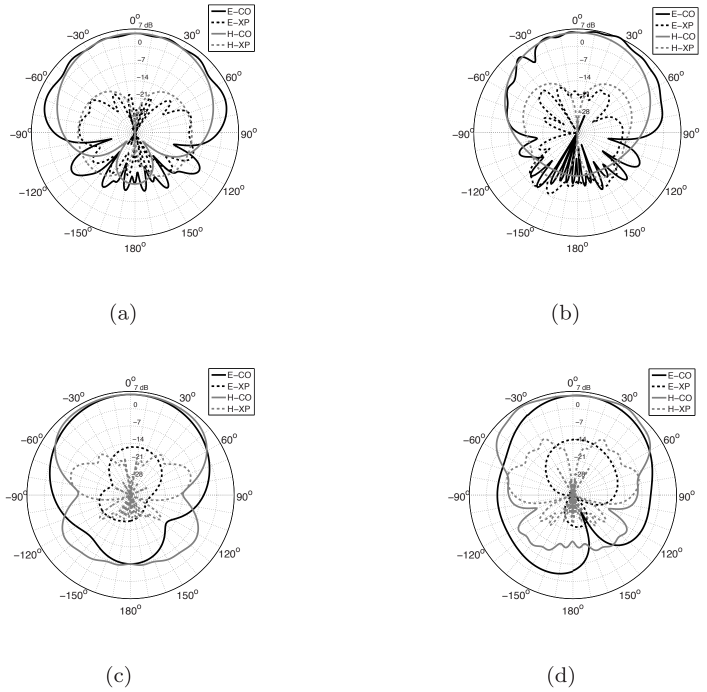

(a)

(b)

(c)

(d)

Figure 4.18: Computed embedded radiation patterns of the centre element (no:7). (a)- E-plane linear array at 8.3 GHz (f_L), (b)- E-plane linear array at 11.6 GHz (f_H), (c)- H-plane linear array at 8.3 GHz (f_L) and (d)- H-plane linear array at 11.6 GHz (f_H).

The low levels of coupling exhibited in both the cases ensure absence of any drastic negative impact on the embedded patterns, which can be verified from the computed embedded radiation patterns of the centre element (no:7), at the operational bands, for both the E-plane and H-plane linear arrays, presented in Fig. 4.18. Broad patterns are achieved along the respective array planes in both the cases. Furthermore, the cross-polarisation levels are maintained less than -16 dB in both the E- and H-plane embedded element patters. The element's symmetry along the H-plane is also reiterated in the cross-polarisation patterns, in both the linear arrays.

Planar array

The final step in the array analysis was the design and optimisation of planar finite-sized array model for experimental demonstration. The maintenance of the dual-band operation with a frequency ratio 1.5:1, low mutual coupling along both the principal (E/H) planes and wide angle scanning up to a maximum of 60 degrees at both the operational bands, were the main goals for the optimisation of the antenna performance.

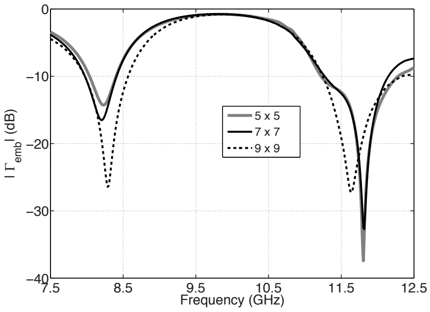

Figure 4.19: Variation of the embedded reflection coefficient (Γ_{emb}) of the centre element in finite-sized planar arrays (Simulated).

Finite-sized arrays of different sizes (5×5, 7×7, 9×9 and 11×11) with rectangular grids were modelled. The array needs to be large enough to emulate large or infinite array and also capture the difference in performance between the edge and centrally embedded elements. A planar 9×9 array was finalised for the concept demonstrations as the array's electrical and physical dimensions ensured good convergence with the results of infinite array. This is illustrated through Fig. 4.19, which shows the variation of the embedded reflection coefficient ($|\Gamma_{emb}|$) of the centre element of the different planar array sizes investigated. Although, well-defined dual-band characteristics were achieved with both the 5×5 and 7×7 arrays, a planar array of 9×9 was still required, in this case, to emulate the dual-band characteristics achieved at boresight in infinite array. However, maintenance of larger array sizes (greater than 9×9) did not result in noticeable difference of the embedded reflection coefficient. The optimised 9×9 array supports a maximum frequency ratio of 1.55:1, with bandwidths of 570 MHz (7.9-8.47 GHz) and 1.07 GHz (11.15-12.22 GHz) at the operational bands.

The mutual coupling behaviour along the principal E- and H-planes was analysed next. Wide-angle scanning requires low levels of mutual coupling between the antennas at both the operational bands. The antenna unit-cell optimised for performance in the planar array maintains very small inter-element spacing (0.38λ), at the low frequency band. However, even with this small inter-element spacing, the mutual coupling levels between adjacent elements were still maintained less than -14 dB, at the low frequency band, along both the E- and H-planes. This is illustrated through Fig. 4.20, which presents the details of the coupling characteristics of the centre element (no: 41) in the planar 9 × 9 array. Coupling characteristics along the E- and H-planes, exhibit performances similar to those obtained with E- and H-plane linear arrays respectively. Further, it is also clear that the coupling between elements after the second adjacent pair can be neglected from consideration for the calculations of active reflection coefficient ($|\Gamma_{act}|$), if required. This is strongly motivated due to the drop in the mutual coupling levels to well below -26 to -30 dB at both the bands, beyond the second adjacent element from the centre element.

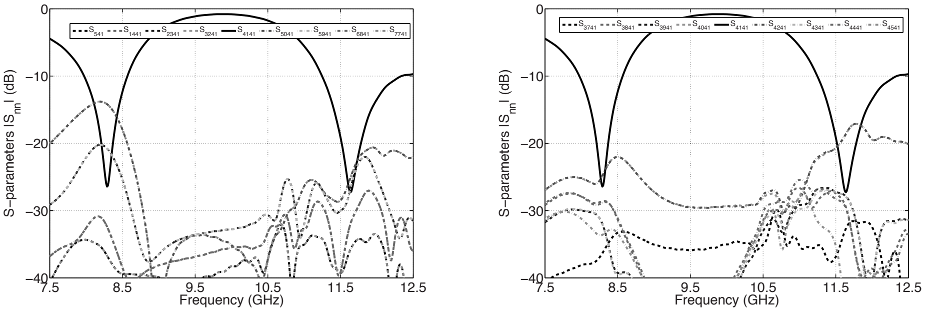

(a) (b)

Figure 4.20: Computed mutual coupling characteristics of centre element (no: 41) in planar (9 × 9) array. (a)- E-plane coupling and (b)- H-plane coupling.

The optimised unit-cell dimensions and the low levels of coupling, along both the E- and H-planes of operation, were extremely beneficial for the performance of the planar array. The radiation patterns of the centre element in the planar array were thus less perturbed by the coupling between the array antennas. This is illustrated through the embedded radiation patterns of the centre element at both the operational bands, in Fig. 4.21. The patterns maintain consistent and broad characteristics suitable for supporting wide-angle scanning. Further, low levels of cross polarisation, below -17 dB, were achieved along both the E- and H-planes. The scanning performance of the planar array is covered in the measurements section. The optimised values of the key dimensions of the unit-cell of the array antenna are presented in Table 4.2 (refer Fig. 4.1 for dimension markings).

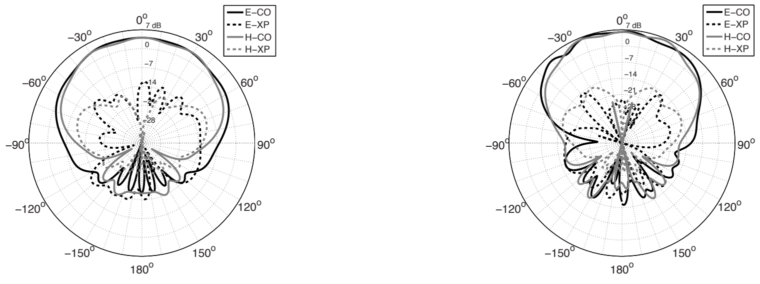

(a) (b)

Figure 4.21: Computed embedded radiation patterns of the centre element (no: 41) of the planar (9 × 9) array. (a)- 8.3 GHz (f_L) and (b)- 11.5 GHz (f_H)

Table 4.2: Comparison of optimised dual-band antenna dimensions

Dimension	Stand-alone	Infinite array	Planar (9 × 9) array
L	12.8	13.0	12.5
W	9.5	10.2	9.5
U_{cell}	16	17	14.5
d_p	2.5	2.51	2.5
w_s	0.425	0.45	0.42
l_s	4.1	4.35	4
w_1	1.86	1.88	1.9
w_2	0.71	0.68	0.7
l_1	4.3	4.35	4.3
l_2	2.63	2.6	2.63
t	4.22	4.22	4.22
ϵ_r	2.2	2.2	2.2

4.5 Concept demonstration

4.5.1 Measurement set-up

The linear and planar array measurements were carried out in the DUCAT anechoic chamber at TU-Delft. The chamber is optimised for measurements in the 4-40 GHz range. A standard X-band horn antenna was used as the reference for both the linear and planar array measurements. A step increment of 10 MHz was used for the reflection coefficient ($|\Gamma|$) and mutual coupling measurements, and a 1 degree step was used for the radiation pattern measurements.

4.5.2 Linear arrays

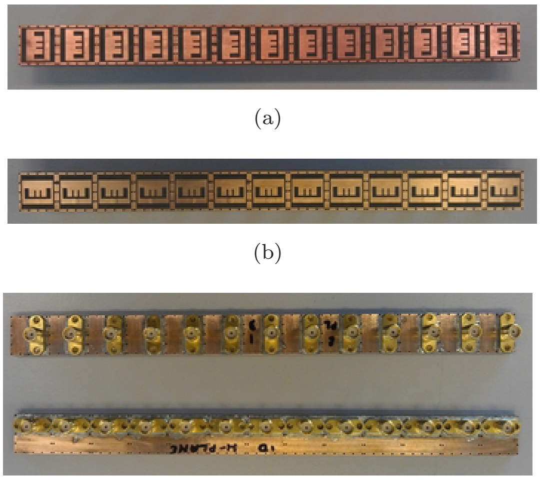

(a)

(b)

(c)

Figure 4.22: Fabricated linear (1 × 13) array prototypes. (a)- E-plane array, (b)- H-plane array and (c)- connector assembly for E- and H-plane arrays.

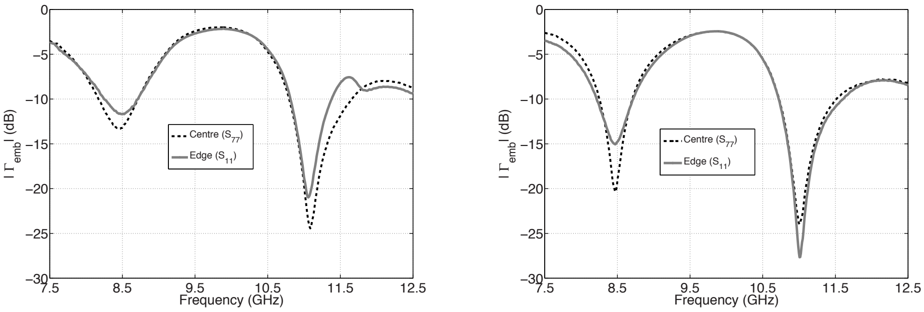

(a)

(b)

Figure 4.23: Measured embedded reflection coefficient ($|\Gamma_{emb}|$) of the centre (no: 7) and edge (no: 1) elements. (a)- linear E-plane array and (b)- linear H-plane array

The fabricated prototypes of the 13-element linear E- and H-plane arrays, along with the respective connector assemblies for the array elements are shown in Fig. 4.22.

Measured reflection coefficient plots of the centre and edge elements of both the E- and H-plane arrays are presented in Fig. 4.23. The dual-band characteristic is well-maintained in both the cases, with the impedance match performance of both the centre and edge elements exhibiting good conformance. The mutual coupling, which is more dominant along the E-plane, as presented in Section 4.4.2, affects the impedance matching at the low frequency band, particularly that of the edge element (no: 1), in the E-plane array. This however, is not present in the H-plane array, due to the comparatively low levels of coupling between array elements along the H-plane. Measured bandwidths of 590 MHz and 830 MHz are achieved at the operational bands in the E-plane array, with a maximum frequency ratio of 1.43:1. On the other hand, the H-plane array supports a maximum frequency ratio of 1.41:1, with sub-band bandwidths of 520 MHz and 870 MHz respectively.

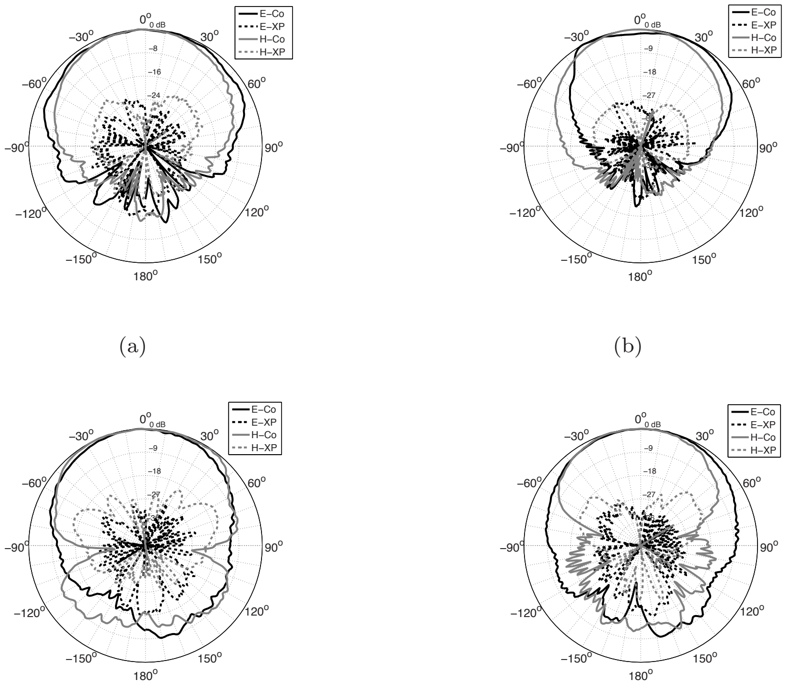

(a) (b)

(c) (d)

Figure 4.24: Measured embedded radiation pattern of centre element (no: 7) in linear arrays. (a)- E-plane array at 8.5 GHz, (b)- E-plane array at 11.0 GHz, (c)- H-plane array at 8.5 GHz and (d)- H-plane array at 11.0 GHz.

The measured embedded patterns of the centre element of the E- and H-plane arrays are analysed next. Figures 4.24(a-d) are used as reference for the upcoming discussion. The embedded radiation patterns of the centre element (no: 7) of the E-plane array (Fig. 4.24a-b) are consistent at both the bands. The tilt or asymmetry along the E-plane at the high frequency band, is still existent in the linear array. On the other hand, the co- and cross-polarisation patterns exhibit symmetry along the H-plane, in both the bands. The radiation patterns in the H-plane array are more affected at the high frequency band, resulting in the pattern along H-plane being more directive, as compared to the same at the low frequency band. This behaviour is not observed in the patterns along the E-plane, as the array elements are not not loaded along the E-plane. The cross-polarisation levels are maintained less than -17 dB, over the entire angular range, at the operational bands, in both the E- and H-plane arrays.

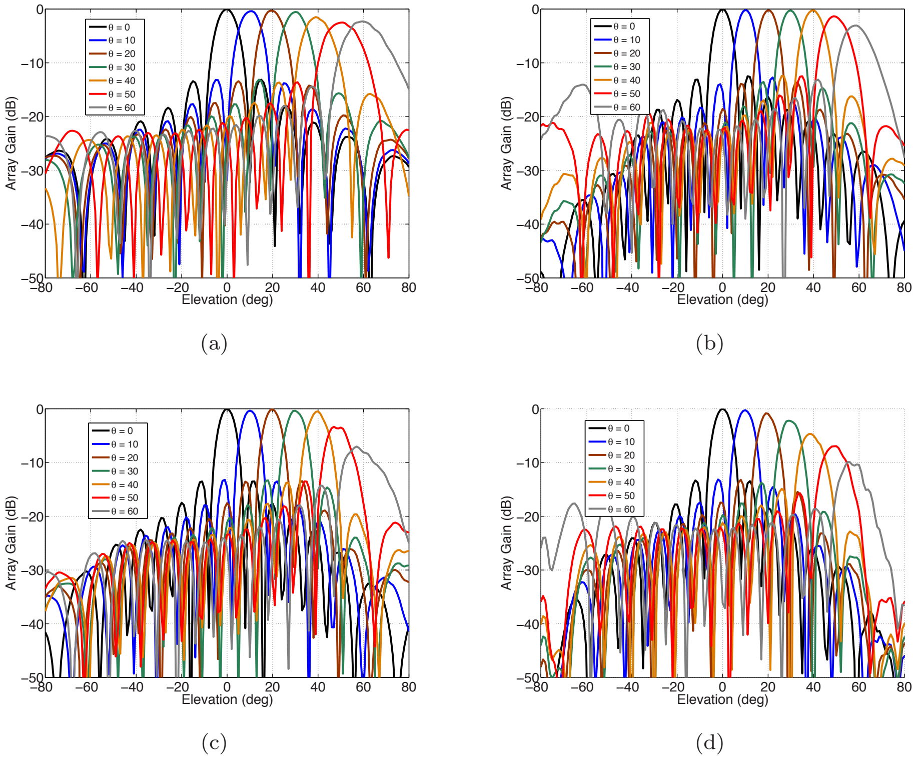

(a) (b)

(c) (d)

Figure 4.25: Measured scanning performance. (a)- E-plane array at 8.5 GHz, (b)- E-plane array at 11.0 GHz, (c)- H-plane array at 8.5 GHz and (d)- H-plane array at 11.0 GHz.

Finally, wide-angle scanning performance up to a maximum of 60 degrees 50 degrees are achieved in the E-plane array at the low and high frequency bands respectively (Fig. 4.25a-b). The scanning performance of the H-plane array though is limited due to the large scan loss at the high frequency band. The directive embedded H-plane pattern in the linear H-plane array, as mentioned above, is the main reason behind the large ($\geq -8dB$) scan loss which occurs when scanning above 40 degrees (Fig. 4.25d). Nevertheless, scanning up to a maximum of 40 degrees is still possible with the linear H-plane array, at the high frequency band. Additional plots on the difference in the embedded radiation patterns between the centre and edge elements, in both the E- and H-plane linear arrays, are provided in Appendix A.

4.5.3 Planar array

The experimental results of the planar array are presented and analysed in this section. The fabricated planar 81-element array prototype, along with its connector assembly, is shown in Fig. 4.26. The 9×9 array with rectangular grid has individual SMA connectors for all the array elements and measures $132mm \times 132mm$. The thickness of the array face measures only 4.3 mm ($0.12\lambda_L$). The anechoic chamber measurement set-up used for the array measurements is shown in Fig. 4.26c. The array-under-test (AUT) was placed on the pedestal of the vertical turn table, held in place by means of a tailor-made foam support frame. The azimuthal rotation of the turn table was used to measure the radiation patterns along the principal planes of interest (E-, H- and diagonal planes).

The embedded reflection coefficient ($|\Gamma_{emb}|$) and radiation patterns of elements at different positions in the array were measured. The performances of the active reflection coefficient, mutual coupling and embedded patterns of the centre element (no: 41) are presented and analysed in this section. A comparative plot illustrating the conformance between the simulated and measured embedded reflection coefficient of the centre element of the planar array is presented in Fig. 4.27. The active reflection coefficient ($|\Gamma_{act}|$) in infinite array is also included in the plot for comparison. The measured performance exhibits good conformance with those of the simulations. However, the frequency ratio is slightly reduced in the measurements. The main reason for this discrepancy was found to be the difference in the effective dielectric permittivity (ϵ_{eff}) of the fabricated antenna substrate. The CuClad adhesive layers used for the fabrication have permittivity ($\epsilon_r = 3$) higher than that of the substrate ($\epsilon_r = 2.2$), used for the antenna modelling, which contributes to this difference. The slightly reduced bandwidths at the sub-bands is also a consequence of this difference in permittivity. Measured bandwidths of 360 MHz (8.14-8.5 GHz) and 650 MHz (10.65-11.31 GHz) are achieved at the sub-bands, supporting a maximum frequency ratio of 1.4:1.

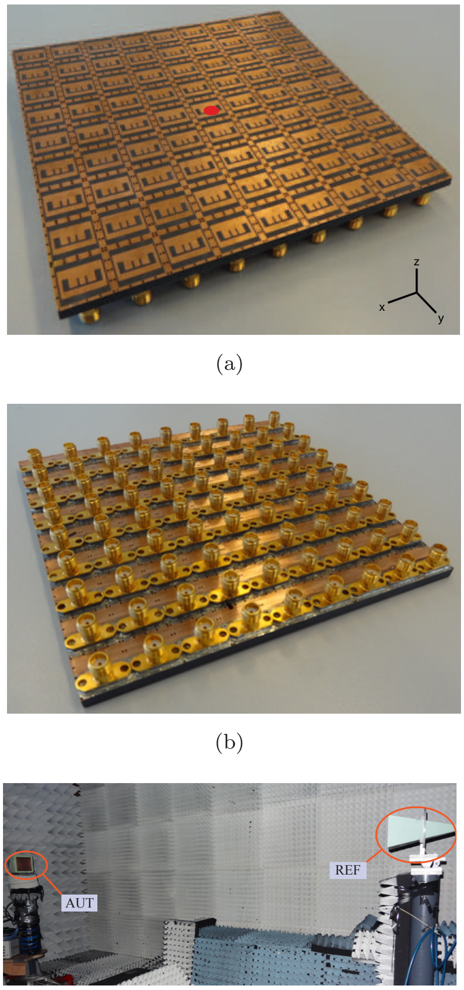

(a)

(b)

(c)

Figure 4.26: Fabricated planar 81-element array prototypes. (a)- array face, (b)- connector assembly and (c)- anechoic chamber set-up (DUCAT).

The mutual coupling characteristics are analysed next. The centre element's embedded reflection coefficient (Γ_{emb}), with the other ports terminated in matched loads, was measured, following which a 1 × 24 port switch was used for the measuring the mutual coupling between the centre element (no: 41) and the other array elements. The active reflection coefficient ($|\Gamma_{act}|$) of the centre element at boresight, calculated based on these measurements, and the coupling characteristics, along the E- and H-planes, are presented in Fig. 4.28. The details of the set-up used for the coupling measurements are provided in Appendix A.

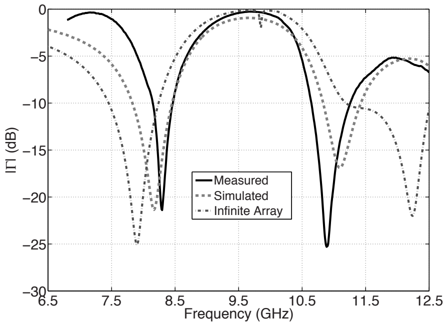

Figure 4.27: Simulated vs. measured embedded reflection coefficient ($|\Gamma_{emb}|$) of centre element (no:41).

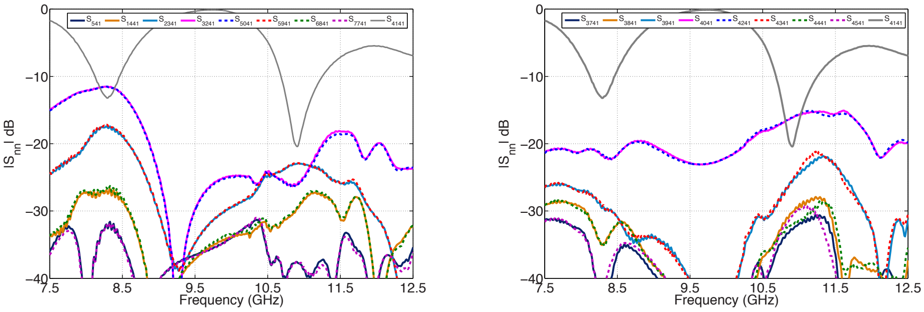

(a)

(b)

Figure 4.28: Measured active reflection coefficient ($|\Gamma_{act}|$) and coupling characteristics of centre element (no: 41) of planar array . (a)- E-plane and (b)- H-plane.

Yet again, the measured coupling performances exhibit characteristics similar to those of the simulations. As expected, the E-plane coupling is higher than the H-plane coupling and is also slightly asymmetric as compared to that of the H-plane, when considering the coupling between similar element pairs on either side of the centre element. It is worth mentioning, that even with very small inter-element spacing ($d_e = 0.38\lambda_L$), the measured coupling levels are kept well below -14 dB, even at the low frequency band of operation, along both the principal planes. This behaviour is a strong validation of the low mutual coupling characteristic of this "array-capable" antenna element.

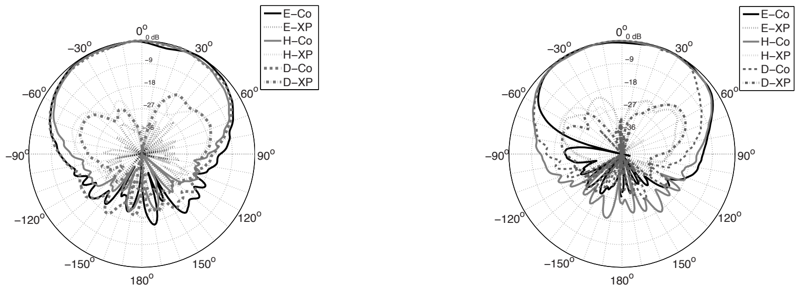

(a)

(b)

Figure 4.29: Measured embedded radiation pattern of the centre element (no: 41) in planar array. (a)- 8.3 GHz(f_L) and (b)- 11.0 GHz(f_H).

The next major validation deals with the antenna elements' embedded radiation patterns and the scanning performance of the array. The ability of the array antenna to maintain consistent and broad radiation patterns at both the bands is illustrated through Fig. 4.29, which presents the measured embedded patterns along the E- (y-z plane), H- (x-z plane) and diagonal planes (45^o). Refer Fig. 4.26a for axis details. The dual-band array antenna maintains consistent radiation patterns at both the operational bands with measured cross-polarisation [86] levels less than -17 dB in all the principal planes. The embedded patterns of the centre element are more symmetric along the E-plane, at the high frequency band, due to the averaging effect of the array. Nevertheless, the marginal asymmetry in the E-plane pattern is still existent even in the planar array. The pattern asymmetry is however more pronounced only for angles greater than -60 degrees and hence, would still be able to satisfy the scanning requirements ($\theta_{max} = \pm 60^o$) expected from the array. It is worth mentioning, that the measured patterns at other frequency points in the respective operational bands exhibit characteristics similar to the ones presented in Fig. 4.29. Additional plots illustrating the difference in the embedded patterns between edge and centrally embedded elements in the planar (9×9) array are provided in Appendix A. Comparative plots on the variation of the embedded reflection coefficient ($|\Gamma_{emb}|$) between elements at different positions in the array are also included in Appendix A.

Finally, the wide-angle scanning capability of the dual-band phased array, at both the operational bands, is demonstrated through Figs. 4.30-4.31. As a first step, the embedded patterns were measured for the elements of the planar array. Following this, the array patterns of the planar array for different scanning angles were calculated using a post processing Matlab script with the application of appropriate phase shifts to the array elements. The planar array was uniformly excited for all the cases presented here. The array exhibits wide-angle scanning up to a maximum of 60 degrees, along both the principal E- and H-planes, at both the operational bands. The unit-cell size at the high frequency band measures $0.58\lambda \times 0.58\lambda$, which is the main reason for the appearance of a visible grating lobe at -80 degrees, when scanned to the maximum scanning angle (θ_{max}) of 60 degrees. This grating lobe appears for 60 degree scans along both the E- and H-planes, at the high frequency band (refer Fig. 4.31). The peak sidelobe level is at around -12.5 dB and can be reduced with the application of suitable amplitude tapering, if required.

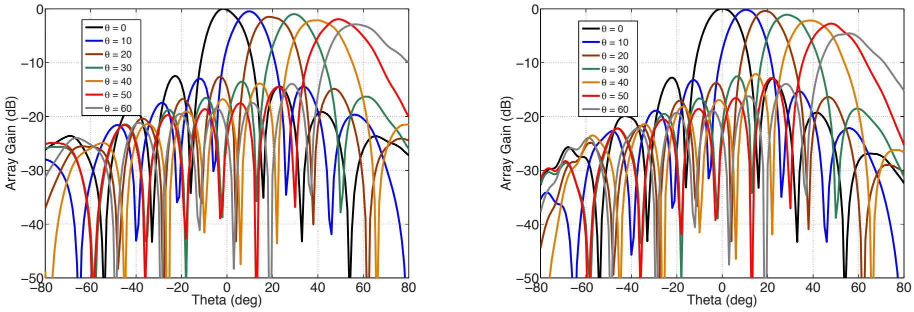

(a) (b)

Figure 4.30: Measured beam scanning performance at 8.3 GHz (f_L). (a)- E-plane and (b)- H-plane.

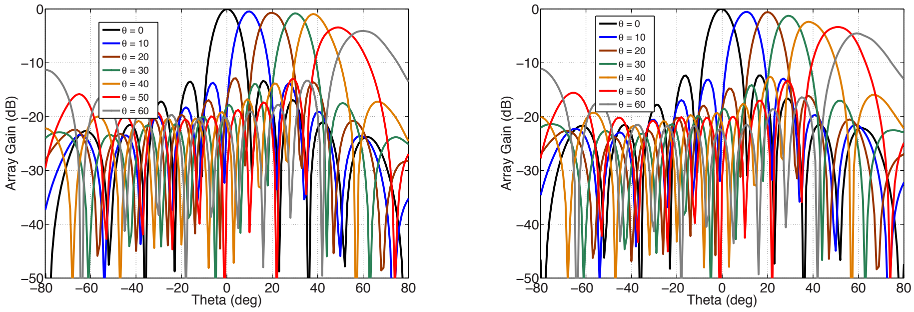

(a) (b)

Figure 4.31: Measured beam scanning performance at 11.0 GHz (f_H). (a)- E-plane and (b)- H-plane.

Another factor demonstrated in the scanning plots is that of the difference in the directive behaviour of the scan patterns observed at the low and high frequency bands. The finite size of the array, which electrically measures smaller at the low frequency band, causes patterns to be more broader, as compared to the scanning patterns obtained at the corresponding angles at the high frequency band (refer Figs. 4.30-4.31). Furthermore, for all scanning angles, at both the operational bands, the sidelobe levels are maintained less than -13 dB, even with a uniformly excited array. The compact electrical dimensions of the dual-band array antenna and its broad embedded element patterns collectively aid in achieving this wide-scan performance.

The demonstrated wide-scan performance in both the operational bands, even with a large frequency ratio (1.4:1), is a significant feature of this dual-band phased array. The novel characteristics of the proposed dual-band phased array, which includes operational bands with large frequency ratio, good sub-band bandwidths, consistent embedded radiation patterns, low levels of mutual coupling coupling and wide-angle scanning capability, have hence been experimentally validated, demonstrating the strength and potential of the proposed design concepts.

4.6 Symmetric comb-slot loaded patch antenna

In order to reduce the asymmetry of the radiation pattern, existent along the E-plane at the high frequency band, due to the inherent asymmetry of the comb-slot, the use of symmetric comb-slots on the patch was investigated. The inclusion of the additional slot, which resembles that of a mirror image, introduces slot symmetry along the E-plane as well. Snapshots of the simulated version (in CST-MWS) and the fabricated prototype are shown in Fig. 4.32. The optimisation of the antenna performance was carried out using the same design parameters as that of the original version. A dielectric permittivity (ϵ_r) of 2.2 was used for the substrate, similar to the original version. The measured input reflection coefficient ($|\Gamma_{in}|$) and radiation patterns are summarised in Figs. 4.33-4.34.

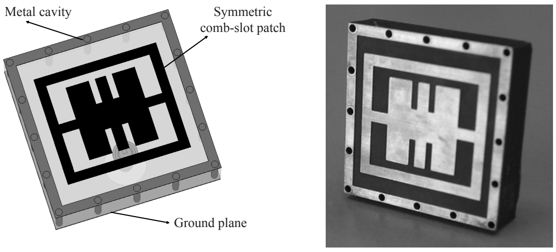

(a) (b)

Figure 4.32: Symmetric comb-slot loaded patch antenna. (a)- Simulated model and (b)- Fabricated prototype.

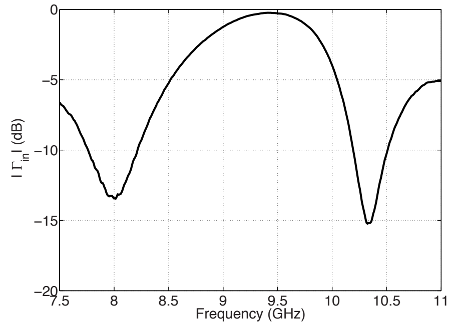

Figure 4.33: Measured input reflection coefficient ($|\Gamma_{in}|$) of the symmetric comb-slot loaded patch antenna.

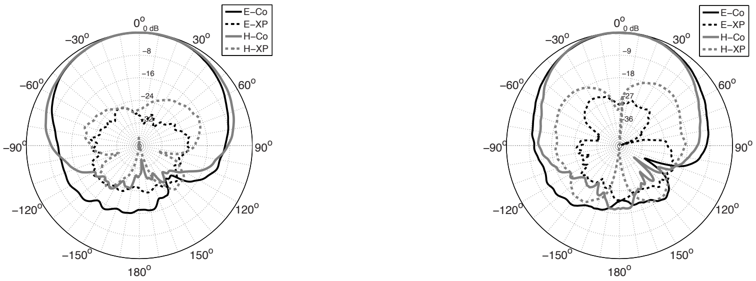

(a) (b)

Figure 4.34: Measured radiation patterns.(a)- 8.0 GHz and (b)- 10.3 GHz.

Based on the measured performance of this antenna element, it is evident that this variant of the proposed antenna also supports two well-defined operational bands, albeit with a slightly reduced frequency ratio (1.36:1). The antenna also exhibits consistent radiation patterns at both the operational bands. A comparative analysis between the radiation patterns at the high frequency band, presented in Fig 4.8b and Fig. 4.34b, illustrates the improvement in terms of the reduction of the pattern's asymmetry along the E-plane with the use of the symmetric comb-slot. The measured cross polarisation patterns (along E-plane) are also more symmetric, similar to that of the H-plane's cross polarisation pattern. Measured bandwidths of 470 MHz and 370 MHz are achieved at the low and high frequency bands respectively. The antenna's compact electrical dimensions, measuring only $0.40\lambda_L \times 0.40\lambda_L$, at the low frequency band, makes it attractive for array implementations as well. A linear

9-element H-plane array and a planar 27-element (3×9) array with the symmetric comb-slot loaded patch antennas were designed, fabricated and their performances experimentally validated. The arrays exhibit wide-angle scanning performances similar to that of arrays with the comb-slot loaded antennas, presented in the previous sections. The measured impedance and scanning performances of both the linear and planar arrays are summarised in Appendix B.

4.7 Summary

In this chapter a novel concept of dual-band radiator suitable for array applications is proposed. Based on this concept dual-band wide-angle-scanning arrays have been developed and their performances verified experimentally. The main contributions are summarised as follows.

The comb-slot-loaded patch antenna has been developed as an array element with a special emphasis on achieving low-profile electrical dimensions, maintenance of large frequency ratio between operational bands, and consistent radiation patterns suitable for wide-scan array applications. A concept to combine electric and magnetic radiator characteristics in a single antenna has been applied to the development of a dual-band patch antenna. To realise a magnetic radiator in a patch, a wide comb-shaped slot has been introduced. This enables the use of both the slot-based magnetic excitation and the patch's electrical radiation characteristics in the overall radiation mechanism. The shape and sizes of both radiators (electric and magnetic ones) have been selected to support two operational frequency bands. While the combination of electric and magnetic radiators in a single element is the first crucial aspect of the concept, a novel *'lamppost'* feeding architecture, which offers simultaneous excitation of both electric and magnetic radiators, constitutes the other key aspect of the concept developed. The proposed feeding configuration also provides reactance balance through the capacitive and inductive components of the feeding apparatus, thereby achieving good bandwidths at the operational sub-bands. The proposed *'lamppost'* feed configuration provides a clear advantage compared to the existing and widely used slot or pin-fed excitations by aiding in achieving good bandwidths (between 400-700 MHz) at the operational bands. The well-known dual-slot antennas only offer a maximum of about 50-80 MHz.

As a second step, infinite array developments have been carried out for optimising the performance of the proposed dual-band antenna in arrays. The developments focussed on the maintenance of the dual-band characteristics over wide scanning angles. The antenna, with the optimised dimensions, sustains the dual-band characteristic up to a maximum scanning angle (θ_{max}) of 60 degrees along both the principal E- and H-planes of operation. This is a key feature of the antenna pivotal for the development of practical finite-sized linear and planar arrays. In comparison, the u-slot antennas are almost always non functional in arrays, even with the inclusion of metal cavities. Evaluation of the u-slot antennas in infinite arrays demonstrate distortion of the dual- or tri-band behaviour, with no impedance matching performance beyond $10 - 20^o$ off-broadside. On the other hand, the dual-band characteristic of the dual-slot-loaded patch antenna, due to the extremely small sub-band bandwidths, show large variation in the band placements for off-broadside scans.

Based on the infinite array simulations, linear 13-element E- and H-plane arrays and planar 81-element (9×9) array, operational in the X-band, with the proposed dual-band patch antennas were modelled and optimised for fabrication using full-wave numerical solver. This was followed by the development of the antenna and array prototypes for concept verification. The optimisation of the array performance took various practical fabrication related constraints, including the value of the dielectric permittivity (ϵ_r) and thicknesses of the substrates, into consideration, which avoided unwanted complications during production. The antenna concepts introduced in the chapter can also be scaled for operation in different target band(s) of interest, for example, different parts of X-band, S- or C-band. This can be accomplished by scaling and optimising the antenna dimensions as per the target band of operation.

To verify the design concepts, anechoic chamber measurements of the linear and planar arrays were carried out. The experimental results exhibit good conformance with the results of the full-wave simulations. The proposed antenna array's capability in maintaining the dual-band operation with large frequency ratio and good sub-band bandwidths was demonstrated though the measurements. The embedded radiation patterns of the array elements also show conformance with the respective simulation results. Most importantly, the planar array's capability to support wide-angle scanning up to a maximum of 60 degrees, along both the principal E- and H-planes has been verified. The scanning loss of the array at 60 degrees scanning angle is maintained less than -5 dB at both the operational bands. It is shown that the operational bandwidth within the whole scan remains at 360 MHz and 650 MHz at the low and high frequency operational bands respectively. This is noteworthy, as the wide-angle scanning is achieved at both the bands, even with a considerable frequency ratio (1.5:1) in between them.

The electrically compact dimensions of the dual-band array antenna and its development as an array antenna, instead of a conventional stand-alone antenna design, has facilitated in achieving this performance. Low levels of sidelobes (less than -13 dB) are achieved even with a uniformly excited planar array for all the scanning angles tested. The sidelobe levels can be further reduced (for eg. less than -30 dB, used in many practical cases of interest) with the application of Taylor or Dolph-Chebyshev tapering, as per the requirement and array size.

In addition to this, to correct the minor asymmetry, existent along the E-plane of the radiator, at the high frequency band, the use of a dual comb-slot loaded patch design, an extended variant of the original version, was investigated. Linear and planar array prototypes employing this variant of the dual-band antenna have also been developed and their performance experimentally validated demonstrating its array-capable feature.

The proposed array antenna design addresses the performance limitations of existing dual-band solutions, providing dual-band operation with large frequency ratio, consistent radiation patterns and low-profile electrical dimensions suitable for wide-scan applications. Despite the minor semblance of the comb-slot shape with that of the u-slot antenna, the difference in the radiation mechanism and characteristic has been comprehensibly demonstrated in the chapter. Furthermore, the u-slot antenna are non-functional in arrays requiring wide-angle scanning capability [40, 47]. Any demonstration of the u-slot antenna's capability to support frequency ratios greater than 1.3:1 with small unit-cell dimensions, suitable for array operations, are also absent in current literature.

Finally, the proposed dual-band antennas have simple single layer architectures, avoiding external components, like for example, PIN diodes or MEMS switches, which in turn introduce unwanted bias issues complicating and compromising array performance. The simple architecture is also a plus in terms of fabrication.

The concepts presented in this chapter provide new avenues to achieve 1) low-profile (*"array-capable"*) electrical dimensions of dual-band array antennas, 2) consistent radiation patterns at both operational bands, 3) impedance matching over large scanning angles, 4) improve sub-band bandwidths, 5) large frequency ratios and 6) wide-angle beam scanning capability.

Chapter 5

Multi-Band Radar and Communications Antenna

5.1 Scope of the research

The development of a multi-band antenna with performance characteristics suitable for its use in both hand-held/mobile communication devices and array applications is presented in this chapter. The improvement in terms of the frequency ratio (greater than 1.6-1.7:1), as compared to the one presented in the previous chapter, was the main design target addressed in this research step. In addition to this, the possibility of achieving extremely low-profile dimensions and support for omni-directional patterns, features attractive for application in hand-held SatComm user terminals, were also explored.

5.2 Versatile low-profile multi-band antenna

The proposed multi-band crossed L-bar antenna was developed to address the performance limitations existent in currently available multi-band antenna [39–42,46–48,78]. The limitations, as mentioned in the previous chapter, primarily relate to the large electrical dimensions, inconsistent radiation patterns, complex geometries, small frequency ratios and very narrow sub-band bandwidths.

The crossed L-bar antenna was developed as a multi-band antenna with performance characteristics suitable for its use as both a communications (as stand-alone) and radar antenna (in arrays). The proposed antenna's versatile features include 1) quad-band operation, 2) extremely low-profile electrical dimensions, 3) support for both patch-like and omni-directional radiation patterns and 4) inherent capability to enhance or suppress any desired resonance(s), as per requirements. These performance traits, along with its simple single-layer architecture, strongly contribute to the novelty of the antenna design. The concept details and working principle are described next.

5.2.1 Crossed L-bar antenna concept and architecture

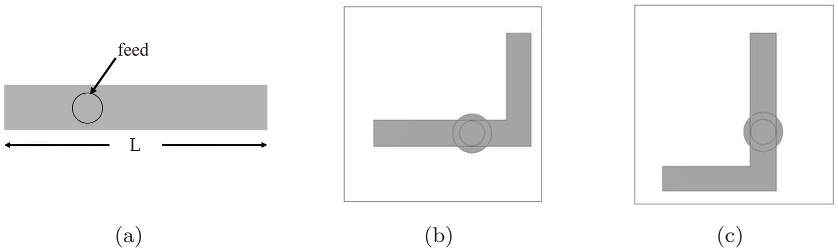

(a) (b) (c)

Figure 5.1: (a)- Dual-band radiating strip, (b)- L-bar patch in unit-cell (vertical polarisation version) and (c)- L-bar patch in unit-cell (horizontal polarisation version). Square represents unit-cell.

The basis of the antenna concept can be explained as follows. Consider a radiating patch with a rectangular strip-like geometry, as shown in Fig. 5.1a. Exciting this by means of an off-centred feed aids in supporting two operational modes, achieving dual-band operation. However, if frequency ratios greater than 1.5:1 are targeted, the length (L) of the patch needs to be large enough to accommodate both the modes, which, in turn, also increases the electrical lengths of the patch, especially at the high frequency band. Furthermore, it would be more attractive to have square unit-cells, instead of the elongated rectangular cells, for array implementations. This would facilitate in maintaining similar inter-element spacing, along both the E- and H-planes of the radiator, whereby similar levels of scanning can be achieved along both the principal planes, when used in arrays.

In order to accommodate the patch strip within a square unit-cell and still maintain dual-band operation, the strip-like radiating patch was modified into an L-bar. Two possible configurations (supporting vertical or horizontal polarization) can be achieved, as shown in Figs. 5.1b-c. To demonstrate the capability of the single L-bar configuration to support dual-band operation, a unit-cell size of $0.5\lambda \times 0.5\lambda$, defined at the Ku-band (12 GHz), was modelled. The L-bar's dimensions were accordingly modified to accommodate it inside this square unit-cell. The patch antenna modelling was carried out in CST-MWS, maintaining a characteristic impedance (Z_o) of 50Ω. The dual-band capability of this version of the antenna is clearly illustrated through the computed impedance plot of the single L-bar antenna, presented in Fig. 5.2. The corresponding surface current distribution at the operational bands are presented in Fig. 5.3. The variation in the current distribution (node-to-node spacing) between the operational bands is also evident. However, the electrical dimensions of the unit-cell at both the operational bands (18 GHz and 27 GHz) become very large ($> 0.75\lambda$), making the antenna unsuitable for array applications, a prime requirement of this research.

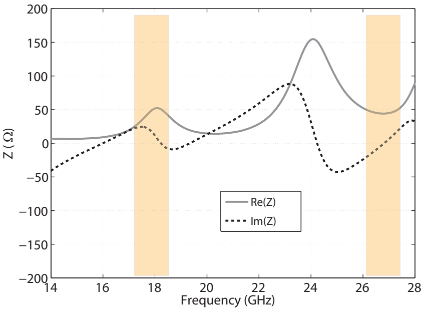

Figure 5.2: Impedance plot of single L-bar antenna.

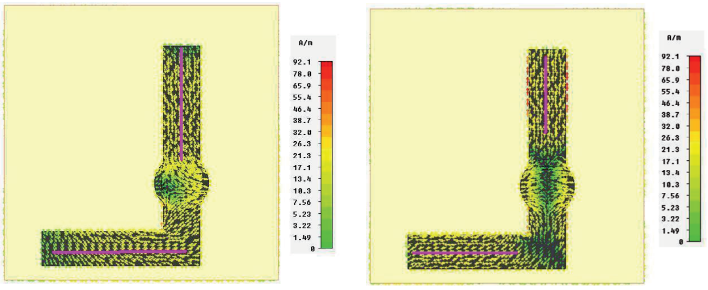

(a) (b)

Figure 5.3: Surface current distribution at the operational sub-bands. (a)- 18 GHz and (b)- 26.7 GHz.

To reduce the electrical dimensions of the antenna's unit-cell, the crossed L-bar geometry (Fig. 5.4a) was proposed. Use of the crossed L-bar geometry makes it possible to increase the electrical dimensions of the radiating aperture, which, in some manner, is analogous to the use of meander-line printed antenna designs, which are often used to reduce the electrical dimensions of the respective patch antennas. The resulting structure results in resonances at frequencies lower than the ones obtained with the single L-bar geometries. Furthermore, the radiating structure also becomes symmetric along the diagonal plane of operation. The impedance plot, demonstrating the crossed L-bar antenna's capability to support a maximum of four operational bands is shown in Fig. 5.6. The current distribution at the resonance frequencies and the current paths at which standing wave resonance takes place, for the crossed L-bar geometry, are shown in Fig. 5.5. A $0.5\lambda \times 0.5\lambda$ (defined at 12 GHz) unit-cell (U_{cell}) was maintained for this case as well.

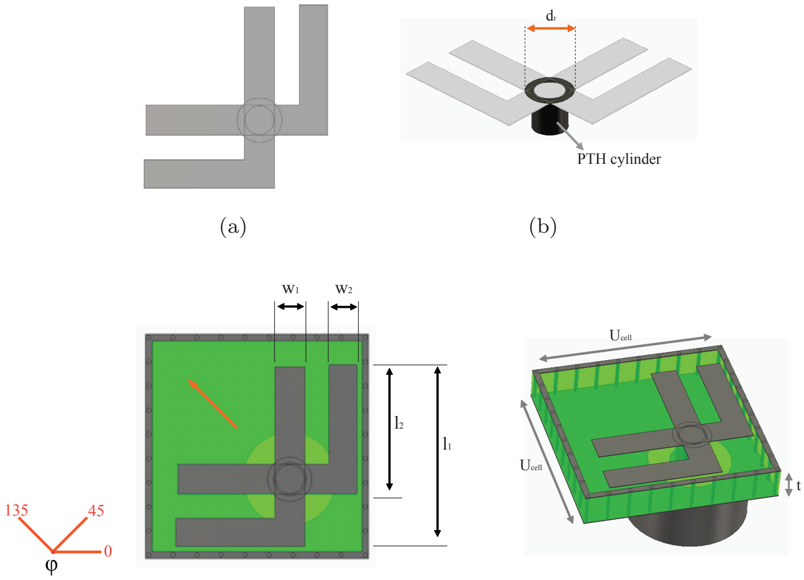

(a) (b)

(c) (d)

Figure 5.4: Architecture of the proposed crossed L-bar patch antenna. (a)- crossed L-bar geometry, (b)- feeding configuration, (c) - unit-cell of the crossed L-bar antenna (diagonally-polarised) and (d)- perspective view of the simulated antenna model. Substrates maintained semi-transparent for illustration. Arrowhead represents polarisation.

The introduction of the low frequency resonances, wherein the entire length of the radiation L-bar patch is made use of by the operational modes is clearly demonstrated through Figs.5.5a-b. The crossed L-bar geometry's capability to support additional resonances using the same unit-cell dimensions is hence illustrated. However, on the other hand, the radiation patterns, especially at the first and second operational bands, exhibit deformity, with the pattern maximum occurring at off-broadside angles. The cavity architecture is hence appended to the unit-cell design (Fig. 5.4d). The loop currents supported by the cavity aid in pattern correction, making it possible to achieve patch-like radiation patterns at the first and second operational bands. The other main functions of the cavity are described in the next section.

Other elements constituting the antenna's unit-cell geometry are as follows. The feed pin of the SMA connector runs through the plate-through-hole (PTH) cylinder, which is placed in the substrate (Fig. 5.4b). A field matching ring arrangement is present at the junction (refer Fig. 5.4b) where the feed pin meets the crossed L-bars, at the top of the substrate. The diameter of the SMA feed pin dictates the inner diameter of both the plate-through-hole (PTH) cylinder and the field matching ring. A dielectric substrate layer (with thickness 't') is used between the ground plane and the crossed L-bar patch (Fig. 5.4d). A novel concept for achieving quad-band operation and extremely low-profile electrical dimensions, with a simple single-layer geometry, is thus introduced.

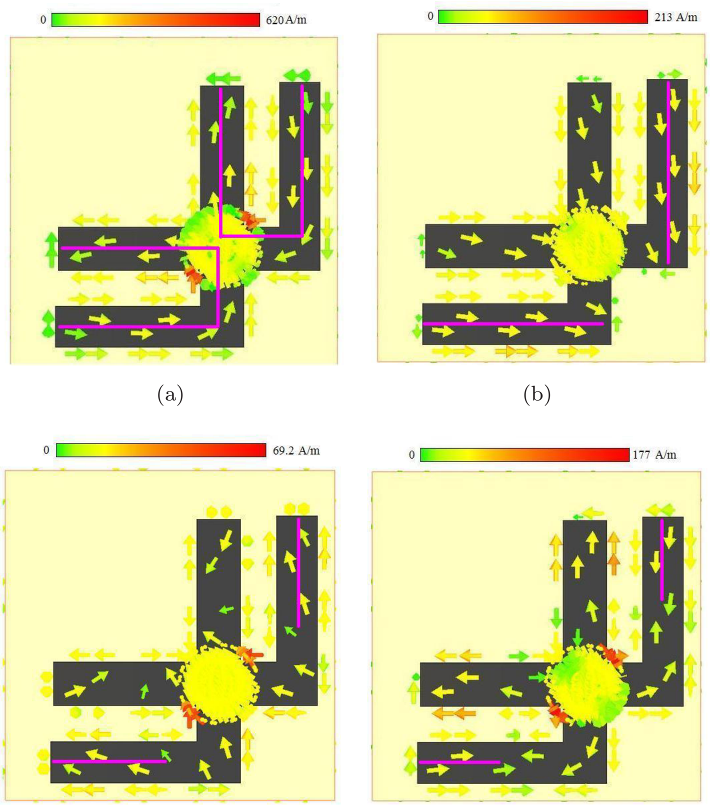

(a) (b)

(c) (d)

Figure 5.5: Surface current distribution on crossed L-bar aperture at the operational sub-bands. (a)- 9.1 GHz, (b)- 16.5 GHz, (c)- 24 GHz and (d)- 33.1 GHz. Pink marker represents node-to-node spacing.

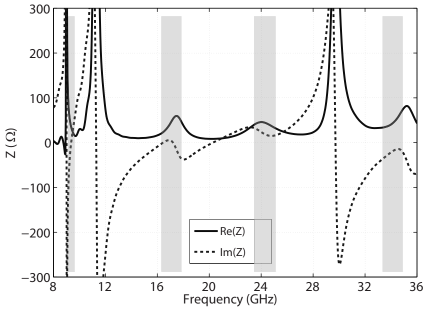

Figure 5.6: Impedance plot of the crossed L-bar antenna.

5.2.2 Functional characteristics

The key functional attributes of the crossed L-bar antenna can be explained as follows. Firstly, with the crossed L-bar geometry, the antenna supports quad-band operation. The additional resonances are introduced at frequencies lower than those obtained with the single L-bar geometry. The introduction of the resonances at lower frequencies results in extremely low-profile electrical dimensions of the unit-cell, especially at the first and second operational bands. Secondly, the bases of the L-bars, in conjunction with the respective side of the cavity, sustain orthogonal polarisation components, resulting in waves polarised along the diagonal plane of the radiator ($\phi = 135^o$ plane in Fig. 5.4c). This is an important distinction, inherent to the antenna design. In addition to this, the cavity architecture also helps in achieving patch-like radiation patterns, at the first and second operational bands, which are otherwise deformed, with the pattern maximum at off-broadside angles. The cavity architecture, hence forms a pivotal part of the antenna design, influencing its radiation characteristics, and also to reduce coupling between elements, when implemented in arrays. The discussion on the mutual coupling characteristics in array is presented in Section 5.5.2.

Impedance matching

The components of the feeding configuration, presented in Fig. 5.4b, are primarily responsible for achieving the required impedance matching at the operational bands. These include the plate-through-hole (PTH) cylinder and the field matching ring arrangement (refer Fig. 5.4b). The inductive reactance of the plate-through-hole (PTH) cylinder can be compensated with the capacitive reactance offered by the matching ring arrangement. As the inner diameter of the PTH cylinder is fixed, as previously mentioned, the height of the PTH cylinder (h_{PTH}) and the diameter of the matching ring (d_r) constitute the key parameters for optimising the antenna's impedance matching characteristics.

In order to demonstrate the proposed antenna's quad-band operational capability, the computed input reflection coefficient ($|\Gamma_{in}|$) is presented in Fig. 5.7. The full-wave numerical modelling was carried out in CST-Microwave Studio (MWS). The X- and K-bands were chosen for the antenna design, as they represent the bands of interest in the STARS project [8]. For the simulated antenna, standard SMA-connector dimensions were used for the feed model. A substrate with dielectric permittivity (ϵ_r) of 2.2 and thickness (t) of 1.824 mm, was used in the numerical model. The antenna's unit-cell dimensions measure $12.5mm \times 12.5mm$ $(0.38\lambda_L \times 0.38\lambda_L)$.

Following up, the computed surface current distributions at the operational bands, are presented in Fig. 5.8, to illustrate the presence of four operational modes, corresponding to the resonant bands. The modes' peak-to-peak spacing (marked with pink lines) at the sub-bands are at 12.9mm, 7.7mm, 5.2mm and 3.95mm, which, in turn, correspond to nearly half-a-wavelength ($\lambda/2$) spacing at the respective operational bands. This is a marked difference, compared to the usual dual- or multi-band designs, wherein only the first and third modes are made use of to achieve patch-like radiation patterns [41, 42].

It can also be noticed that the operational bands are well-separated (in frequency) with good isolation. The quad-band capability achieved with a simple single-layer architecture, is a significant standpoint of the proposed antenna design. A demonstration of the antenna's flexible resonance capability is presented in Appendix C.

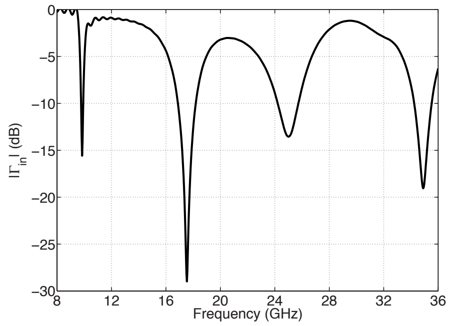

Figure 5.7: Computed input reflection coefficient ($|\Gamma_{in}|$) of the quad-band version of the crossed L-bar patch antenna.

Radiation characteristics

The radiation characteristics of the proposed antenna are discussed next. Considering the current distributions at the operational bands (Fig. 5.8), a clear distinction exists between the current distributions at the third and fourth sub-bands (Fig. 5.8c-d) compared to that of the first and second sub-bands (Fig. 5.8a-b). The presence of strong loop currents on the metal cavity are clearly evident at the third and fourth sub-bands. The difference in the maximum amplitude of the current, at the third and fourth bands, is also apparent, as a consequence of this difference in the current distribution. The impact of this difference in the current distribution on the radiation patterns can be observed from Fig. 5.9, which presents the computed radiation patterns (3D-plots) at the operational bands.

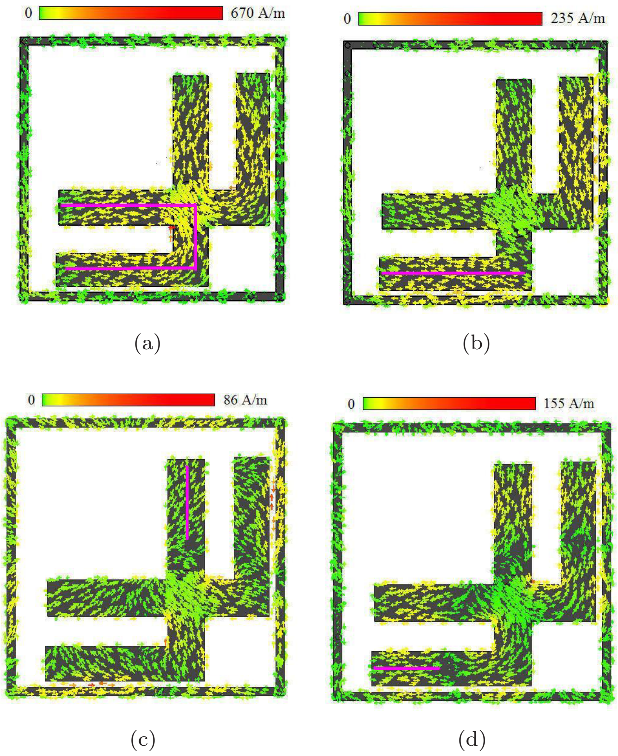

Figure 5.8: Surface current distribution at the operational sub-bands. (a)- 9.7 GHz, (b)- 17.04 GHz, (c)- 25.2 GHz and (d)- 35.1 GHz. Pink marker represents node-to-node spacing.

The presence of strong cavity currents, along with the currents on the radiating patch, result in omni-directional (along the azimuth) radiation patterns at the third and fourth bands. This contrasts with the more patch-like radiation patterns achieved at the first and second operational bands. The demonstrated performance illustrates the antenna's capability to support both patch-like and omni-directional radiation patterns. This hence permits the use of the antenna for communication applications, due to its broad omni-directional patterns at the high bands, and as an array antenna, if required, at the low frequency bands (first and second bands). The antenna is linear diagonally-polarised in all the operational bands. A 'grounded-pin' technique for achieving elliptical polarisation in a target band was also developed and experimentally verified. The details of this technique are presented in Appendix C.

The multi-band characteristic, with the inherent capability to enhance or suppress any desired band(s) of interest (Appendix C), support for both patch-like and omni-directional patterns, and extremely low-profile electrical dimensions, form a unique combination, contributing to the novelty of the proposed design.

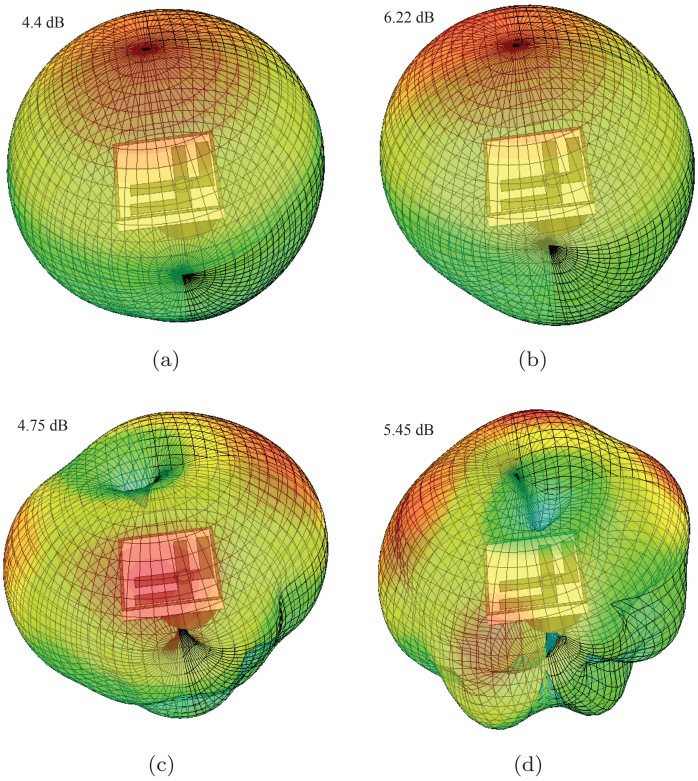

(a) (b)

(c) (d)

Figure 5.9: Computed radiation patterns of the quad-band crossed L-bar patch antenna. (a)- 9.7 GHz, (b)- 17.04 GHz, (c)- 25.2 GHz and (d)- 35.1 GHz. Values marked represent peak directivity.

5.3 Array-capable dual-band antenna optimisation

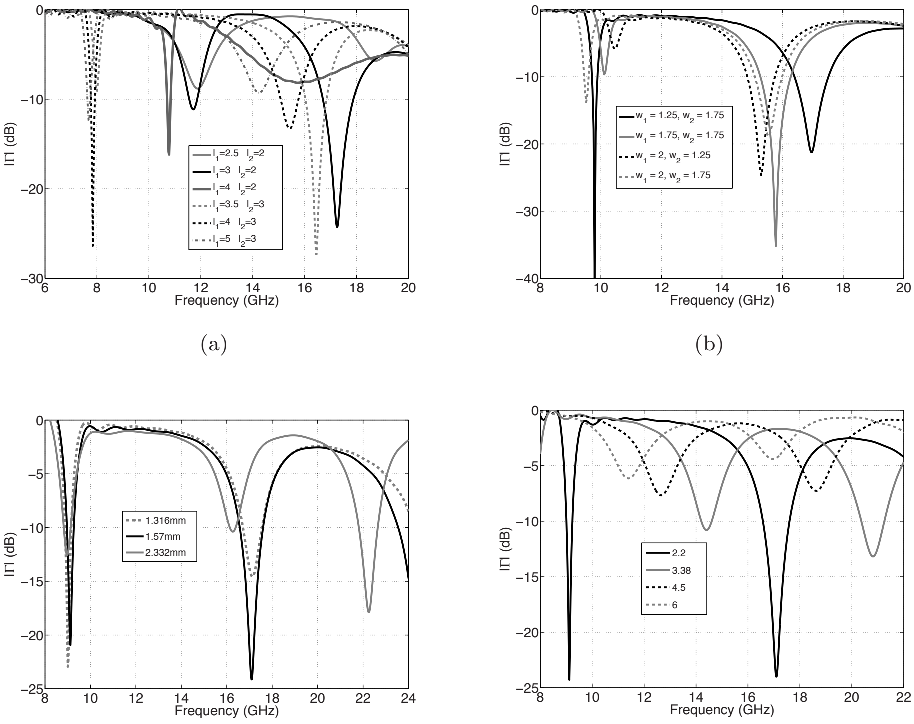

(a) (b)

(c) (d)

Figure 5.10: Optimisation of the dual-band version of the crossed L-bar array antenna. (a)- impact of arm length ratio (l_1/l_2), (b)- impact of arm width ratio (w_1/w_2), (c)- impact of height of plate-through-hole cylinder (h_{PTH}) and (d)- impact of dielectric permittivity (ϵ_r) of substrate.

The use of the crossed L-bar arrangement facilitates in achieving optimal electrical dimensions, as compared to the models with individual L-bars, making it attractive and suitable for the development of dual-band wide scanning phased arrays. The broad patch-like radiation patterns (in the first and second operational bands) are also well suited for array applications. However, the optimisation of the dual-band version of the crossed L-bar antenna, making use of the first and second sub-bands, was still required in order to reduce the unit-cell dimensions.

The quad-band antenna, presented in the previous section, has unit-cell dimensions equal to $0.4\lambda \times 0.4\lambda$ and $0.7\lambda \times 0.7\lambda$ at the first and second bands respectively. When a dual-band variant (making use of the first and second bands) of the crossed L-bar antenna was considered, a closer look at the unit-cell dimensions at the high frequency band (17 GHz) revealed that the maximum scanning angle was limited to only 25 degrees, as per the relation $d_e = \lambda_{op}/1 + sin(\theta_{max})$. Where, λ_{op} refers to the wavelength at the operational band and d_e refers to the inter-element spacing. Hence, the maintenance of smaller unit-cell dimensions with the same frequency ratio and radiation patterns, formed the primary objective for the optimisation carried out. In this regard, the optimisation of the antenna characteristics was mainly influenced by four key metrics viz., the L-bars length ratio (l_1/l_2), L-bars width ratio (w_1/w_2), height of the plate-through-hole cylinder (with a fixed matching ring diameter) and the dielectric permittivity of the substrate (refer Fig. 5.4c for dimensions marking).

The summary of the optimisation can be elucidated as follows. Firstly, the impact of the ratio of the lengths of the stem (l_1) and base (l_2) of the L-bars (l_1/l_2) was considered (Fig. 5.10a). For ratio values less than or equal to 1, the dual-band performance was largely affected. Maintaining base lengths (l_2) less than 2 mm, resulted in the radiating patch becoming electrically small, thereby affecting the dual-band characteristic completely. For the same ratio value (l_1/l_2=1) and larger base lengths ($l_2 \geq 3$), the dual-band characteristic was sustained, albeit with considerable reduction in the frequency ratio. The variation of the length ratio is akin to the variation of the length in patch antennas, which typically results in the shift in the frequency of the operational band(s). The optimum performance was achieved for length ratios (l_1/l_2) greater than 1.5, with the base length (l_2) maintained greater than or equal to 3mm. This condition ensured the sustenance of the dual-band characteristic with the targeted frequency ratio (greater than 1.7:1).

The impact of the widths ratio (w_1/w_2) was analysed next (Fig. 5.10b). Compared to the length ratio, the width ratio does not have a drastic impact on the dual-band performance. The ratio optimisation was largely carried out to achieve the necessary fine-tuning required in terms of the impedance match at the operational bands.

Thirdly, the impact of the variation of the height of the PTH cylinder (h_{PTH}) was examined. The increase in the height of the PTH cylinder, which also implies an increase in the thickness of the substrate, results in the disturbance of the reactance balance. This is clear from the plot (Fig. 5.10c), in which case the increase in the PTH height above 2 mm, resulted in a marked disturbance of the high frequency band, strongly affecting the impedance matching at the same band. For all the values shown, the matching ring diameter (d_r) was maintained constant. It is worth mentioning, that since the height of the PTH cylinder and the substrate thickness are inter-related, the height of the PTH cylinder was varied as per standard substrate thicknesses (t) available for fabrication [76].

Finally, the impact of the permittivity is illustrated through Fig. 5.10d. Use of substrates with higher permittivity was considered to evaluate the possibility of achieving low-profile electrical dimensions. For a fixed value of substrate thickness (t), the increase in the permittivity causes drastic disturbance to the band characteristics of the antenna. This behaviour could be compensated by using larger substrate thicknesses, as per the chosen value of permittivity. This however, was not pursued as the maintenance of thicker substrates with higher permittivity ($\epsilon_r \geq 4.5$), would result in increased levels of mutual coupling in arrays. Having high mutual coupling with small inter-element spacing would in turn be detrimental to the scanning performance of the array. Only standard permittivity values used for fabrication [76] were used in for this optimisation step.

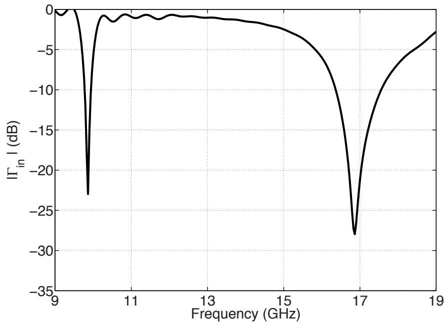

Figure 5.11: Computed input reflection coefficient ($|\Gamma_{in}|$) of the crossed L-bar patch antenna optimised for dual-band operation.

Table 5.1: Optimised dual-band antenna variant dimensions

Dimension	Value (mm)
l_1	8.35
l_2	6.7
w_1	1.35
w_2	1.25
d_r	1.9
U_{cell}	10
t	1.57
ϵ_r	2.2

The dimensions of the dual-band antenna, finalised based on the optimisation procedure, are summarised below in Table 5.1. The unit-cell dimensions ($10mm \times 10mm$) measure $0.55\lambda \times 0.55\lambda$, at the high frequency band, which in turn allows grating-lobe-free scanning range up to a maximum of 60 degrees, at both the operational bands. The computed input reflection coefficient ($|\Gamma_{in}|$) of the crossed L-bar antenna (standalone), optimised for dual-band performance, is shown in Fig. 5.11. The antenna supports a frequency ratio of 1.75:1, with the operational centre frequencies at 9.8 GHz and 17.0 GHz respectively. The bandwidths at the sub-bands are 320 MHz and 1.3 GHz respectively. The corresponding radiation patterns are similar to the ones presented in Fig. 5.9b-c. The embedded radiation patterns (in array) are covered in later sections. The low-profile dimensions of the array antenna, along with the dual-band performance and consistent radiation patterns are well-suited for array operations, the details of which are presented in the next section.

5.4 Infinite array analysis

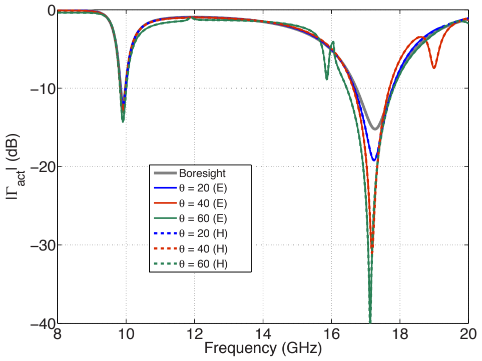

Figure 5.12: Variation of the dual-band antenna's active reflection coefficient ($|\Gamma_{act}|$) with scanning angle in infinite array

Evaluation of the antenna's performance in infinite array, using the frequency domain solver in CST-MWS, was carried out as the first step in the array analysis. The variation of the dual-band characteristics and the sub-band bandwidths with scanning angle, was evaluated in the infinite array. The corresponding performance summary obtained with the infinite array simulation is presented in Fig. 5.12. The cavity architecture of the antenna helps in lowering the mutual coupling, thereby aiding in the maintenance of the dual-band characteristics up to a maximum of 60 degrees along both the principal planes of operation. Another significant feature of the antenna's performance is the maintenance of the bandwidth at both the operational bands over wide scanning angles, with only marginal variations at the high frequency band. This performance ensures the absence of any effects of scan blindness up to a maximum 60 degrees in both planes. The optimised unit-cell dimensions and wide-angle impedance match characteristics of the dual-band antenna are both useful and advantageous for development of array prototypes, the details of which are presented next.

5.5 Finite arrays

The development of finite arrays forms an integral part of the research for the verification of the proposed concepts. In this regard, the crossed L-bar patch antenna was implemented and optimised for performance in both linear and planar arrays using full-wave numerical models. The specific details are summarised in the following subsections.

5.5.1 Linear arrays

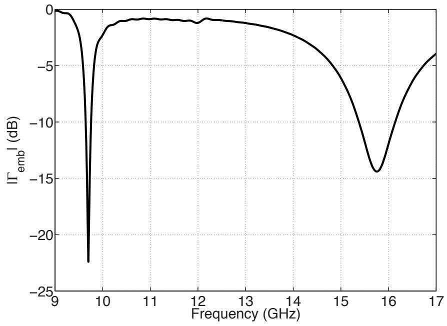

Figure 5.13: Computed embedded reflection coefficient ($|\Gamma_{emb}|$) of the centre element (no: 4) in linear array.

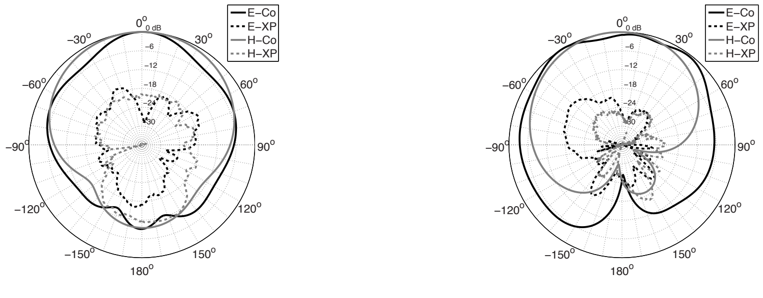

(a)

(b)

Figure 5.14: Computed embedded radiation patterns of the centre element (no: 4) in linear array. (a)- 9.7 GHz and (b)- 15.8 GHz.

Linear array of crossed L-bar patch antennas, with axis of the array oriented along the $\phi = 0^o$ plane of the antenna (refer Fig. 5.4a), was modelled. As the antenna is diagonally-polarised, fabrication of the linear array along the E- or H-plane ($\phi = 135^o$ and $\phi = 45^o$ planes in Fig. 5.4a) was not possible due to reasons related to mechanical stability. The dual-band antenna with unit-cell dimensions of $10mm \times 10mm$, was used in the 7-element linear array modelled in CST-MWS. No major modification of the antenna's L-bars or cavity dimensions was carried out. The simulated embedded reflection coefficient ($|\Gamma_{emb}|$) and radiation patterns, at the operational bands, of the centre element (no: 4) are presented in Figs. 5.13 and 5.14 respectively. The array supports dual-band characteristics with a frequency ratio of nearly 1.7:1. Consistent and broad patterns are achieved at both the operational bands, with the patterns along the $\phi = 0^o$ plane more affected, due to the element loading along this plane.

5.5.2 Planar arrays

The next and final step in the array analysis was the development of planar arrays. Finite arrays of different dimensions (5×5, 7×7 and 9×9) were modelled and the performance difference was evaluated. As was presented in the previous chapter, the final size of the planar array for prototype development was chosen based on the conformance of the array performance with respect to the infinite array. The array size needs to be large enough to capture the difference in performance between the edge and centrally embedded elements, and on the other hand should also emulate the infinite array. The variation of the embedded reflection coefficient ($|\Gamma_{emb}|$) of the centre element of the different planar arrays evaluated is presented in Fig. 5.15. The active reflection coefficient obtained with infinite array simulation is also added for comparison. Based on the results of the analysis, a 49-element planar 7×7 array was chosen for the prototype demonstrator development as it satisfied the above mentioned requirements. Maintenance of larger array size did not result in any significant variation in performance.

The embedded radiation patterns at the operational bands of the centre element (no: 25) in the planar (7×7) array are presented in Fig. 5.16. Consistent radiation patterns with cross polarisation levels less than -15 dB are obtained at both the bands. The bandwidths at the sub-bands are at 280 MHz and 1.2 GHz respectively, with a frequency ratio of nearly 1.8:1.

The effectiveness of the metal cavity to confine the field distribution within the unit-cell, is demonstrated through the field distribution plots over the array, at the operational centre frequencies (Fig. 5.17). Very low levels of coupling, less than -30 dB, are obtained after the second adjacent element from the centre element. This behaviour is especially important given the very small inter-element spacing (0.33λ) at the low frequency band. The maintenance of the dual-band characteristics with scanning, presented in Fig. 5.12, can as well be attributed to the presence of the

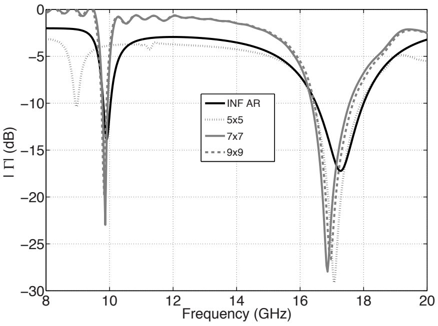

Figure 5.15: Variation of the embedded reflection coefficient ($|\Gamma_{emb}|$) of the centre element planar arrays of different sizes.

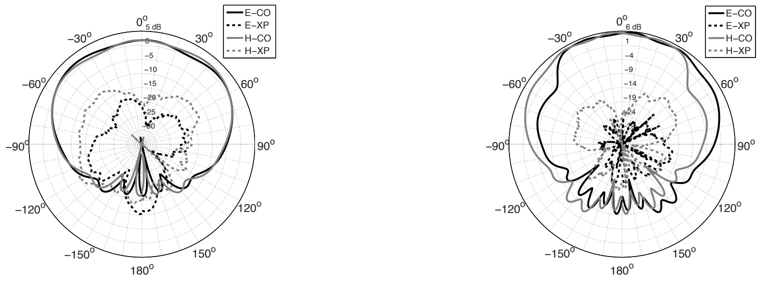

(a)

(b)

Figure 5.16: Computed embedded radiation patterns of the centre element (no: 25) in planar array. (a)- 9.9 GHz and (b)- 17 GHz.

metal cavity.

The unit-cell dimensions ($10mm \times 10mm$) of the array antenna are similar to those of the optimised version, presented in Section 5.3 (Table 5.1). The widths of the bases of the L-bars are however, slightly larger ($w_2 = 1.75mm$) as compared to that of the stand-alone dual-band version ($w_2 = 1.25mm$). This difference in the w_1/w_2 ratio is required for re-optimising the antenna performance in planar array. The broad radiation patterns and small unit-cell dimensions ($0.34\lambda_L \times 0.34\lambda_L$), guarantee wide-angle grating-lobe-free scanning capability, with the low mutual coupling characteristic avoiding scan blindness effects. The beam scanning performance of both the linear and planar dual-band arrays are covered later in the experimental results section.

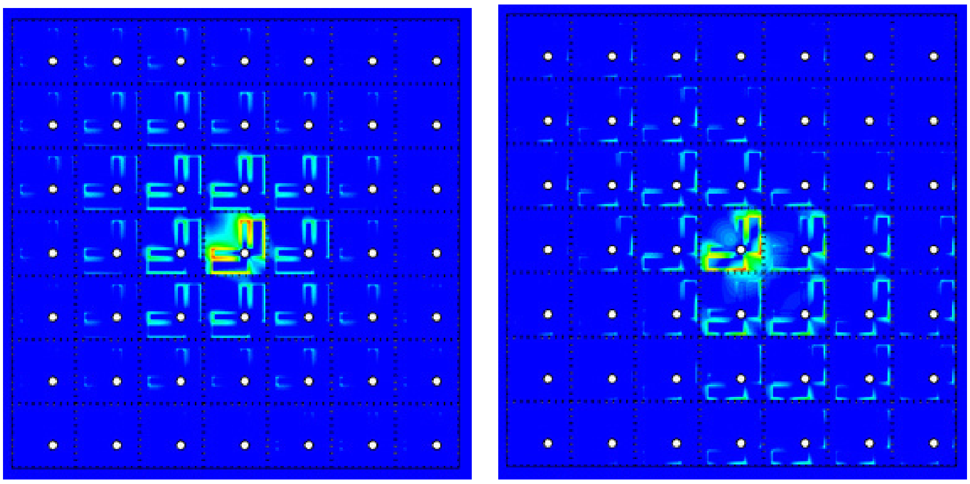
(a) (b)

Figure 5.17: E-field distribution demonstrating low levels of coupling with active centre element (no: 25) in planar (7 × 7) array. (a)- 9.2 GHz and (b)- 16.5 GHz.

5.6 Concept demonstration

5.6.1 Measurement set-up

The experimental measurements of the antenna elements and the linear and planar array prototypes were carried out in the DUCAT anechoic chamber at TU-Delft, optimised for measurements in the 4 - 40 GHz range. Two types of reference horn antennas were used for the radiation pattern measurements, as the operational frequencies of the antenna prototypes cover a wide frequency range from 8 to 36 GHz. The ridged horn antenna, shown in Fig. 5.18a, operational in the 2 - 20 GHz range, was used for the patterns measurements of the dual-band linear and planar arrays with crossed L-bar antennas. The same reference antenna was used for the pattern measurements at the first and second operational bands of the stand-alone quad-band antenna element. For pattern measurements above 20 GHz, which includes the high frequency band of the single L-bar dual band antenna, and the third and fourth operational bands of the quad-band antenna, the dual-polarised horn antenna, shown in Fig. 5.18b, with an operational range of 20 - 40 GHz range, was used as the reference antenna. A step increment of 10 MHz was used for the reflection coefficient and coupling measurements, and a 1 degree step was used for the radiation pattern measurements.

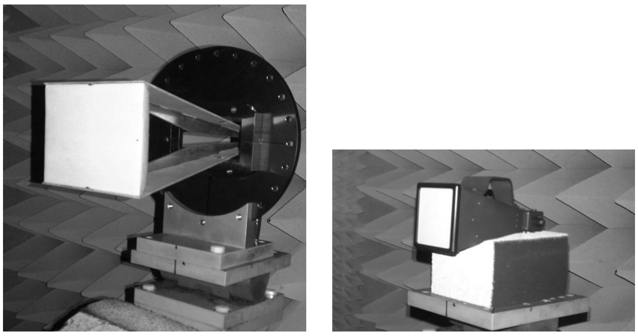

(a) (b)

Figure 5.18: Reference horn antennas used for the measurements. (a)- 2-20 GHz ridged horn antenna and (b)- 20-40 GHz dual-linearly-polarised horn antenna.

5.6.2 Quad-band stand-alone patch antenna

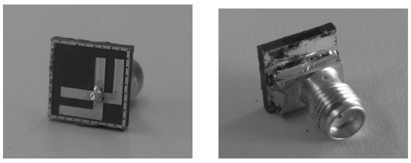

(a) (b)

Figure 5.19: Fabricated quad-band crossed L-bar antenna prototype. (a)- perspective view and (b)- connector.

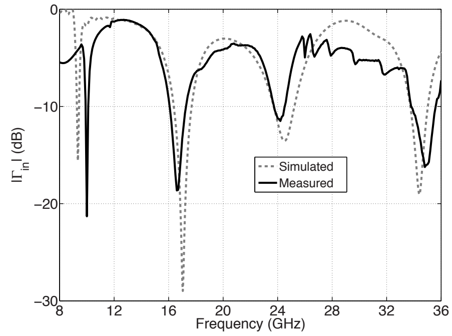

Figure 5.20: Measured and simulated input reflection coefficient ($|\Gamma_{in}|$) of the quad-band antenna.

The fabricated quad-band antenna prototype and the connector assembly are shown in Fig. 5.19. Due to the small unit-cell dimensions of the antenna ($12.5mm \times 12.5mm$), minor mechanical modification (trimming) of the SMA connector's base is required before mounting it on the ground plane. The use of mini-SMA connectors can be a viable alternative option. It can also be noticed that the ground plane of the antenna has the dimensions of the unit-cell similar to that of the simulated model. This ensures a fair comparison between the simulated and measured results.

The measured input reflection coefficient ($|\Gamma_{in}|$), presented in Fig. 5.20, exhibits good conformance with the computed results. The minor shifts in the bands' centre frequencies are due to the use of the adhesive layers in the fabricated model, which have higher permittivity ($\epsilon_r = 3$) as compared to the values used for the modelling of the substrates in the full-wave simulations. Measured bandwidths of 280 MHz, 890 MHz, 900 MHz and 1.1 GHz are achieved at the operational sub-bands

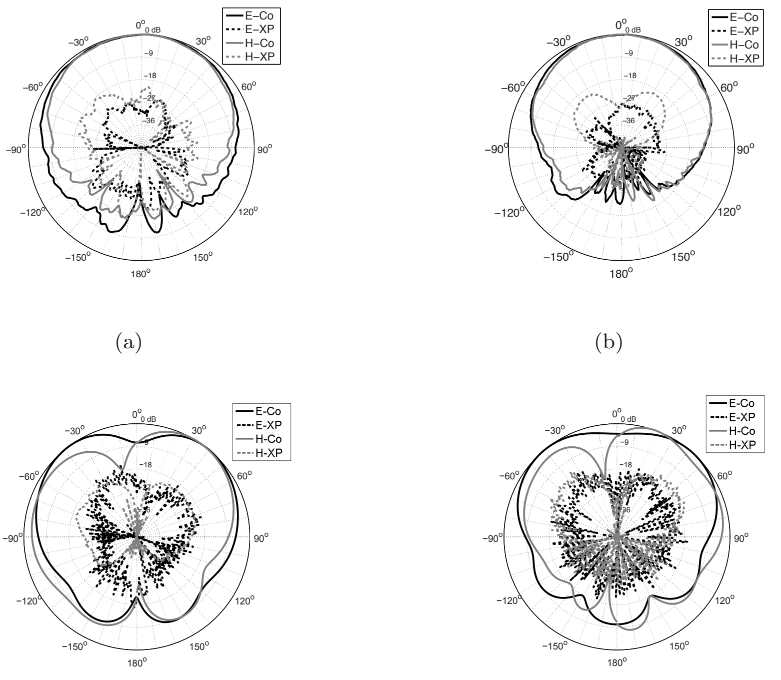

(a)

(b)

(c)

(d)

Figure 5.21: Measured radiation patterns of the quad-band antenna. (a)- 9.9 GHz, (b)- 17.64 GHz, (c)- 25.2 GHz and (d)- 35.1 GHz

Analysis of the radiation patterns of the quad-band, presented in Fig. 5.21, demonstrates the antenna's capability for supporting both patch-like and omni-directional patterns, as described in Section 5.2. The cross-polarisation levels, measured along the principal E- and H-planes, are maintained less than -17 dB over all angular points for the first and second operational bands, and less than -14 dB for the third and fourth operational sub-bands. The proposed quad-band antenna concept's novel performance characteristics have hence been demonstrated.

5.6.3 Linear arrays

The validation of the linear dual-band array is discussed next. The top view and connector assembly of the fabricated 7-element linear array of crossed L-bar patch antennas are shown in Fig. 5.22. Compared to the unit-cell of the quad-band antenna, the unit-cell of the dual-band variant, used in the arrays, have even smaller dimensions of $10mm \times 10mm$. Due to the size constraints, conductive adhesive was used for mounting the (trimmed) connectors on the array's ground plane, as a solder-based approach proved to be very complicated.

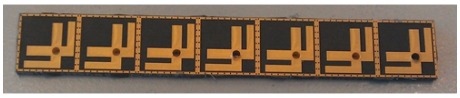

(a)

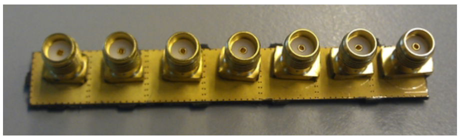

(b)

Figure 5.22: Fabricated 7-element linear array prototype. (a)- top view and (b)- connector arrangement.

The simulated and measured embedded reflection coefficient ($|\Gamma_{emb}|$) of the centre (no: 4) element of the linear array are shown in Fig. 5.23. The dual-band operation in the X/Ku-bands is well maintained with a maximum frequency ratio of 1.7:1 between the operational bands. The measured sub-band bandwidths are 300 MHz and 1.1 GHz respectively.

Embedded radiation patterns were measured along three principal $\phi-$planes of interest viz., the $\phi = 0^o$ (axis of the array), $\phi = 45^o$ (H-plane) and $\phi = 135^o$ (E-plane). The measured embedded radiation patterns of the centre element (no: 4) of the linear array are presented in Fig. 5.24. Broad radiation patterns are exhibited in all the three planes, at both the operational bands. The patterns along the $\phi = 0^o$

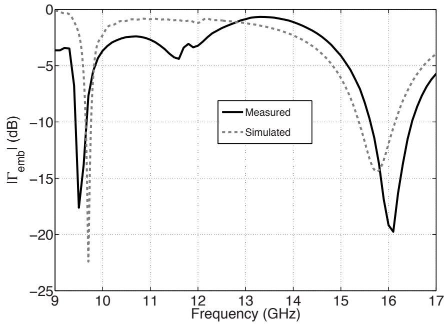

Figure 5.23: Comparative plot of the measured and simulated embedded reflection coefficient ($|\Gamma_{emb}|$) of the centre element (no:4) in linear array.

plane however, are slightly more directive at the high frequency band, compared to the E- and H-plane patterns, due to the element loading along this plane. In this sense, it can also be inferred that, as expected, the embedded patterns along the E- and H-planes are less perturbed in the linear array.

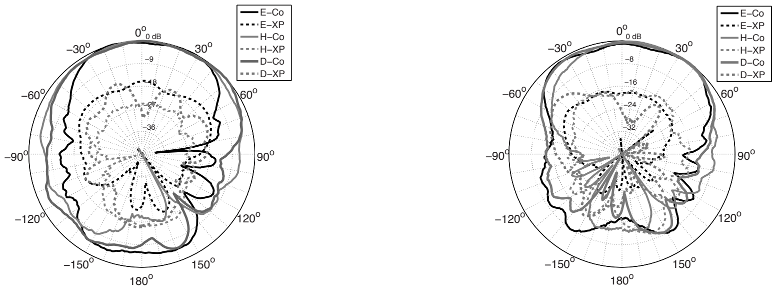

(a) (b)

Figure 5.24: Measured embedded radiation patterns of the centre element (no: 4) of the linear array. (a)- 9.8 GHz and (b)- 16.4 GHz.

The measured scanning performance of the linear array, based on the embedded element radiation patterns, at both the operational bands, are presented in Fig. 5.25. The scanning performance is evaluated along the $\phi = 0^o$ plane, which corresponds to the axis of the linear array. Due to the small physical and electrical dimensions of the array, the array patterns exhibit broad patterns at all scanning angles. The large frequency ratio supported (1.7:1), which results in larger electrical length of the array at the high frequency band, is the main reason for the comparatively more directive scan patterns achieved at the high frequency band (Fig. 5.25b). It is hence demonstrated that with linear array of the proposed dual-band crossed L-bar patch antennas, scanning up to a maximum of 60 degrees and 50 degrees, can be achieved at the low and high frequency bands respectively.

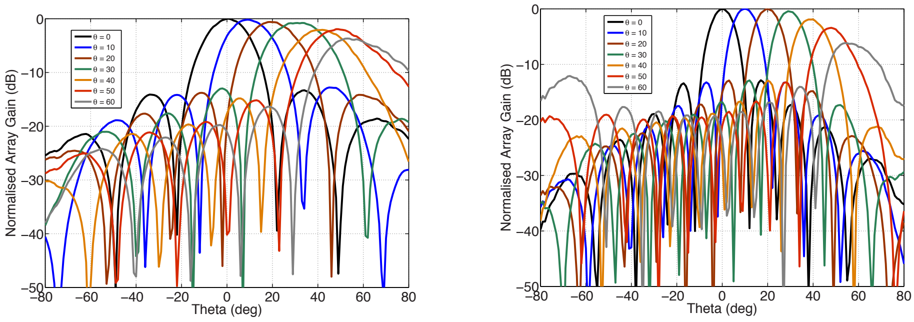

(a)

(b)

Figure 5.25: Measured beam scanning performance of the linear array. (a)- 9.8 GHz and (b)- 16.4 GHz.

5.6.4 Planar array

The fabricated 49-element planar (7 × 7) array, along with its connector assembly, are presented in Figs. 5.26a-b. The array measures $70mm \times 70mm$. The thickness of the array face, which measures only 1.58 mm ($0.05\lambda_L$), adds to the low-profile dimensions of the array. As in the case of the linear array, conducting adhesive was used for mounting the SMA connectors for the individual array elements on the ground plane, due to the small unit-cell dimensions ($10mm \times 10mm$).

In order to evaluate the active reflection coefficient of the centre element of the planar array, the embedded reflection coefficient ($|\Gamma_{emb}|$) and mutual coupling characteristics were measured. A 1×24 port switch was used for the mutual coupling measurements between the element under consideration (centre element) and the other array elements. Following this, the active reflection coefficient ($|\Gamma_{act}|$) was calculated based on the measured embedded reflection coefficient and mutual coupling.

The plots presenting the measured active reflection coefficient ($|\Gamma_{act}|$) of the centre element (no: 25) and the mutual coupling characteristics along the $\phi = 45^o$ (H-) and $\phi = 135^o$ (E-) planes (refer Fig. 5.26a) are shown in Fig. 5.27. Low levels of mutual coupling (below -17.5 dB) are maintained along both the principal planes considered, demonstrating the effectiveness of the cavity backed architecture. The maintenance of the low levels of coupling even with very small inter-element spacing ($0.33\lambda_L$) is a key feature of the proposed dual-band array design.

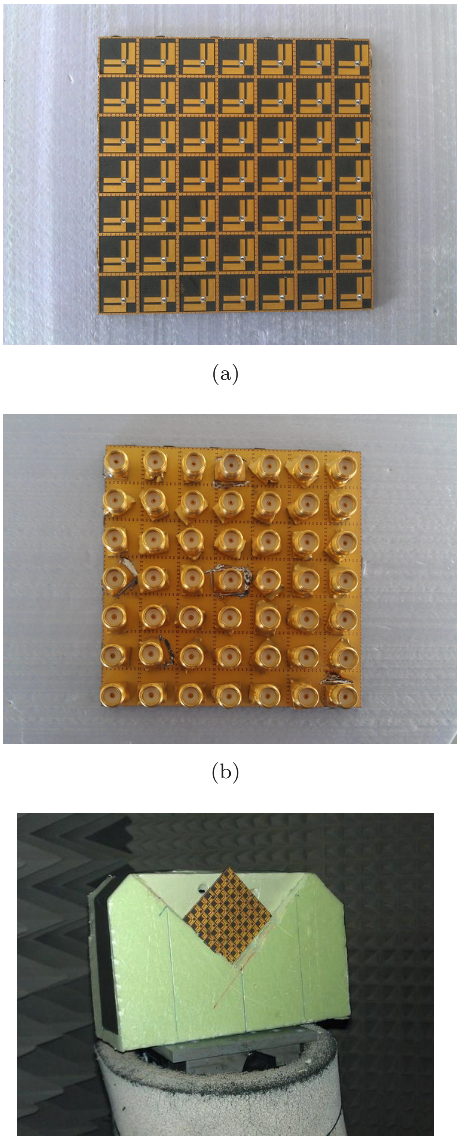

(a)

(b)

(c)

Figure 5.26: (a)- Fabricated planar (7×7) array prototype, (b)- connector assembly and (c)- antenna-under-test (AUT) in anechoic chamber.

The conformance between the measured and computed embedded reflection coefficient (Γ_{emb}) of the centre-element (no: 25) of the planar array is illustrated through Fig. 5.28. The inclusion of the fabrication related constraints and tolerances on the antenna and array design (like substrate values, patch dimensions, cavity via diameters), as presented in Section 5.3, has positively aided in achieving this performance conformance. Measured bandwidths of 270 MHz and 1.2 GHz are achieved at the low and high frequency bands, supporting a maximum frequency ratio of nearly 1.8:1.

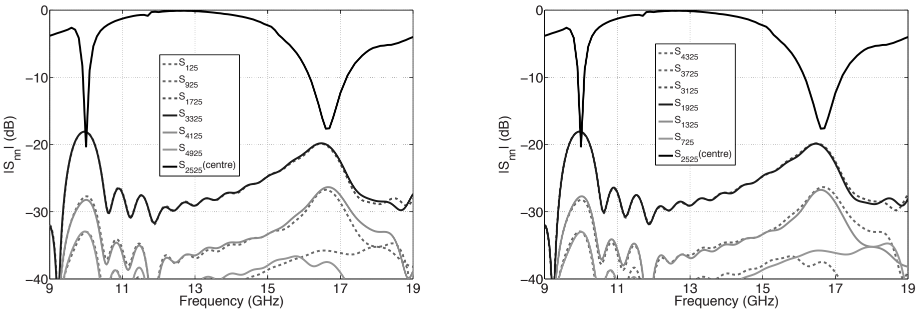

(a) (b)

Figure 5.27: Measured active reflection coefficient ($|\Gamma_{act}|$) and mutual coupling characteristics of the centre element (no: 25) of the planar (7 × 7) array. (a)- E-plane and (b)- H-plane.

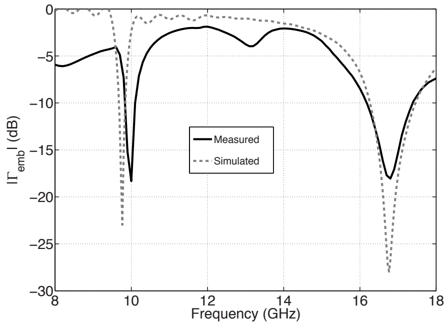

Figure 5.28: Measured and simulated embedded reflection coefficient ($|\Gamma_{in}|$) of the centre element (no: 25) in planar array.

The diagonal polarisation of the proposed crossed L-bar antenna necessitates the use of a custom-made array support for the radiation pattern measurements. The foam block used for supporting the array-under-test (AUT) in the anechoic chamber measurements is shown in Fig. 5.26c. The design of this foam block makes it possible to orient the polarisation of the antenna along different $\phi-$planes for the pattern measurements. Embedded radiation pattern measurements along the $\phi = 45^o$(H-) and $\phi = 135^o$(E-) planes were carried out (refer Fig. 5.26a for $\phi-$plane marking). The measured embedded radiation patterns of the centre element (no:25) of the planar array are presented in Fig. 5.29, to illustrate the broad radiation patterns supported by the array antenna at both the operational bands. The patterns along both the principal $\phi-$planes are also consistent, with minor variations. Furthermore, the cross-polarisation levels are maintained less than -16 dB, over the entire angular range, at both the operational bands. These broad radiation patterns are key to achieving wide-angle scanning, presented next. Additional information on the variation of the embedded radiation patterns and reflection coefficient ($|\Gamma_{emb}|$) between edge and centrally embedded array elements of the planar array are summarised in Appendix C.

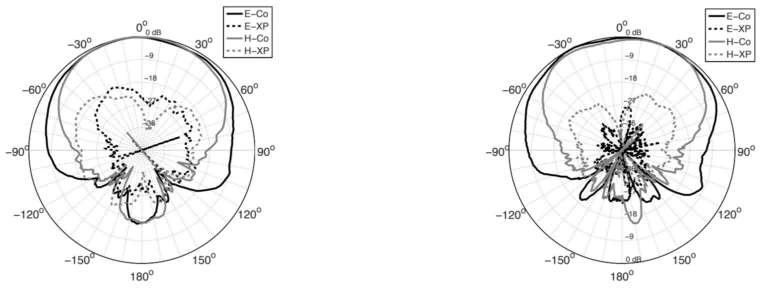

(a)

(b)

Figure 5.29: Measured embedded radiation patterns of the centre element (no: 25) of the planar array.(a)- 9.9 GHz and (b)- 17.1 GHz.

The measured scanning performances of the uniformly excited planar (7×7) array, at the operational bands, are presented in Figs. 5.30-5.31. The embedded radiation patterns were used for evaluating the scanning behaviour along the $\phi = 45^o$ and $\phi = 135^o$ planes. Beam scanning up to a maximum of 60 degrees and 50 degrees are achieved at the low and high frequency bands respectively. The electrically small dimensions of the planar array, at the low frequency band, results in broad scanning patterns, which exhibit comparatively more directive behaviour at the high frequency band. In both the cases, the sidelobe levels are also maintained less than -14 dB for all scanning angles. It is worth mentioning that the sidelobe levels can be reduced further with the application of appropriate amplitude tapering, if required. The combination of electrically small unit-cell dimensions, at both the operational bands, and broad embedded radiation patterns facilitates in achieving this wide-angle scanning capability.

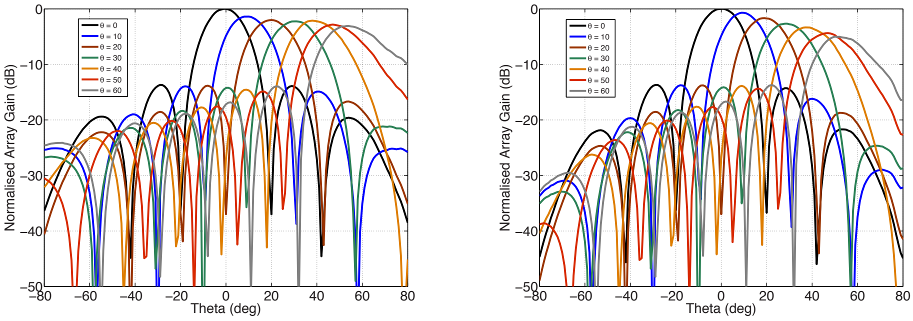

(a) (b)

Figure 5.30: Measured beam scanning performance of the planar array at 9.9 GHz.(a)- E-plane and (b)- H-plane.

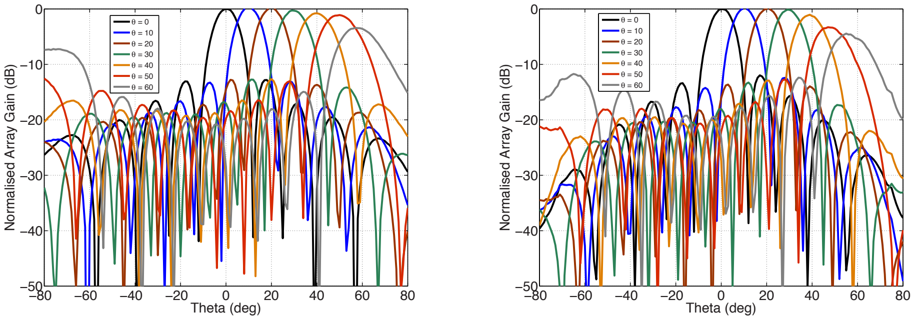

(a) (b)

Figure 5.31: Measured beam scanning performance of the planar array at 17.1 GHz.(a)- E-plane and (b)- H-plane.

In summary , the demonstrated novelties of the proposed dual-band array design include 1) the maintenance of large frequency ratio between operational bands, 2) low levels of coupling, 3) broad embedded radiation patterns, 4) wide-angle beam scanning and 5) extremely low-profile electrical dimensions of array antennas. These aspects represent a strong value addition to the domain of dual-band phased arrays. The proposed dual-band array design can also be very useful for focal-plane arrays, due to its well-separated operational bands and extremely low-profile electrical dimensions.

5.7 Summary

The design of a novel crossed L-bar patch antenna, capable of supporting quad-band operation over a wide frequency range, is proposed in this chapter. The inherent features include the ability to enhance or suppress any desired band(s) of interest, support for both patch-like and omnidirectional patterns, possibility for supporting elliptical polarisation at any target band of interest, and achieving low-profile electrical dimensions suitable for array operations. The simple single-layer geometry is an added feature of this antenna. The small physical dimensions of the quad-band antenna, which measures only $12.5mm \times 12.5mm$, is also suitable for integration in mobile user terminals, predominantly used for SatComm applications.

The proposed *diagonally-polarised* antenna has been optimised in arrays for dual-band operation, making use of the first two operational bands, which support patch-like radiation patterns. Infinite array simulations have been carried out with numerical full-wave solver to optimise the dual-band performance over wide scanning angles. The antenna exhibits extremely attractive impedance characteristics maintaining the dual-band performance, with negligible variation, up to a maximum of 60 degrees when scanned along both the principal E- and H-planes. The performance is noteworthy, given the large frequency ratio (1.8:1) between the bands, and the absence of any external components to stabilise the scanning characteristics.

Following this, 7-element linear and 49-element planar (7×7) arrays, operational in the X/Ku-bands, were modelled and optimised for the development of experimental array prototypes for concept demonstration. The fabricated array prototypes have extremely low-profile dimensions in terms of both the unit-cell and thickness of the antenna element, which measure only $0.33\lambda \times 0.33\lambda$ and 0.05λ respectively, at the low frequency band of operation.

Anechoic chamber measurements were carried out for the stand-alone quad-band antenna, and linear and planar arrays with the dual-band operational variants. Consistent conformance was demonstrated between the computed and measured results in all the cases. Furthermore, wide-angle scanning up to a maximum of 60 degrees, along the principal operational planes (E/H), have been demonstrated with the experimental results for both the linear and planar arrays. The scanning performance achieved at both the bands, even with a large frequency ratio (1.8:1), is significant and a step ahead of the current state-of-the-art in patch-based phased arrays.

A variant of the crossed L-bar patch antenna, employing only one of the L-bars, named the 'single L-bar' patch antenna, has also been optimised for performance in linear and planar arrays, similar to the crossed L-bar antenna. This variant, which functions as a dual-band antenna, supports vertical polarisation as compared to the diagonal polarisation of the original version. The planar array, in this case, has operational bands in the K-band, and supports scanning up to a maximum of 50 degrees and 20 degrees at the low and high frequency bands respectively. This variant supports a maximum frequency ratio of 1.5:1.

In summary, the novel crossed L-bar patch antenna concept introduced in this chapter enables 1) quad-band operation, 2) enhancement or suppression of any desired resonances 3) extremely low-profile dimensions, 4) support for both patch-like and omni-directional patterns, 5) large frequency ratios and 6) wide-angle impedance matching and beam scanning capability. The impedance and radiation pattern characteristics of the crossed L-bar patch antenna are attractive and suitable for both communications and array applications. The demonstrated concept verifications represent a strong value addition to the domain of multi-band antenna and array research.

Chapter 6

Conclusions

6.1 Summary

Antenna array front-ends with both frequency and wide-angle beamforming agility will greatly enhance the reconfigurable capabilities of future multifunction radar systems. Currently, the use of either single-band arrays, with multiple apertures for different radar functions, or ultra-wideband arrays are seen as the two main solutions for multifunction radars. System demands however, can be better satisfied with the use of dual-band arrays due to two main reasons. Firstly, the number of single-band array front-ends used for different target functions can be reduced with the use of dual-band array front-ends. Secondly, compared to the use of ultra-wideband arrays, dual/multi-band phased arrays can facilitate by providing additional filtering at the antenna element level, reduce interferences from out-of-band signals and also ease efficiency requirements on the T/R modules. These advantages served as key motivating factors for the doctoral research, which broadly focused on the development of dual-band single-aperture phased arrays supporting large frequency ratios and wide-angle beamforming. The ability to support well-separated sub-bands, makes it possible to use the same aperture to support different operational tasks, which mostly require different operational frequencies as well. Further, the addition of wide-angle beamforming is extremely useful for applications involving digital beamforming (DBF), a pivotal aspect of modern radars. Finally, patch antenna elements were considered for the research owing to their attractive conformal, cheap and planar architectures, suitable for many practical applications of interest envisaged within the STARS project [8].

The major research tasks included, 1) the investigation of the scanning characteristics of dual-band arrays, 2) mutual coupling reduction in patch antenna arrays, 3) design of novel dual-/multi-band array elements and 4) development of experimental prototype demonstrators of phased array concepts with wide-angle scanning capability and large frequency ratio ($FR \geq 1.5:1$) between sub-bands. Associated supplementary research on the influence of mutual coupling on scanning performance, grid impact on coupling and scanning, truncation impact on impedance of array elements and development of multi-band antennas for SatComm applications have also been successfully carried out.

The major research outputs can be broadly summarised as follows. Based on the investigation of the impact of coupling on scanning performance of dual-band arrays, a novel and simple technique for reducing mutual coupling between closely-spaced array elements has been proposed and validated experimentally. Secondly, linear and planar dual-band phased arrays with wide-angle scanning capability have been developed in L/S, X, X/Ku and K-bands, following which, prototypes in X-, Ku- and K-bands have been built and experimentally verified demonstrating the feasibility of the design concepts proposed and incorporated in the antennas arrays. Finally, the design concepts have been successfully applied for the development of multi-band patch antennas for SatComm applications. Prototype models of the same have been fabricated and their performance verified as well.

The outputs have, for the first time, demonstrated the potential and feasibility of dual-band phased arrays with wide-angle scanning capability for application in future multifunction radar front-ends. The major results achieved, covering aspects of both fundamental research and practical relevance, presented through the chapters of the thesis, to the antenna and radar community, signify an important evolutionary step forward in the development of reconfigurable dual-band phased arrays for future multifunction radars.

6.2 Research contributions and novelty

The major results of the thesis and their associated novelty are summarised in this section.

1. *Dielectric-contrast technique* - A novel technique based on the use of multilayer substrates with dielectric-contrast, in terms of permittivity between the constituent substrate layers, to reduce mutual coupling between adjacent patch antennas in array was developed and its effectiveness experimentally verified. The proposed technique reduces the average power flow between adjacent patches thereby reducing the coupling. The impact of the dielectric contrast ratio ($\epsilon_{r2}/\epsilon_{r1}$), and the need to co-optimise the position of the high permittivity layer (in the multilayer architecture) and the inter-element spacing d_e has been elucidated in detail. In addition to this, the impact of the thickness of the high

permittivity layer on the operational bandwidth was also illustrated. Furthermore, evaluation and illustration of the modification of the characteristics of the operational mode, with the use of modal analysis has also been carried out.The modal analysis, based on the concept of propagators, reiterate the performance difference expected from the use of the multilayer substrate architecture. The variation of the propagation characteristics of the operational mode, along the lateral direction, is illustrated using the lateral wavenumber (k_t). The dependence of the mutual coupling on the inter-element spacing, is also clear from the modal characteristics graphs. A significant feature of the proposed technique is that it does not increase the inter-element spacing by introducing external structures, leaving the scanning performance of the array unaffected. In addition to this, the technique does not affect the array elements' radiation characteristics or its bandwidth. The effectiveness of the technique was demonstrated in arrays with patch antennas, maintaining very small inter-element spacing(0.37-0.38λ). Coupling reduction in the orders of 4.5-5.5 dB were obtained in arrays. The efficacy of the proposed technique (Chapter 3) to reduce coupling levels without any increase in inter-element spacing and fabrication complexity strongly contributes to the novelty of the proposed technique.

2. *Quasi-magneto-electric array antennas* - Dual-band antenna design with quasi-magneto-electric radiation characteristics has been presented. The antenna's novelty stems from the fact that the complementary element is placed in the same plane as that of the radiating element, whereby the slot-based magnetic radiation and the patch-based electric radiation characteristics are simultaneously made use of in the overall radiation mechanism. Furthermore, the antenna is 'array-capable', which in itself adds a strong performance characteristic compared to that of other dual- or multi-band radiators, available in literature, which are mostly non-functional in arrays. Proof-of-concept demonstrations of the antenna as stand-alone and in arrays have been successfully carried out.

3. *Bandwidth enhancement technique for dual-band array elements* - A novel two-step methodology or technique for optimising the frequency ratio and sub-band bandwidths of the dual-band patch antenna was proposed. The first step involves the optimisation of the frequency ratio, achieved by tuning the dimensions of the comb-slot geometry. The second step focuses on achieving the required impedance matching and sub-band bandwidths. This involves the use of the proposed *'lamppost'* feeding architecture, which consists of an inductive feed pin to a capacitive stripline transition. The reactance balance offered by the transition architecture and matching-ring arrangement helps in achieving good bandwidths in the sub-bands. The relative optimisation of the slot geometry and the dimensions of the matching-ring and stripline are pivotal for achieving the expected

frequency ratio and bandwidth. This configuration apart from providing band control flexibility, also offers a new way of feeding dual-band slot-loaded elements as compared to the usual pin or slot based excitations. Furthermore, the *'lamppost'* architecture is also pivotal for achieving the quasi-magneto-electric radiation. The proposed two-step methodology has been applied in the design of dual-band phased arrays and its performance experimentally verified, reiterating the effectiveness and novelty of the technique.

4. *Dual-band phased arrays in L/S and X-bands* - Two novel dual-band phased arrays supporting a frequency ratio of nearly 1.5:1, with wide-angle scanning and good sub-band bandwidths, have been designed and experimentally validated (X-band version). Both the dual-band array antenna variants viz., the comb-slot loaded patch and symmetric comb-slot patch, used in the dual-band arrays designs, have simple single-layer and low-profile architectures suitable for wide-angle scanning arrays. The performance characteristics of the dual-band arrays are a step ahead of the current state-of-the-art in dual/multi-band phased array research in terms of dual-band operation with large frequency ratio, sub-band bandwidths and wide-angle scanning capability.

5. *Multi-band radar and Satcomm antenna* - A novel multi-band crossed L-bar antenna has been developed for operation as both a communications (stand-alone) and radar (in arrays) antenna. The antenna's novel characteristics include support for a maximum of four well-separated operational bands (quad-band), support for both omni-directional and patch-like radiation patterns, flexible resonance characteristics, through which any operational resonance can be enhanced or suppressed as per requirements, extremely low-profile electric and physical dimensions and simple single architecture. The antenna exhibits performance characteristics attractive for application in fixed and mobile SatComm user terminals and the experimental validation of the stand-alone quad-band antenna's performance has also been carried out. The array implementation of the dual-band version of this antenna is described next.

6. *Dual-band phased array demonstrators in X/Ku and K-bands* - A second set of dual-band prototype demonstrator arrays, aimed at improving the frequency ratio, have been designed, fabricated and their performance verified. The X/Ku-band version, which consists of the dual-band version of the crossed-L bar patch antenna (mentioned previously), has wide-angle scanning capability ($\pm 60^\circ$) with a frequency ratio of nearly 1.82:1 between the sub-bands. On the other hand, the K-band version, with the single L-bar patch antenna, supports scanning up to $\pm 50^\circ$ and $\pm 30^\circ$ respectively at the low and high frequency sub-bands of operation, with a frequency ratio of nearly 1.65:1. It is worth mentioning that

both these versions have larger frequency ratios, as compared to the aforementioned L/S and X-band demonstrators. The results are significant considering the large frequency ratios (1.6:1 to 1.82:1), simple single-layer antenna architectures, wide-angle scanning at both bands and good sub-band bandwidths. The successful development of the dual-band arrays (L/S, X-, X/Ku and K-band versions) have hence demonstrated, for the first time, that dual-band phased array can be considered as practical and useful candidates for future multifunction radar front-ends.

In summary, the antenna concepts proposed in this thesis provides avenues for the development of array-capable planar dual-band antennas. Improvement of the frequency ratio between the bands keeping intact the operational bands is essential for the implementation of these antennas in radar systems covering two or more bands. Furthermore, the proposed dielectric technique is attractive and suitable for applications in arrays, which in turn can address the mutual coupling issues, which are non-trivial. However, its worth mentioning, that despite the experimental demonstration of the concepts proposed, further development and integration of these arrays with RF electronics are still required for the development of fully operational dual-band array front-ends. In this regard, some recommendations for future research in this domain, which may serve as continuation of the work presented, are prescribed in the following sub-section.

6.3 Recommendations for future work

- The dielectric-contrast technique, in its current form, is limited to coupling reduction in arrays with single-band patch antennas. The extension of the technique for mutual coupling reduction between wideband (or ultra-wideband) patch antennas in arrays would serve well as a next step. The extended studies might shed light on the full scope and limitations of this technique. Also, the impact of the use of the multilayer substrate on the bandwidth of wideband elements is another related research topic of interest.

- The trade-off between the maximum achievable frequency ratio and the sub-band bandwidth has been presented (Chapter 4). Techniques to increase the frequency ratio without drastically affecting the sub-band bandwidth can be explored and is very attractive and useful for practical applications as well.

- Dual-band phased arrays have been developed in different radar bands. The case of switch-able polarisation was however not been considered in the current work. The inclusion of the switch-able polarisation characteristic in the array element can add further weight by extending these concepts to applications requiring the use of dual-linear or circular polarisation, for example, weather radars.

- The proposed bandwidth enhancement technique (in Chapter 4) can be applied to similar (and suitable) slot-loaded patch antennas, whereby on one hand the limits of its application can be validated and on the other hand, if proven successful, can improve the bandwidth performance of the respective dual/multi-band antenna element(s).
- The design and development of dual-band phased arrays forms a part of the overall system design. Several associated research issues including the development of dual-band T/R modules, integration of the T/R modules with array elements, performance optimization and testing and the calibration of sub-systems provide enough open topics for future research in the design and development of dual/multi-band array based sub-systems for multifunction radars.

6.4 Impact of the research

The work presented in this dissertation resulted in 5 journals (*IEEE-TAP* and *IET-MAP*) and 13 proceedings in all major conferences (*AP-S, EuMC, EuRAD, AMTA* and *EuCAP*), as well as in the development of one of the first demonstrations of dual-band wide-scan phased arrays.

The results are a step ahead of the current state-of-the-art and henceforth serve as a vanguard for the development of practical and agile dual-band phased arrays for future multifunction radar system front-ends.

Appendix A

Analysis of Embedded Element Performance Variation Over the Array Aperture

A.1 Cavity impact in infinite array

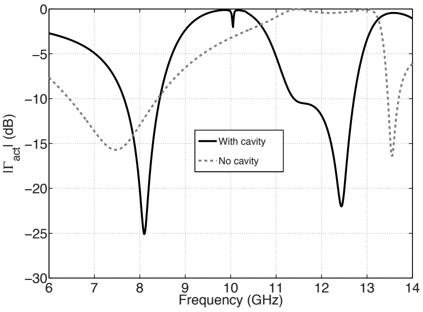

Figure A.1: Impact of cavity on the impedance performance in infinite array.

The importance of the cavity-backing for supporting well-defined dual-band operation, is illustrated through the comparative graph (Fig. A.1) presenting the boresight active reflection coefficient ($|\Gamma_{act}|$) in infinite array. The dual-band characteristic is completely disturbed in terms of band placements without the inclusion of the cavity. This also impacts the antenna's ability to maintain consistent impedance matching over wide scanning angles, pivotal for array applications.

A.2 Linear arrays

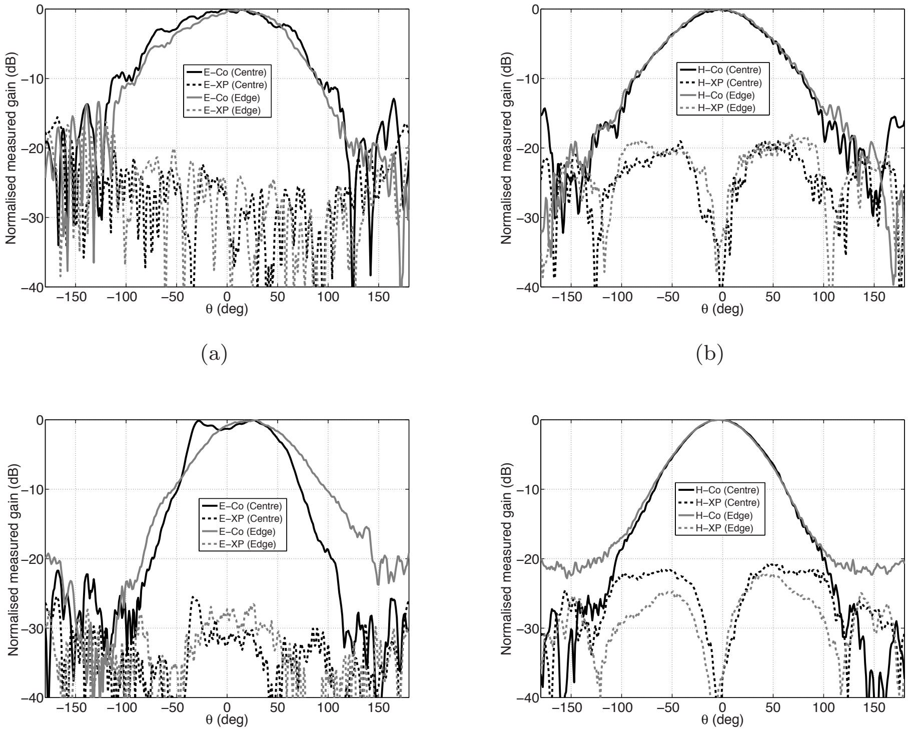

(a) (b)

(c) (d)

Figure A.2: Variation of the measured embedded radiation patterns of the centre (no: 7) and edge (no: 1) elements in linear E-plane array. (a)- E-plane at 8.5 GHz, (b)- H-plane at 8.5 GHz, (c)- E-plane at 11.0 GHz and (d)- H-plane at 11.0 GHz.

A summary of the variation of the measured radiation patterns between the edge and centre elements in both the E- and H-plane linear arrays is presented in this subsection. The low levels of mutual coupling existent in both the linear arrays, ensure good conformance between the patterns of the edge and centre elements, at both the operational bands (Fig. A.2-A.3). The absence of element loading along the H- and E-planes, in the E- and H-plane linear arrays, are responsible for the broad patterns achieved along the H- (Fig. A.2b and A.2d) and E-planes (Fig. A.3a and

A.3c). The pattern conformance in both the linear arrays are noteworthy, given the small electrical lengths of the linear arrays ($5.7\lambda_L$).

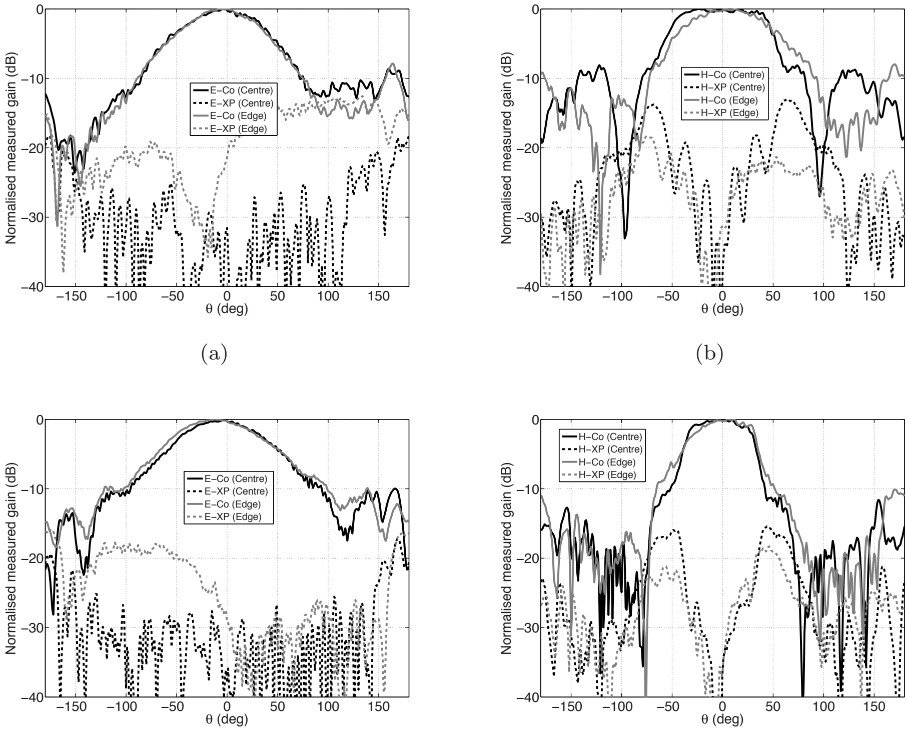

(a)

(b)

(c)

(d)

Figure A.3: Variation of the measured embedded radiation patterns of the centre (no: 7) and edge (no: 1) elements in linear H-plane array. (a)- E-plane at 8.5 GHz, (b)- H-plane at 8.5 GHz, (c)- E-plane at 11.0 GHz and (d)- H-plane at 11.0 GHz.

A.3 Planar array

The measured embedded reflection coefficients of elements at different positions in the planar array are presented in Fig. A.4. Two significant characteristics are worth mentioning. Firstly, the dual-band impedance matching performances are consistently achieved for array elements distributed at different position in the array. Secondly, the bandwidths at the operational bands are also maintained in all cases with minor variations. These characteristics, along with the demonstrated low levels of mutual coupling (Section 4.5.3), strongly emphasise the array's suitability for supporting wide-angle scanning, avoiding scan blindness problems.

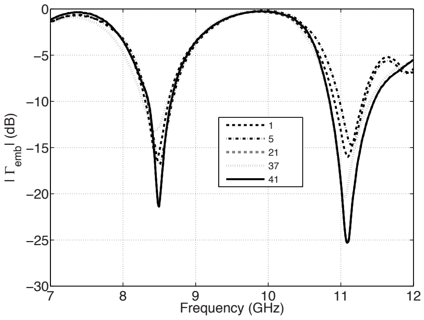

Figure A.4: Variation of the measured embedded reflection coefficient ($|\Gamma_{emb}|$) of different array elements of the planar array.

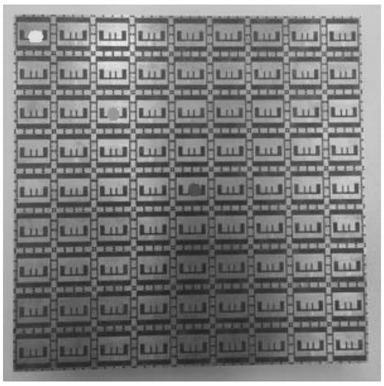

Figure A.5: Elements considered for the comparative analysis on the variation of the radiation patterns. Red - centre (no: 41), green - middle (no: 21) and yellow - edge (no: 1).

The variation of the radiation patterns between the edge and centrally embedded elements are summarised next (refer Fig. A.5 for the elements considered in the comparative analysis). Yet again, despite the relatively small electrical dimensions of the planar array, high degree of conformance is exhibited along both the principal planes, at the operational bands. The maintenance of consistent embedded patterns in array elements is a major characteristic which aids in achieving the wide-angle scanning performance (presented in Section 4.5.3).

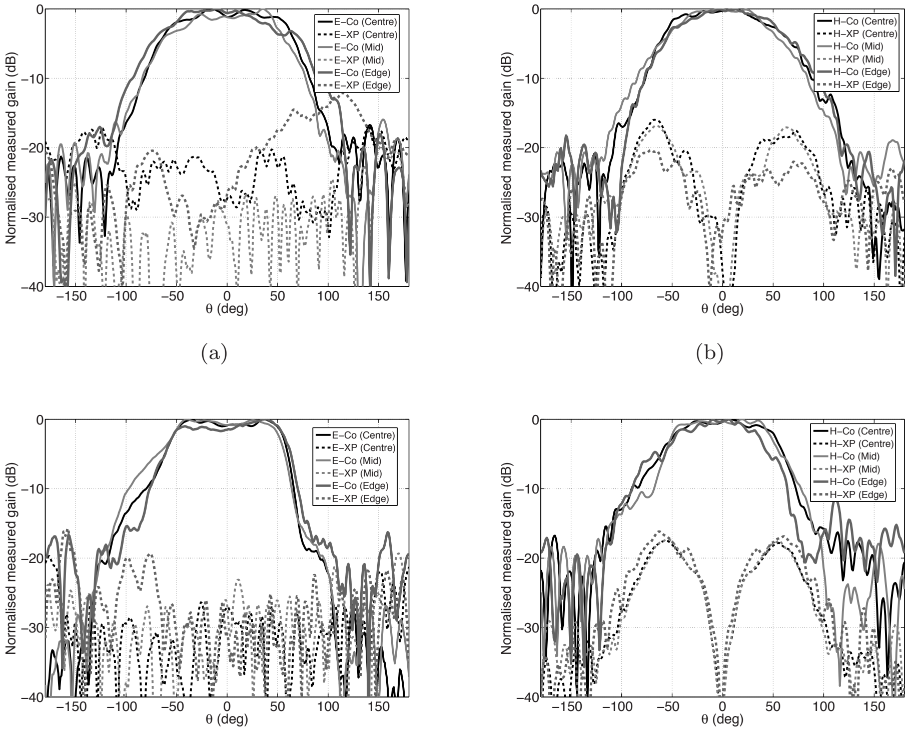

(a) (b)

(c) (d)

Figure A.6: Variation of the measured embedded radiation patterns of the centre (no: 41), middle (no: 21) and edge (no: 1) elements in the planar (9×9) array. (a)- E-plane at 8.3 GHz, (b)- H-plane at 8.3 GHz, (c)- E-plane at 11.0 GHz and (d)- H-plane at 11.0 GHz.

A.4 Experimental set-up for coupling measurements

Table A.1: Technical specifications of the coupling measurement set-up

Network analyser	Agilent PNA E8364B
Port switch	Agilent 87050A-K24 Multi-port Test-Set
Ports available	24
Frequency sweep	7 - 14 GHz (7001 points)
Array details	Dual-band 81-element, planar (9×9) X-band array

Figure A.7: Chamber set-up for the mutual coupling measurements of the dual-band planar (9×9) array. AUT- array under test.

The mutual coupling measurements were carried out using the experimental set-up shown in Fig. A.7. The set-up was placed inside the anechoic chamber to avoid external disturbances which might influence the performance. The key technical details of the set-up are summarised in Table A.1.

Appendix B

Dual-Band Phased Arrays with Symmetric Comb-Slot-Loaded Patches

B.1 Linear H-plane array

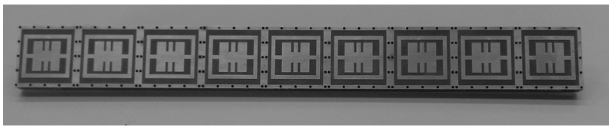

Figure B.1: Fabricated 9-element H-plane linear array.

This appendix presents a performance summary of the linear and planar dual-band arrays employing the symmetric comb-slot loaded patch antenna, introduced in chapter 4. The measured results of the linear 9-element H-plane array (fabricated model shown in Fig. B.1) are presented in Figs. B.2-B.3. The dual-band characteristic is maintained consistently for both the centre and edge elements. The measured radiation patterns of the centre (no: 5) and edge (no: 1) elements of the linear array exhibit good conformance, along the principal operational planes at both the operational bands. The performances with cross-polarisation levels less than -18 dB, are similar to those obtained with the comb-slot-loaded patch in linear array, and are well suited for scanning applications.

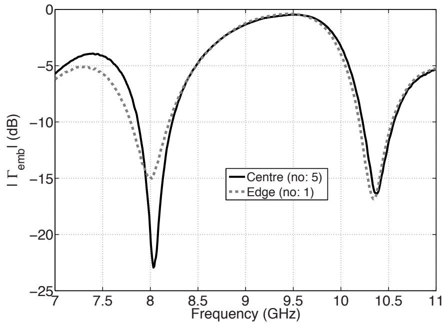

Figure B.2: Measured embedded reflection coefficient of centre and edge elements.

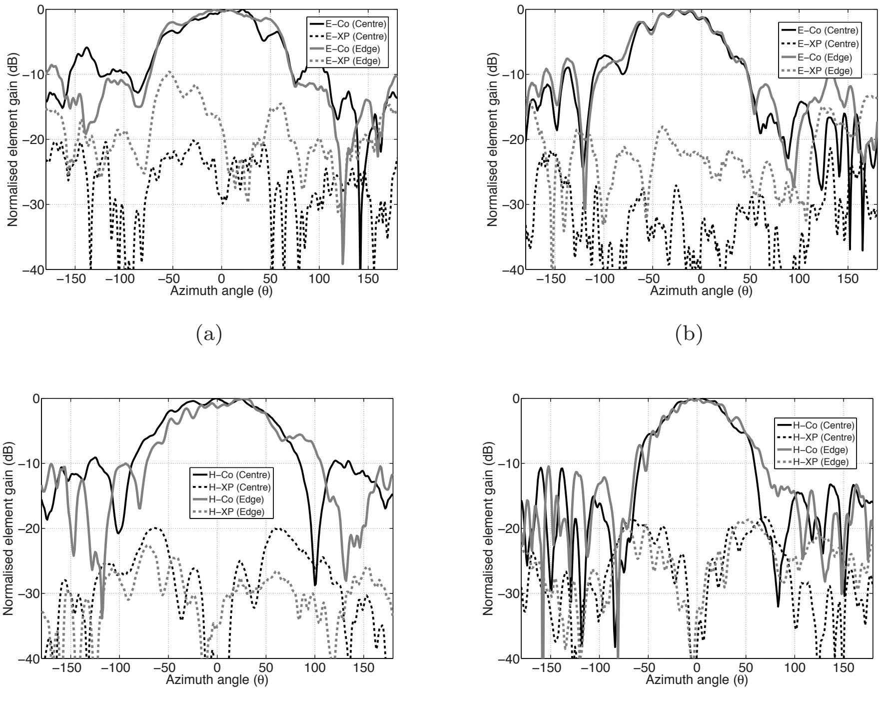

(a)

(b)

(c)

(d)

Figure B.3: Measured embedded radiation patterns. (a)- E-plane at 8 GHz (f_L), (b)- E-plane at 10.3 GHz (f_H), (c)- H-plane at 8 GHz (f_L) and (d)- H-plane at 10.3 GHz (f_H).

B.2 Planar array

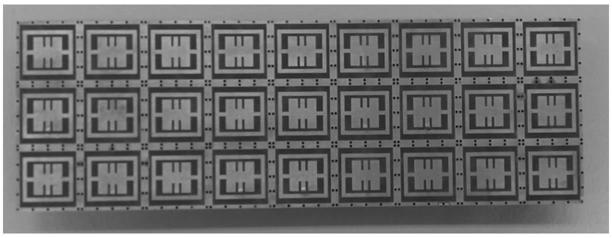

Figure B.4: Fabricated 27-element planar dual-band phased array.

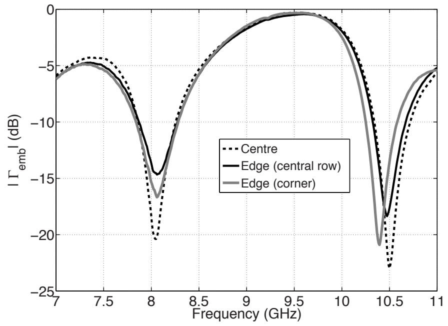

Figure B.5: Measured embedded reflection coefficient of centre and edge elements.

The performance summary of the 27-element planar array (shown in Fig. B.4) are presented in Figs B.5-B.9. The array exhibits well-defined dual-band performance supporting a maximum frequency ratio of 1.35:1. Bandwidths of 360 MHz and 410 MHz are achieved at the low and high frequency bands respectively. The conformance in the impedance matching between different array elements is also evident from Fig. B.5. This behavioural conformance is significant, given the small size of the planar array.

Measured embedded radiation patterns show similar performances for both the edge and centre elements of the array. Finally, wide-angle scanning up to maximum of 60^o and 50^o are achieved along both the principal E- and H-planes, at the low and high frequency bands respectively (Figs. B.8-B.9). The small size of the array (3-elements), along the E-plane, results in very broad scanning patterns along this plane at both the operational bands. Grating-lobe-free scanning performance is achieved up to a maximum of 50^o, at the high frequency band, which can be inferred more clearly from the high frequency H-plane scanning performance (Fig. B.9b). The array antenna's unit-cell measures $0.40\lambda \times 0.40\lambda$ and $0.54\lambda \times 0.54\lambda$ at the low and high frequency bands respectively.

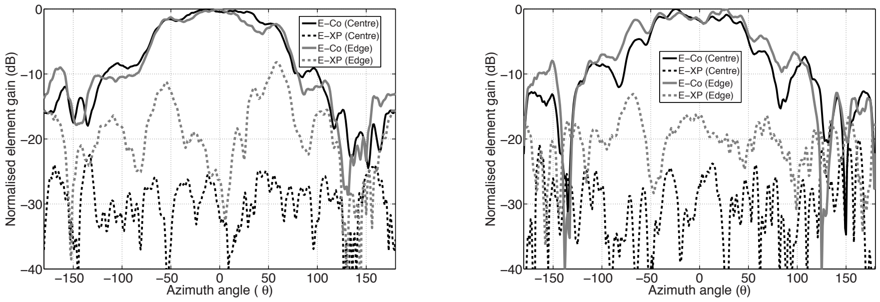

(a) (b)

Figure B.6: Measured E-plane embedded patterns. (a)- 8 GHz (f_L), (b)- 10.5 GHz (f_H).

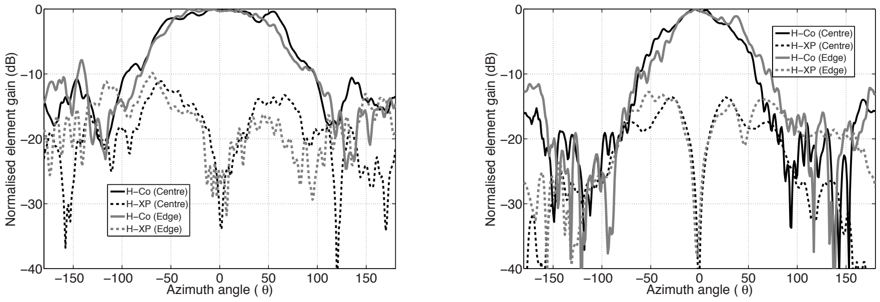

(a) (b)

Figure B.7: Measured H-plane embedded patterns. (a)- 8 GHz (f_L), (b)- 10.5 GHz (f_H).

This dual-band antenna variant has hence been successfully applied for array operations. The novel characteristics of this array include the frequency ratio, wide-angle scanning, good sub-band bandwidths and the low-profile electrical dimensions of the array antenna. The results henceforth serve as a well-suited complement for the original comb-slot-loaded antenna array.

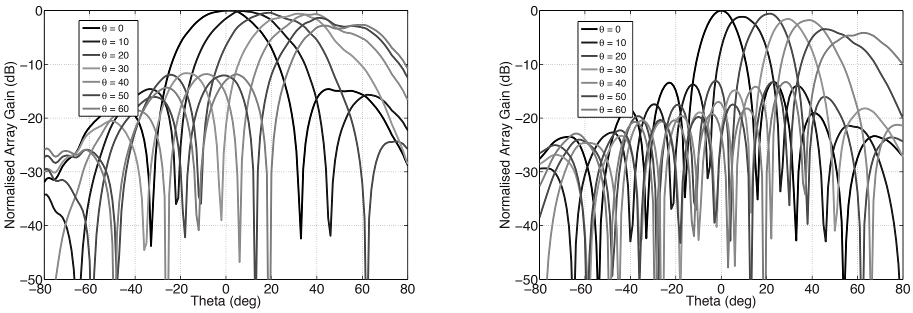

(a) (b)

Figure B.8: Measured beam scanning performance at 8 GHz (f_L). (a)- E-plane, (b)- H-plane.

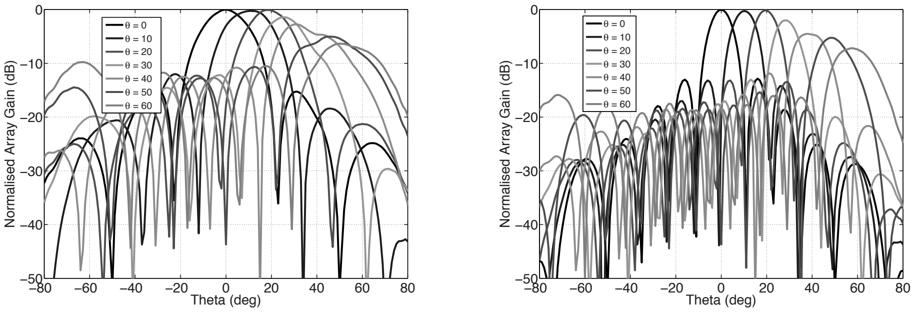

(a) (b)

Figure B.9: Measured beam scanning performance at 10.5 GHz (f_H). (a)- E-plane, (b)- H-plane.

Appendix C

Additional Results of the Crossed L-Bar Patch Antenna

C.1 Flexible resonance characteristic

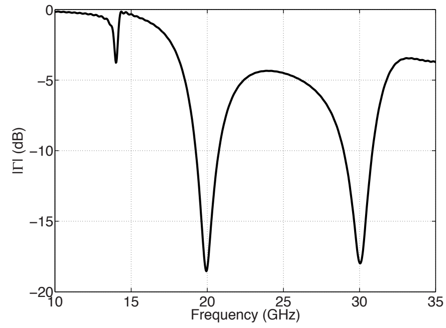

Figure C.1: Demonstration of 1) enhancement of third resonance and 2) shifting the third and fourth resonances to ECC Satellite Network bands (19.7-20.2 GHz and 29.50-30 GHz).

As a demonstration of the crossed L-bar patch antenna's inherent flexible resonance capability, the first and second resonances are suppressed, while the third and fourth resonances are equally tuned and shifted exactly to the satellite network bands (19.7-20.2 GHz and 29.5-30 GHz) in the Ka-band, as defined by the ECC and CEPT [87]. The input reflection coefficient ($|\Gamma_{in}|$) plot of the corresponding version of the antenna, obtained using full-wave (CST-MWS) simulations is presented in Fig. C.1. The radiation patterns at the operational sub-bands are similar to the patterns of the second and third sub-bands, obtained with the quad-band version (refer Fig. 5.16(b-c)). The antenna is linearly-polarised in this case.

C.2 Elliptically-polarised crossed L-bar patch antenna

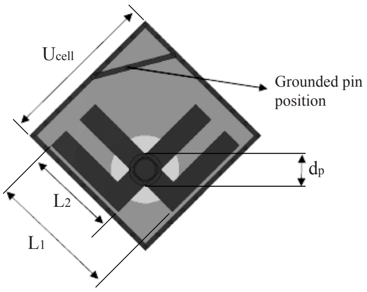

Figure C.2: Grounded pin concept used for achieving elliptical polarisation.

In order to illustrate the antenna's capability to support elliptical polarisation, a modified grounded-pin arrangement as shown Fig. C.2 is used. This arrangement aims to achieve elliptical polarisation in the first two bands of the antenna. There are two key steps involved in this procedure. The first step involves the addition of a metal strip connecting the cavity linings on either side of the diagonal. The connecting strip is slightly slanted in order to disturb the orientation of the magnetic current distribution supported by the metal patch and cavity loop arrangement. The metal strip should be placed at a distance of $\lambda/8$ from the patch edge (refer Fig. C.2), defined at the target operational band. In the case presented here, λ defined at the second operational band (16.5 GHz) is used. The second step is the use of a ground via pin placed on the metal strip on the left side of the diagonal (refer to Fig. C.2 for via pin position). The combination proposed is similar to, and inspired from the use of corner clipping in patch antennas and grounded pins in PIFA antenna designs. In addition to this, the position of the grounded via pin needs to be off the diagonal plane, in order to disturb the symmetric magnetic current distribution. The resulting structure hence disturbs the magnetic current distribution on the patch producing left-handed polarised waves [86].

A snapshot of the fabricated antenna with the connector assembly is shown in Fig. C.3a. The measured reflection coefficient, presented in Fig. C.4, exhibits good conformance with simulations. A linearly-polarised wideband horn antenna (Fig. C.3b) was used as the reference antenna for the pattern measurements, as its operational range (2-20 GHz) covers the first and second operational sub-bands. Radiation patterns were measured for two cases wherein the E-plane of the reference horn antenna was

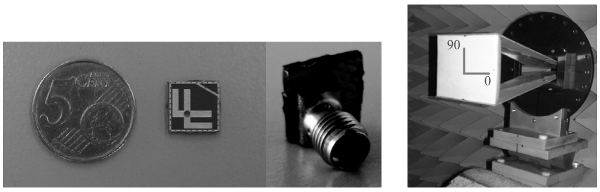

(a) (b)

Figure C.3: (a)- Fabricated quad-band antenna and connector assembly. (b)- Wideband reference horn antenna.

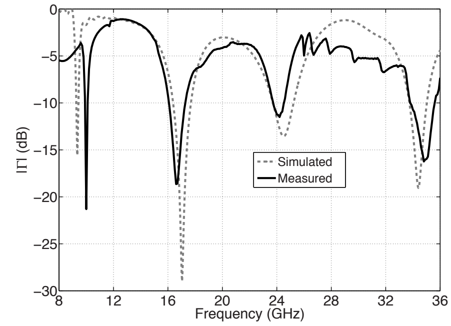

Figure C.4: Measured input reflection coefficient $|\Gamma_{in}|$.

oriented along both the 0^o and 90^o planes (refer Fig. C.3b). The measured radiation patterns at 9.2 GHz and 16.4 GHz, presented in Fig. C.5a-b, are analysed first. Due to the elliptically-polarised behaviour of the antenna in these bands, the patterns exhibit similar characteristics when computed for both the aforementioned orientations of the reference horn antenna (refer Fig. C.3b). It can also be inferred that the axial ratio is maintained below 3 dB for all angles in both the targeted sub-bands of operation (9.7 GHz and 16.4 GHz).

The patterns at 24.1 GHz and 34.3 GHz (see Fig. C.5c-d) are analysed next. In this case, the variation in the pattern characteristics for different orientations of the reference horn antenna clearly exhibits a co- and cross-polarisation performance. The co- and cross-polarisation behaviour corresponds to the 90^o and 0^o orientations of the reference horn antenna respectively (Fig. C.3b). The measurements hence demonstrate the antenna's capability and versatility to maintain quad-band operation with linear as well as elliptical polarisations at the respective operational sub-bands. Furthermore, the omni-directional patterns supported by the antenna, along with it's compact size, measuring only $0.365\lambda_L$ x $0.365\lambda_L$, at lowest operational band, are characteristics suitable for integration in satellite user terminals [88–90].

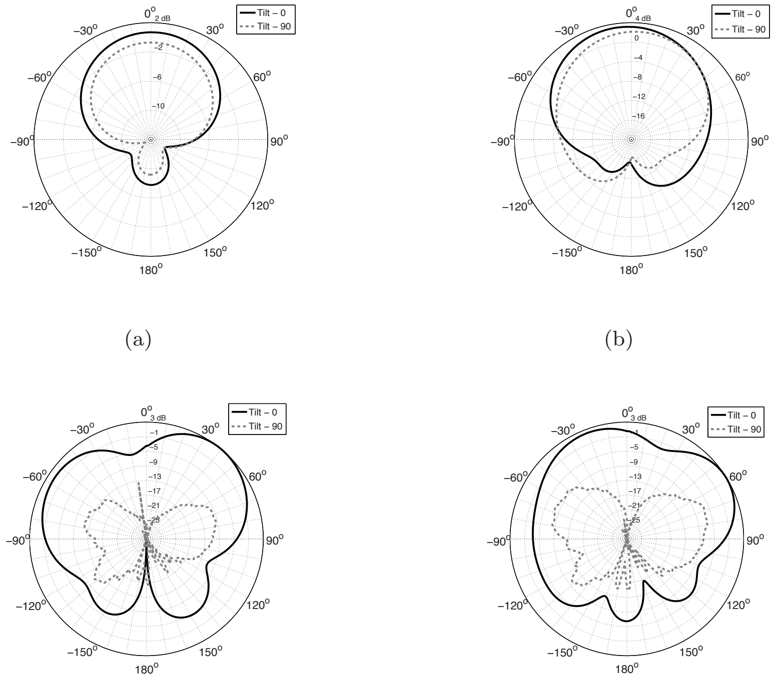

(a)

(b)

(c)

(d)

Figure C.5: Measured radiation patterns at the operational bands. (a) 9.1 GHz, (b) 16.4 GHz, (c) 24.1 GHz and (d) 34.3 GHz.

C.3 Performance variation in planar arrays of crossed L-bar patch antennas

The variation in the measured performances between the edge and centrally embedded elements in the planar (7×7) array are summarised in this section. The measured embedded reflection coefficient ($|\Gamma_{emb}|$) and radiation patterns, of different array elements, are used for the comparative analysis. It is evident from the comparative plot, presented in Fig. C.6, that the dual-band characteristic is consistently maintained for elements in the centre, middle and edge of the array. The band placements are also well-maintained, serving as an important verification of the impedance matching characteristics of the array, on the whole.

Secondly, examination of the variation of the radiation patterns of the centre (no: 25) and edge (no: 49) elements shows good conformance (Figs. C.7-C.8), along both the principal planes of operation. This is significant, given the small size of the planar array prototype (7×7). The array's ability to support well-defined dual-band performance with a large frequency ratio (1.76:1) and consistent radiation patterns in both the edge and centrally embedded elements has hence been experimentally demonstrated.

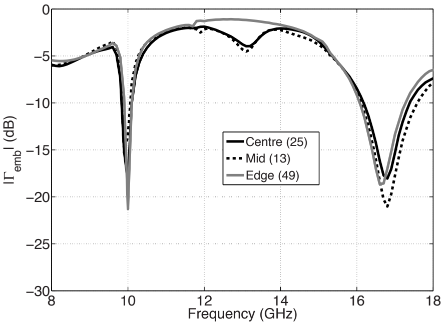

Figure C.6: Variation of embedded reflection coefficient between centre (no: 25), middle (no: 13) and edge (no: 49) elements in planar (7×7) array.

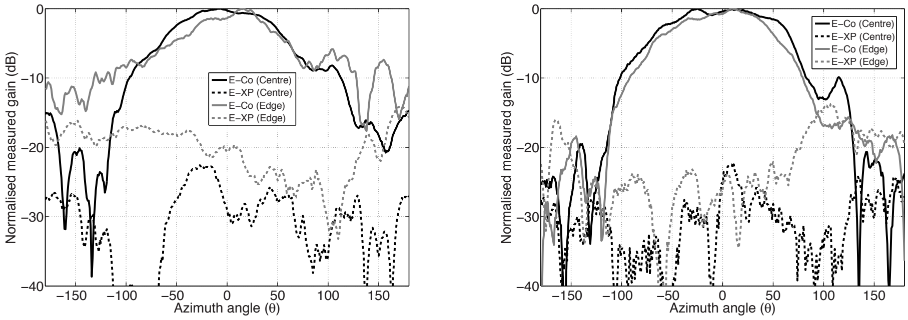

(a)

(b)

Figure C.7: Measured embedded radiation patterns of elements in planar array. (a) E-plane at 9.9 GHz and (b) E-plane at 16.4 GHz.

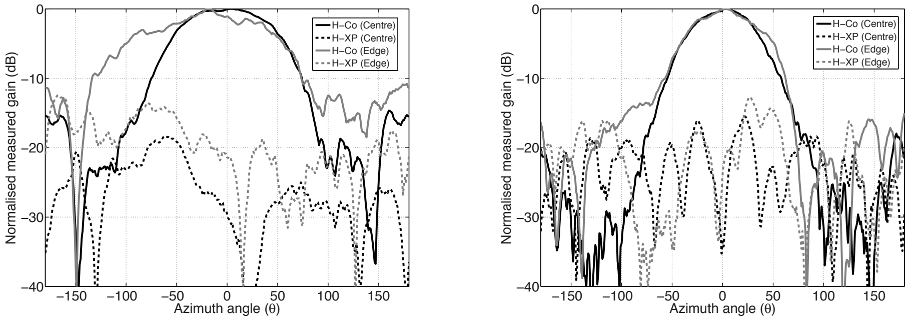

(a) (b)

Figure C.8: Measured embedded radiation patterns of elements in planar array. (a) H-plane at 9.9 GHz, (b) H-plane at 16.4 GHz.

Appendix D

Dual-Band Arrays with Single L-Bar Patch Antennas

D.1 Dual-band single L-bar patch antenna

Finally, the performance characteristics of dual-band antenna variants, with the use of single L-bar geometry is elucidated. Depending on the L-bar chosen, vertical or horizontal polarisation can be achieved, as previously mentioned in Section 5.2. The use of single L-bar, instead of the crossed L-bar arrangement, results in smaller electrical patch dimensions, which moves the resonance bands to the high frequencies. Larger unit-cell and L-bar dimensions are required to move the operational bands to the lower frequencies. But, this would inevitably impair the scanning performance to a large extent, when implemented in array. Therefore, the unit-cell dimensions of this single L-bar variant ($10mm \times 10mm$) are the same as that of the crossed L-bar dual-band antenna, presented in Section 5.3.

(a) (b)

Figure D.1: Dual-band single L-bar patch antenna. (a)- simulated vertically-polarised (VP) variant and (b)- fabricated prototype.

The fabricated prototype of the single L-bar patch antenna is shown in Fig. 5.32b. The experimental results for the stand-alone antenna are presented in Figs. 5.33 - 5.34 The measured impedance performance of the single L-bar antenna shows well-defined dual-band operation with a maximum frequency ratio of 1.5:1. The sub-band bandwidths are at 1.1 GHz and 930 MHz respectively. The radiation patterns are also consistent at both the bands with low levels of cross-polarisation(less than -13 dB). The single L-bar antenna was also optimised for performance in linear (1 × 7) and planar (7 × 7) arrays, exhibiting grating-lobe free scanning performance up to 50 degrees and 20 degrees, at the low and high frequency bands respectively. The limitation on the scanning performance is primarily due to the large electrical dimensions of the unit-cell, which measures $0.77\lambda \times 0.77\lambda$, at the high frequency band of operation. An extended summary of the array results is presented in Appendix D.

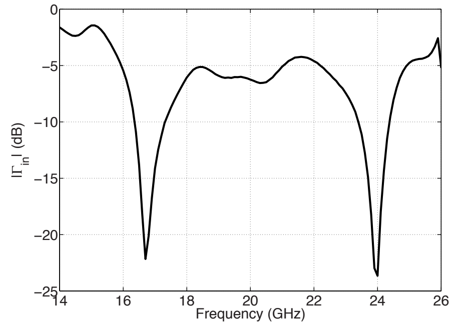

Figure D.2: Measured input reflection coefficient ($|\Gamma_{in}|$) of the single L-bar patch antenna.

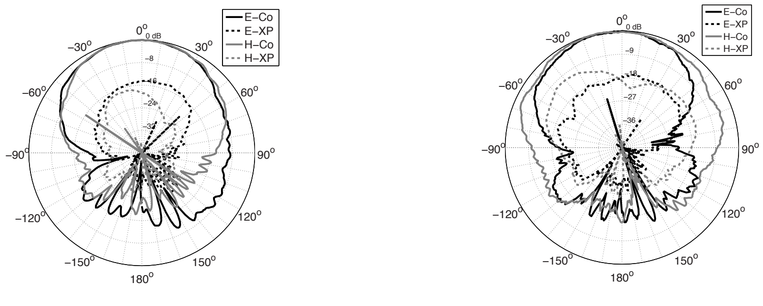

(a) (b)

Figure D.3: Measured radiation patterns.(a)- 16.5 GHz and (b)- 24.1 GHz.

D.2 Linear array

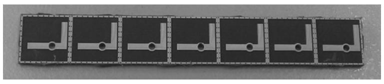

Figure D.4: Fabricated linear (1 × 7) array prototype.

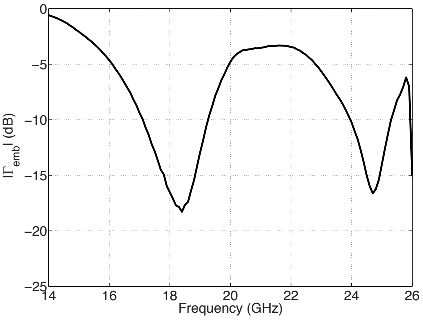

Figure D.5: Measured embedded reflection coefficient (Γ_{emb}) of the centre element (no: 4) in linear (1 × 7) array.

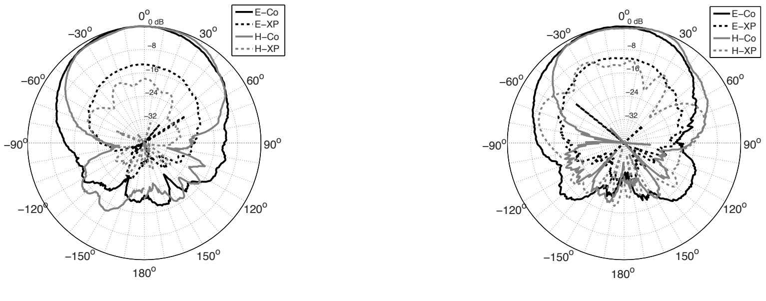

(a)

(b)

Figure D.6: Measured embedded radiation patterns of centre element (no: 4) in linear array. (a)- 18 GHz and (b)- 24.5 GHz.

The fabricated prototype of the 7-element linear array with single L-bar patch antennas is shown in Fig. D.1. The measured embedded reflection coefficient and the radiation patterns of the centre element (no: 4) of the linear array are presented in Figs. D.2 and D.3 respectively. The array supports dual-band operation with a frequency ratio of 1.5:1. Measured bandwidths are at 2.2 GHz and 1.3 GHz respectively. The radiation patterns are also consistent at both the operational bands, with cross polarisation levels less than -14 dB. The scanning patterns obtained along the H-plane (axis) of the array are presented in Fig. D.4. The unit-cell dimensions, which measure $0.78\lambda \times 0.78\lambda$, at the high frequency band, restricts the maximum scanning angle (θ_{max}) to only 20 degrees. However, wide-angle scanning up to a maximum of 50 degrees is possible at the low frequency band.

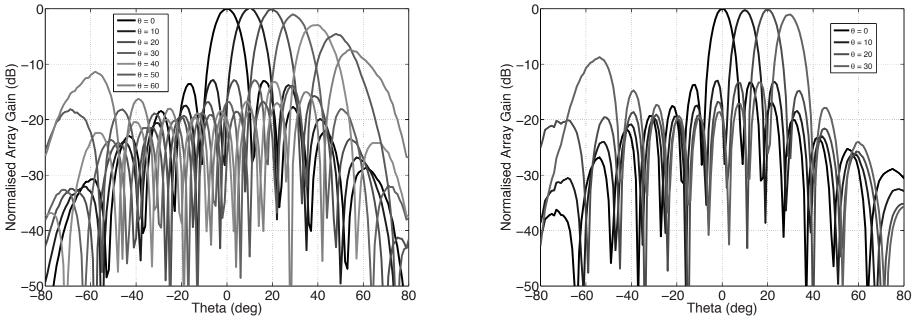

(a)

(b)

Figure D.7: Measured beam scanning performance of linear array. (a) 18 GHz and (b) 24.5 GHz.

D.3 Planar array

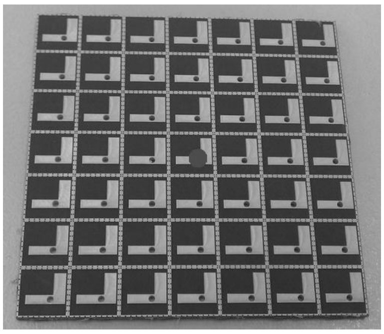

Figure D.8: Fabricated planar (7 × 7) array prototype.

The fabricated 49-element planar array prototype with single L-bar patch antennas is shown in Fig. D.5. The embedded reflection coefficient (Fig. D.6) and radiation patterns (Fig. D.7) measured for the centre element (no: 25, indicated with a red circle in Fig. D.5) exhibit characteristics similar to that of the centre element of the linear array, presented in the previous section. The element loading along both the principal planes, in this case, result in more directive patterns along the E-plane as well, at the high frequency band of operation. Cross-polarisation levels less than -14 dB are achieved in both the bands. The dual-band characteristic is well-maintained in this case with a frequency ratio of 1.5:1, and measured sub-band bandwidths are at 900 MHz and 1.5 GHz respectively.

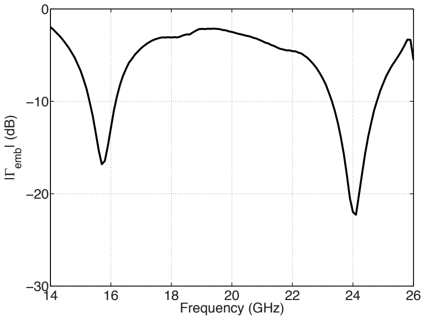

Figure D.9: Measured embedded reflection coefficient (Γ_{emb}) of the centre element (no: 25) in planar (7×7) array.

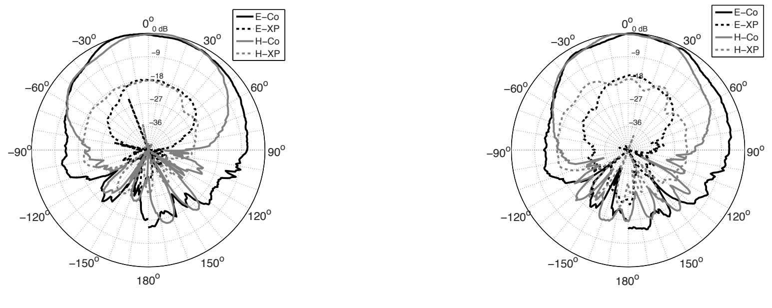

(a) (b)

Figure D.10: Measured embedded radiation patterns of centre element (no: 25) in planar array. (a)- 15.5 GHz and (b)- 24 GHz.

The scanning performances of the uniformly-excited planar array are presented in Fig. D.8. The array supports grating lobe-free scanning up to a maximum of 50 degrees and 20 degrees at the low and high frequency bands. The limitation in terms of the maximum scanning angle ($\theta_{max} = 20^o$) at the high frequency band, due to the larger unit-cell dimension ($0.78\lambda \times 0.78\lambda$), is evident along both the principal operational planes (E/H). Finally, it is worth mentioning that low levels of sidelobes (less than -13 dB) are maintained for all supported scanning angles, even with a uniformly-excited array. Other ways of enhancing the scanning performance by improving the low-profile dimensions of the single L-bar patch antenna could be investigated as part of future research.

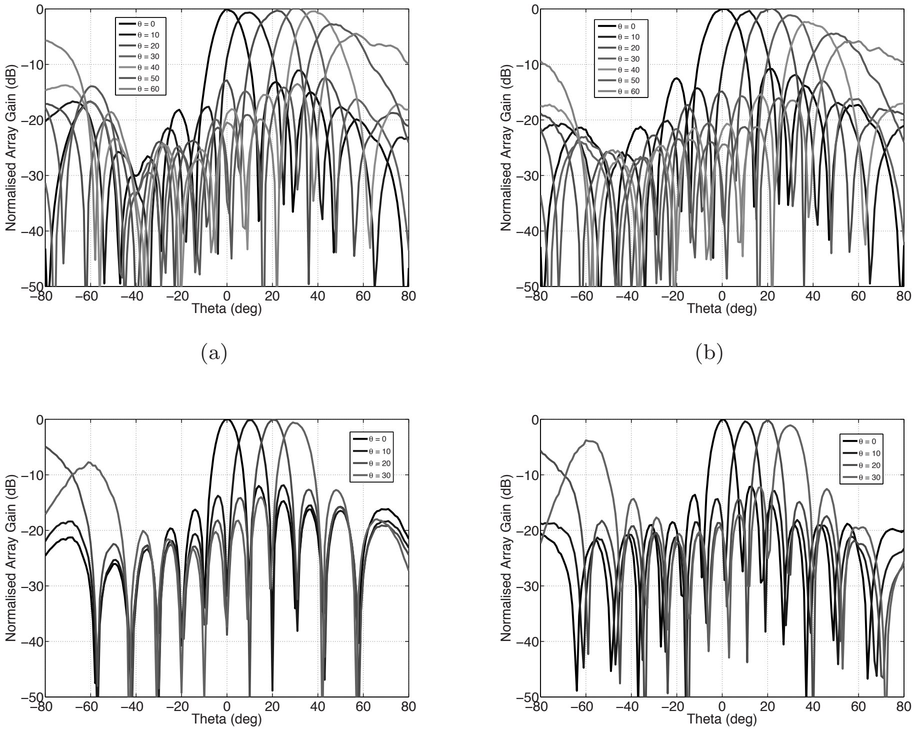

(a) (b)

(c) (d)

Figure D.11: Measured beam scanning performance of planar array. (a) E-plane at 15.5 GHz, (b) H-plane at 15.5 GHz, (c) E-plane at 24 GHz and (d) H-plane at 24 GHz.

Bibliography

[1] E. Brookner, "Never ending saga of phased array breakthroughs," in *Phased Array Systems and Technology (ARRAY), 2010 IEEE International Symposium on*, 2010.

[2] A. Cetronio, M. D'Urso, A. Farina, C. Lanzieri, L. Timmoneri, and M. Teglia, "Phased array systems and technologies in selex-sistemi integrati: State of art and new challenges," in *Phased Array Systems and Technology (ARRAY), 2010 IEEE International Symposium on*, oct. 2010, pp. 44 –49.

[3] J. Herd, D. Carlson, S. Duffy, M. Weber, G. Brigham, M. Rachlin, D. Cursio, C. Liss, and C. Weigand, "Multifunction phased array radar (mpar) for aircraft and weather surveillance," in *Radar Conference, 2010 IEEE*, may 2010, pp. 945 –948.

[4] S. Kemkemian and M. Nouvel-Fiani, "Toward common radar and ew multifunction active arrays," in *Phased Array Systems and Technology (ARRAY), 2010 IEEE International Symposium on*, oct. 2010, pp. 777 –784.

[5] A. Ouacha, A. Fredlund, J. Andersson, H. Hindsefelt, V. Rinaldi, and C. Scattoni, "Se-it joint m-aesa program: Overview and status," in *Phased Array Systems and Technology (ARRAY), 2010 IEEE International Symposium on*, oct. 2010, pp. 771 –776.

[6] A. Stark, A. Dreher, H. Fischer, A. Geise, R. Gieron, M. Heckler, S. Holzwarth, C. Hunscher, A. Jacob, K. Kuhlmann, O. Litschke, D. Lohmann, W. Simon, F. Wotzel, and D. Zahn, "Santana: Advanced electronically steerable antennas at ka-band," in *Antennas and Propagation, 2009. EuCAP 2009. 3rd European Conference on*, march 2009, pp. 471 –478.

[7] Raytheon. (2011) Naval radars: Dual band radar (dbr). Internet. Raytheon Company. [Online]. Available: http://www.raytheon.com/businesses/rids/businesses/scs/navalradars/dbr/index.html.2012

[8] STARS. (2010-2014) Sensor technology applied in reconfigurable systems for sustainable security (stars) project. Internet. [Online]. Available: www.starsproject.nl

[9] T. Group. (2012) Integrated mast. Online. [Online]. Available: https://www.thalesgroup.com/en/innovation/integrated-mast

[10] R. J. Mailloux, *Phased Array Antenna Handbook, 2nd Edition.* Artech House, Boston, MA, 2005.

[11] D. Schaubert, S. Kasturi, A. Boryssenko, and W. Elsallal, "Vivaldi antenna arrays for wide bandwidth and electronic scanning," in *Antennas and Propagation, 2007. EuCAP 2007. The Second European Conference on*, nov. 2007, pp. 1 –6.

[12] D. Schaubert, W. Elsallal, S. Kasturi, A. Boryssenko, M. Vouvakis, and G. Paraschos, "Wide bandwidth arrays of vivaldi antennas," in *Wideband, Multiband Antennas and Arrays for Defence or Civil Applications, 2008 Institution of Engineering and Technology Seminar on*, march 2008, pp. 1 –20.

[13] A. Ellgardt, "Wide-angle scanning wide-band phased array antennas," Ph.D. dissertation, KTH-Stockholm, Sweden, 2009.

[14] A. Ellgardt and A. Wikstrom, "A single polarized triangular grid tapered-slot array antenna," *Antennas and Propagation, IEEE Transactions on*, vol. 57, no. 9, pp. 2599–2607, 2009.

[15] C. Rodenbeck, S.-G. Kim, W.-H. Tu, M. Coutant, S. Hong, M. Li, and K. Chang, "Ultra-wideband low-cost phased-array radars," *Microwave Theory and Techniques, IEEE Transactions on*, vol. 53, no. 12, pp. 3697–3703, 2005.

[16] S. Kasturi and D. Schaubert, "Effect of dielectric permittivity on infinite arrays of single-polarized vivaldi antennas," *Antennas and Propagation, IEEE Transactions on*, vol. 54, no. 2, pp. 351–358, 2006.

[17] B. Munk, R. Taylor, T. Durharn, W. Croswell, B. Pigon, R. Boozer, S. Brown, M. Jones, J. Pryor, S. Ortiz, J. Rawnick, K. Krebs, M. Vanstrum, G. Gothard, and D. Wiebelt, "A low-profile broadband phased array antenna," in *Antennas and Propagation Society International Symposium, 2003. IEEE*, vol. 2, june 2003, pp. 448 – 451 vol.2.

[18] R. Hansen, "Linear connected arrays [coupled dipole arrays]," *Antennas and Wireless Propagation Letters, IEEE*, vol. 3, no. 1, pp. 154–156, 2004.

[19] R. Erickson, R. Gunnarsson, T. Martin, L. G. Huss, L. Pettersson, P. Andersson, and A. Ouacha, "Wideband and wide scan phased array microstrip patch antennas for small platforms," in *Antennas and Propagation, 2007. EuCAP 2007. The Second European Conference on*, 2007, pp. 1–6.

[20] A. Neto, D. Cavallo, G. Gerini, and G. Toso, "Scanning performances of wideband connected arrays in the presence of a backing reflector," *Antennas and Propagation, IEEE Transactions on*, vol. 57, no. 10, pp. 3092–3102, 2009.

[21] A. Brown, Y. Zhang, D. Kant, and J. de Vaate, "Wideband planar phased arrays for the square kilometre array," in *Phased Array Systems and Technology (ARRAY), 2010 IEEE International Symposium on*, 2010, pp. 616–623.

[22] R. Sarkis and C. Craeye, "Circular array of wideband 3d vivaldi antennas," in *Electromagnetic Theory (EMTS), 2010 URSI International Symposium on*, 2010, pp. 792–794.

[23] D. Cavallo, A. Neto, and G. Gerini, "A 10.5-14.5 ghz wide-scanning connected array of dipoles with common-mode rejection loops to ensure polarization purity," in *Antennas and Propagation Society International Symposium (APSURSI), 2010 IEEE*, 2010, pp. 1–4.

[24] J. Kasemodel, C.-C. Chen, and J. Volakis, "Broadband planar wide-scan array employing tightly coupled elements and integrated balun," in *Phased Array Systems and Technology (ARRAY), 2010 IEEE International Symposium on*, oct. 2010, pp. 467 –472.

[25] L. Cifola, D. Cavallo, G. Gerini, and A. Morini, "Integrated filtering in a planar array of connected dipoles including a common-mode rejection module," in *Radar Conference (EuRAD), 2012 9th European*, 2012, pp. 417–420.

[26] S. Holland, D. Schaubert, and M. N. Vouvakis, "A 7-21 ghz dual-polarized planar ultrawideband modular antenna (puma) array," *Antennas and Propagation, IEEE Transactions on*, vol. 60, no. 10, pp. 4589–4600, 2012.

[27] L. Infante, S. Mosca, and M. Teglia, "Low-profile wide-band wide-angle-scan antenna array element," in *Antennas and Propagation (EUCAP), 2012 6th European Conference on*, 2012, pp. 638–642.

[28] S.-H. Hsu, Y.-J. Ren, and K. Chang, "A dual-polarized planar-array antenna for s-band and x-band airborne applications," *Antennas and Propagation Magazine, IEEE*, vol. 51, no. 4, pp. 70–78, 2009.

[29] X. Qu, S. Zhong, and Y. M. Zhang, “Dual-band dual-polarised microstrip antenna array for sar applications,” *Electronics Letters*, vol. 42, no. 24, pp. 1376–1377, 2006.

[30] C. Coman, I. Lager, and L. Ligthart, “The design of shared aperture antennas consisting of differently sized elements,” *Antennas and Propagation, IEEE Transactions on*, vol. 54, no. 2, pp. 376 – 383, feb. 2006.

[31] I. Lager and M. Simeoni, “Experimental investigation of the mutual coupling reduction by means of cavity enclosure of patch antennas,” in *Antennas and Propagation, 2006. EuCAP 2006. First European Conference on*, nov. 2006, pp. 1 –5.

[32] I. Lager, C. Trampuz, M. Simeoni, and L. Ligthart, “Interleaved array antennas for fmcw radar applications,” *Antennas and Propagation, IEEE Transactions on*, vol. 57, no. 8, pp. 2486 –2490, aug. 2009.

[33] I. Lager, C. Trampuz, M. Simeoni, L. Ligthart, and P. v. Genderen, “Puzzling radiators functionality enhancement by means of shared aperture antennas,” in *Antennas for ubiquitous radio services in a wireless information society. WiSE project,*, 2010.

[34] M. Simeoni, I. Lager, and C. Coman, “Interleaving sparse arrays: a new way to polarization-agile array antennas?” in *Antennas and Propagation Society International Symposium, 2007 IEEE*, june 2007, pp. 3145 –3148.

[35] M. Simeoni, I. E. Lager, C. I. Coman, and A. G. Roederer, “Implementation of polarization agility in planar phased-array antennas by means of interleaved subarrays,” *Radio Science*, vol. 44, no. 5, pp. n/a–n/a, 2009. [Online]. Available: http://dx.doi.org/10.1029/2009RS004175

[36] L. Pringle, P. Harms, S. Blalock, G. Kiesel, E. Kuster, P. Friederich, R. Prado, J. Morris, and G. Smith, “A reconfigurable aperture antenna based on switched links between electrically small metallic patches,” *Antennas and Propagation, IEEE Transactions on*, vol. 52, no. 6, pp. 1434–1445, 2004.

[37] G. Jaworski, T. Maleszka, S. Gruszczynski, and K. Wincza, “Dual frequency amp; dual- linear polarization integrated antenna array for application in synthetic aperture radar,” in *Radar Conference (EuRAD), 2010 European*, 2010, pp. 523–526.

[38] N. Haider, D. Tran, A. Roederer, and A. Yarovoy, “Reconfigurable l/s band phased array,” *Electronics Letters*, vol. 47, no. 23, pp. 1265–1266, 2011.

[39] R. Di Bari, T. Brown, S. Gao, M. Notter, D. Hall, and C. Underwood, "Dual-polarized printed s-band radar array antenna for spacecraft applications," *Antennas and Wireless Propagation Letters, IEEE*, vol. 10, pp. 987–990, 2011.

[40] K. Lee, K. Luk, K. Mak, and S. Yang, "On the use of u-slots in the design of dual-and triple-band patch antennas," *Antennas and Propagation Magazine, IEEE*, vol. 53, no. 3, pp. 60–74, 2011.

[41] S. Maci, G. Biffi Gentili, P. Piazzesi, and C. Salvador, "Dual-band slot-loaded patch antenna," *Microwaves, Antennas and Propagation, IEE Proceedings*, vol. 142, no. 3, pp. 225 –232, jun 1995.

[42] S. Maci and G. Gentili, "Dual-frequency patch antennas," *Antennas and Propagation Magazine, IEEE*, vol. 39, no. 6, pp. 13–20, 1997.

[43] T. Chan and Y. Hwang, "A dual-band microstrip array antenna," in *Antennas and Propagation Society International Symposium, 1995. AP-S. Digest*, vol. 4, 1995, pp. 2132–2135 vol.4.

[44] K.-P. Yang and K.-L. Wong, "Dual-band circularly-polarized square microstrip antenna," *Antennas and Propagation, IEEE Transactions on*, vol. 49, no. 3, pp. 377–382, 2001.

[45] D. Choi, Y. Cho, and S.-O. Park, "Dual-band and dual-polarised microstrip antenna," *Electronics Letters*, vol. 42, no. 2, pp. 68–69, 2006.

[46] K. Yegin, D. Morris, N. Bally, R. Snoeyink, and W. Livengood, "Integrated gps and sdars antenna," U.S. Patent US20 060 097 924A1, May 11, 2006.

[47] K.-F. Lee, S. Yang, and A. Kishk, "Dual- and multiband u-slot patch antennas," *Antennas and Wireless Propagation Letters, IEEE*, vol. 7, pp. 645–647, 2008.

[48] K. Jhamb, L. Li, and K. Rambabu, "Novel-integrated patch antennas with multi-band characteristics," *Microwaves, Antennas Propagation, IET*, vol. 5, no. 12, pp. 1393–1398, 2011.

[49] C.-Y. Chiu, C.-H. Cheng, R. Murch, and C. Rowell, "Reduction of mutual coupling between closely-packed antenna elements," *Antennas and Propagation, IEEE Transactions on*, vol. 55, no. 6, pp. 1732–1738, 2007.

[50] M. Ghaderi and N. Karmakar, "Frequency selective surface for reducing mutual coupling in antenna arrays," in *Microwave Conference Proceedings (APMC), 2011 Asia-Pacific*, 2011, pp. 1877–1880.

[51] H. Farahani, M. Veysi, M. Kamyab, and A. Tadjalli, “Mutual coupling reduction in patch antenna arrays using a uc-ebg superstrate,” *Antennas and Wireless Propagation Letters, IEEE*, vol. 9, pp. 57–59, 2010.

[52] D. M. Pozar, “Analysis of finite phased arrays of printed dipoles,” *Antennas and Propagation, IEEE Transactions on*, vol. 33, no. 10, pp. 1045–1053, 1985.

[53] T.-H. Chio and D. Schaubert, “Parameter study and design of wide-band widescan dual-polarized tapered slot antenna arrays,” *Antennas and Propagation, IEEE Transactions on*, vol. 48, no. 6, pp. 879–886, 2000.

[54] H. Holter and H. Steyskal, “On the size requirement for finite phased-array models,” *Antennas and Propagation, IEEE Transactions on*, vol. 50, no. 6, pp. 836–840, 2002.

[55] D. M. Pozar, “Finite phased arrays of rectangular microstrip patches,” *Antennas and Propagation, IEEE Transactions on*, vol. 34, no. 5, pp. 658–665, 1986.

[56] B.-J. Jang, Y.-K. Lee, H.-W. Moon, Y.-J. Yoon, and H.-K. Park, “Analysis of finite-phased arrays of aperture-coupled stacked microstrip antennas,” *Antennas and Propagation, IEEE Transactions on*, vol. 45, no. 8, pp. 1201–1204, 1997.

[57] D. Pozar and D. Schaubert, “Analysis of an infinite array of rectangular microstrip patches with idealized probe feeds,” *Antennas and Propagation, IEEE Transactions on*, vol. 32, no. 10, pp. 1101–1107, 1984.

[58] E. Rajo-Iglesias, O. Quevedo-Teruel, and L. Inclan-Sanchez, “Mutual coupling reduction in patch antenna arrays by using a planar ebg structure and a multilayer dielectric substrate,” *Antennas and Propagation, IEEE Transactions on*, vol. 56, no. 6, pp. 1648–1655, 2008.

[59] F. Jolani, A. Dadgarpour, and G. Dadashzadeh, “Reduction of mutual coupling between dual-element antennas with new pbg techniques,” in *Antenna Technology and Applied Electromagnetics and the Canadian Radio Science Meeting, 2009. ANTEM/URSI 2009. 13th International Symposium on*, 2009, pp. 1–4.

[60] S. E. Valavan, M. Simeoni, and A. G. Yarovoy, “Impact of truncation on finite-sized dual-band linear phased arrays,” in *Radar Conference (EuRAD), 2012 9th European*, 2012, pp. 622–625.

[61] D. Pozar, “The active element pattern,” *Antennas and Propagation, IEEE Transactions on*, vol. 42, no. 8, pp. 1176–1178, 1994.

[62] D. Kelley and W. Stutzman, "Array antenna pattern modeling methods that include mutual coupling effects," *Antennas and Propagation, IEEE Transactions on*, vol. 41, no. 12, pp. 1625–1632, 1993.

[63] D. M. Pozar, "A relation between the active input impedance and the active element pattern of a phased array," *Antennas and Propagation, IEEE Transactions on*, vol. 51, no. 9, pp. 2486–2489, 2003.

[64] D. Kelley, "Relationships between active element patterns and mutual impedance matrices in phased array antennas," in *Antennas and Propagation Society International Symposium, 2002. IEEE*, vol. 1, 2002, pp. 524–527 vol.1.

[65] J. L. Allen and B. L. Diamond, "Mutual coupling in anrray antennas," Lincoln Labs, MIT, Tech. Rep., 1966.

[66] I. Gupta and A. Ksienski, "Effect of mutual coupling on the performance of adaptive arrays," *Antennas and Propagation, IEEE Transactions on*, vol. 31, no. 5, pp. 785–791, 1983.

[67] R. Jedlicka, M. Poe, and K. Carver, "Measured mutual coupling between microstrip antennas," *Antennas and Propagation, IEEE Transactions on*, vol. 29, no. 1, pp. 147–149, 1981.

[68] L. Lechtreck, "Effects of coupling accumulation in antenna arrays," *Antennas and Propagation, IEEE Transactions on*, vol. 16, no. 1, pp. 31–37, 1968.

[69] E. Penard and J.-P. Daniel, "Mutual coupling between microstrip antennas," *Electronics Letters*, vol. 18, no. 14, pp. 605–607, 1982.

[70] A. Bhattacharyya and L. Shafai, "Surface wave coupling between circular patch antennas," *Electronics Letters*, vol. 22, no. 22, pp. 1198–1200, 1986.

[71] A. Bhattacharyya, "Characteristics of space and surface waves in a multilayered structure [microstrip antennas]," *Antennas and Propagation, IEEE Transactions on*, vol. 38, no. 8, pp. 1231–1238, 1990.

[72] K. Griffith and I. Gupta, "Effect of mutual coupling on the performance of adaptive antennas," in *Antennas and Propagation Society International Symposium, 2008. AP-S 2008. IEEE*, 2008, pp. 1–4.

[73] A. S. C. Svendsen and I. Gupta, "The effect of mutual coupling on the nulling performance of adaptive antennas," *Antennas and Propagation Magazine, IEEE*, vol. 54, no. 3, pp. 17–38, 2012.

[74] G. Kristensson, P. Waller, and A. Derneryd, “Radiation efficiency and surface waves for patch antennas on inhomogeneous substrates,” Lund Institute of Technology, Sweden, Tech. Rep., 2002.

[75] ——, “Radiation efficiency and surface waves for patch antennas on inhomogeneous substrates,” *Microwaves, Antennas and Propagation, IEE Proceedings*, vol. 150, no. 6, pp. 477–483, 2003.

[76] Rogers. (2012) Product selection guide. Online. Rogers Corporation. [Online]. Available: www.rogercorp.com

[77] S. Rikte, G. Kristensson, and M. Andersson, “Propagation in bianisotropic media-reflection and transmission,” *Microwaves, Antennas and Propagation, IEE Proceedings*, vol. 148, no. 1, pp. 29–36, 2001.

[78] J. K. Ali, “A new dual band e-shaped slot antenna design for wireless applications,” in *PIERS Proc. Suzhou, pp. 1258-1261, China, Sept. 12-16*, 2011.

[79] Y. Mushiake, *Self-Complementary Antennas: Principle of Self-Conplementarity for Constant Impedance.* Springer Verlag, London, 1996.

[80] H. Booker, “Slot aerials and their relation to complementary wire aerials (babinet’s principle),” *Electrical Engineers - Part IIIA: Radiolocation, Journal of the Institution of*, vol. 93, no. 4, pp. 620–626, 1946.

[81] D. Tran, F. Tanyer-Tigrek, A. Vorobyov, I. Lager, and L. Ligthart, “A novel cpw-fed optimized uwb printed antenna,” in *Wireless Technologies, 2007 European Conference on*, 2007, pp. 40–43.

[82] F. Tanyer-Tigrek, D. Tran, I. Lager, and L. Ligthart, “Cpw-fed quasi-magnetic printed antenna for ultra-wideband applications,” *Antennas and Propagation Magazine, IEEE*, vol. 51, no. 2, pp. 61–70, 2009.

[83] F. Tanyer-Tigrek, I. Lager, and L. Ligthart, “A cpw-fed printed loop antenna for ultra-wideband applications, and its linear-array performance,” *Antennas and Propagation Magazine, IEEE*, vol. 52, no. 4, pp. 31–40, 2010.

[84] ——, “Experimental validation of a linear array consisting of cpw fed, uwb, printed, loop antennas,” *Antennas and Propagation, IEEE Transactions on*, vol. 58, no. 4, pp. 1411–1414, 2010.

[85] T. Huynh and K.-F. Lee, “Single-layer single-patch wideband microstrip antenna,” *Electronics Letters*, vol. 31, no. 16, pp. 1310–1312, 1995.

[86] A. Ludwig, "The definition of cross polarization," *Antennas and Propagation, IEEE Transactions on*, vol. 21, no. 1, pp. 116–119, 1972.

[87] R.-. ECC, "The use of the frequency bands 17.3-20.2 ghz and 27.5-30.0 ghz by satellite networks," ECC, Gothenburg, Sept. 2010, Tech. Rep., 2010.

[88] R. T. Sanchez, J. R. Mosig, S. Vaccaro, and D. L. del Rio, "Design review of compact and low cost elementary radiating cell for satellite braodcasting automotive receving arrays," in *Proceedings of the 33rd ESA Antenna Workshop, ESA/ESTEC, Oct 2011.*, 2011.

[89] F. Bongard, D. L. del Rio, C. Vigano, and S. Vaccaro, "Switched-beam tx-only ku-band terminal antenna for mobile satellite applications," in *Proceedings of the 33rd ESA Antenna Workshop, ESA/ESTEC, Oct 2011*, 2011.

[90] W. Whittow, A. Chauraya, R. Seager, Y. Varadaxoglou, and P. de Maagt, "Wearable circularly polarised vhf antennas for emergency applications," in *Proc. of the 33rd ESA Antenna Workshop, ESA/ESTEC*, 2011.

Summary

Antenna array front-ends with both frequency and wide-angle beamforming agility will greatly enhance the reconfigurable capabilities of future multifunction radars. Currently, the use of either single-band arrays, with multiple apertures for different radar functions, and ultra-wideband arrays are seen as the two main solutions for multifunction radars. System demands however, can be better satisfied with the use of dual-band arrays due to two main reasons. Firstly, the number of single-band array front-ends used for different target functions can be reduced with the use of dual-band arrays. Secondly, compared to the use of ultra-wideband arrays, dual/multi-band phased arrays can facilitate by providing additional filtering at the antenna element level, reduce interferences from out-of-band signals and also ease efficiency requirements of the T/R modules. The ability to support well-separated bands makes it possible to use the same aperture to support different operational tasks, which mostly require different operational frequencies as well. Further, the addition of wide-angle beamforming is extremely useful for applications involving digital beamforming, a pivotal aspect of modern radars.

The development of dual-band wide-angle scanning phased arrays represents a multilevel research problem which necessitated the compartmentalization of the problem into three major research blocks, these include, 1) the design of novel dual- or multi-band array elements, 2) the development of experimental prototype demonstrators of phased array concepts with wide-angle scanning capability and large frequency ratios ($\geq 1.5 : 1$), and 3) the development of techniques to reduce mutual coupling in patch antenna arrays. Associated supplementary research on the influence of mutual coupling on scanning performance, grid impact on coupling and scanning, truncation impact on impedance of array elements and development of multi-band antennas for SatComm applications have also been successfully carried out.

The major research outputs can be summarized as follows. A novel comb-slot-loaded patch antenna with quasi-magneto-electric radiation characteristics was developed for array applications. There are two key aspects of this antenna design. Firstly, the antenna combines both the electric and magnetic radiation characteristics in the

overall radiation mechanism in a single radiating structure. Secondly, the antenna incorporates a novel “lamppost” feeding architecture, which also provides reactance balancing mechanism aiding in achieving good bandwidths at the operational bands. The dual-band antenna supports a large frequency ratio (1.5:1) and consistent radiation patterns at both bands. Based on this antenna concept, experimental prototypes of both linear and planar arrays, operational in X-band, have been designed and its performance validated. Wide-angle scanning ($\pm 60^o$) is demonstrated at both the operational bands with consistent embedded element patterns.

A novel multi-band radar and communications antenna with extremely low-profile electrical dimensions was developed next. The proposed crossed L-bar antenna's novel and flexible operational features include the support for a maximum of four well-separated operational bands, support for both patch-like and omni-directional radiation patterns, and inherent resonance tuning capability to enhance or suppress any desired band(s) of interest. Experimental prototypes of dual-band linear and planar arrays with the crossed L-bar antenna, operational in X/Ku- and K-bands, have been developed. The demonstrated key features include the large frequency ratios (1.8:1), wide-angle scanning ($\pm 50 - 60^o$) and sub-band bandwidths. The ability of the quad-band version of the antenna to support both ‘patch-like’ and omni-directional radiation patterns, along with its extremely low-profile electrical and physical dimensions, makes it attractive for use in SatComm user terminals.

Finally, a novel dielectric-contrast technique to mitigate mutual coupling between closely spaced array radiators has been proposed. The method uses multilayer substrates, with permittivity contrast between the layers, aiding in the reduction of coupling. The proposed technique removes the need to employ any external structures (like EBGs), thereby leaving the scanning performance of the array unaltered. Furthermore, modal analysis, based on the concept of propagators, has been used to evaluate the difference in the operational mode's characteristics between the homogeneous and multilayer substrate architectures. The effectiveness of the proposed technique has also been verified with experimental linear array prototypes.

In summary, the outputs have, for the first time, demonstrated the potential and feasibility of dual-band phased arrays with wide-angle scanning capability. The major results achieved and presented here, covering aspects of both fundamental research and practical relevance, signify an important evolutionary step forward in the development of dual-band phased arrays for future multifunction radar front-ends.

Samenvatting

Antenne array front-ends met behendigheden in zowel frequentie als brede-hoek bundelvorming zal de her-configureerbare mogelijkheden van toekomstige multifunctionele radars zeer verbeteren. Het gebruik van zowel enkele-band antenne arrays met meerdere openingen voor verschillende radar functies en ultra-breedband antenne arrays worden momenteel gezien als de twee voornaamste oplossingen voor multifunctionele radars. Maar systeemeisen kunnen beter worden voldaan met het gebruik van dubbele-band antenne arrays om de volgende twee redenen. Ten eerste, het aantal enkele-band antenne array front- ends gebruikt voor verschillende beoogde functies kan worden gereduceerd door gebruik te maken van dubbele-band antenne arrays. Ten tweede, vergeleken met ultra-breedband antenne arrays, dubbele/meerdere-band gefaseerde antenne arrays kan faciliteren door het leveren van aanvullend filteren op antenne element niveau, verlaging van interferentie van buiten-de-band signalen en ook verlichten van efficintie eisen voor de T/R modules. De bekwaamheid om banden goed te onderscheiden maakt het mogelijk om dezelfde opening te gebruiken voor verschillende operationele taken dat meestal verschillende operatie frequenties nodig heeft. Bovendien, de toevoeging van brede-hoek bundelvorming is heel bruikbaar bij digitale bundelvorming, een centraal aspect bij moderne radars.

Het ontwikkelen van dubbele-band brede-hoek gefaseerde arrays voor scannen is een onderzoeksprobleem bestaande uit meerdere lagen. Dit vereist om het probleem op te delen in drie hoofd onderzoekrichtingen: 1) het ontwerp van nieuwe dubbele- of meerdere-band array elementen, 2) de ontwikkeling van experimentele prototypes van gefaseerde array concepten met brede-hoek scan mogelijkheden en grote frequentie verhoudingen ($\geq 1.5 : 1$) en 3) de ontwikkeling van technieken om wederzijdse koppeling te reduceren in patch antenne arrays. Geassocieerde aanvullend onderzoek over de invloed van wederzijdse koppeling op het scannen, rooster invloed op koppeling en scannen, invloed van inkorten op impedantie van array elementen en ontwikkeling van meerdere-band antennes voor SatComm applicatie zijn succesvol uitgevoerd.

De grote onderzoek opbrengst kan als volgt worden samengevat. Een nieuwe comb-slot-geladen patch antenne met quasi-magneto-elektrisch radiatie karakteristieken was ontwikkeld voor array applicaties. Er zijn twee sleutel aspecten voor dit antenne ontwerp. Ten eerste, de antenne combineert zowel de elektrisch als magnetisch radiatie karakteristieken in het gehele radiatie mechanisme in een enkele radiatie structuur. Ten tweede, de antenne bevat een nieuwe "lamppost" voeding architectuur, welke ook een mechanisme levert die reactantie balanceert dat helpt bij het behalen van goede bandbreedtes bij operationele banden. De dubbele-band antenne ondersteund een grote frequentie verhouding (1.5:1) en consistente radiatie patronen op beide banden. Gebaseerd op dit antenne concept, experimentele prototypes van beide lineair en planer arrays, operationeel in X-band, zijn ontwikkeld en de performance is gevalideerd. Brede-hoek scannen ($\pm 60^o$) is gedemonstreerd op beide operationele banden met consistente ingebedde element patronen.

Een nieuwe meerdere-band radar en communicatie antenne met extreem weinig lage profiel voor elektrische dimensies is daarna ontwikkeld. Het voorgestelde gekruiste L-staaf antenne heeft nieuwe en flexibele operationele eigenschappen die ondersteuning bieden voor maximaal vier goed afgescheiden operationele banden, voor zowel patch-gelijkend en omni-directioneel radiatie patronen, en inherent resonantie afstel mogelijkheid om te verhogen of onderdrukken van elk benodigde band(en). Experimentele prototypes van dubbele-band lineair en planar arrays met de gekruiste L-staaf antenne, operationeel in X/Ku- en K-banden, zijn ontwikkeld. De gedemonstreerde belangrijkste eigenschappen bevat de grote frequentie verhoudingen (1.8:1), brede-hoek scannen ($\pm 50 - 60^o$) en sub-banden bandbreedtes. De kundigheid van de quad-band antenne versie met ondersteuning voor zowel 'patch-gelijkend' en omnidirectioneel radiatie patronen als zijn extreem lage profiel in elektrisch en fysische dimensies, maakt het aantrekkelijk voor het gebruik in SatComm gebruikers stations.

Ten sloten, een nieuwe dilectrisch-contrast techniek om wederzijdse koppeling tussen nauw plaatst array radiatoren te verminderen is voorgesteld. De methode gebruikt meerdere laags substraten, met permittiviteit contrast tussen de lagen, dat bijdraagt in het verlagen van koppeling. De voorgestelde techniek maakt externe structuren (zoals EBGs) overbodig, waardoor de scanning prestaties van de array ongewijzigd blijven. Bovendien, modale analyse, gebaseerd op het concept van verspreiders, is gebruikt om het verschil in operationele mode karakteristieken tussen de homogene en meerdere laags substraat architecturen te evalueren. The effectiviteit van de voorgestelde techniek is ook geverifieerd met experimentele lineair array prototypes.

Samenvattend, de productie heeft, voor de eerste keer, gedemonstreerd het potentieel en mogelijkheid van dubbele-band gefaseerde arrays met brede-hoek scanning bekwaamheid. De voornamelijk behaalde en hier gepresenteerde resultaten, die aspecten dekken van zowel fundamenteel onderzoek en praktische relevantie, duiden een belangrijk evolutionaire stap aan richting het ontwikkelen van dubbele-band gefaseerde arrays voor toekomstige multifunctionele radar front-ends.

Author's publications

Journals

J1. S. E. Valavan, D. Tran, A. G. Yarovoy, A. G. Roederer, "Dual-band wide-angle scanning planar phased array in X,Ku bands", **accepted** to the *IEEE Transactions on Antennas and Propagations.*

J2. S. E. Valavan, D. Tran, A. G. Yarovoy, A. G. Roederer, "Planar dual-band wide-scan phased array in X-band", **accepted** to the *IEEE Transactions on Antennas and Propagations.*

J3. S. E. Valavan, D. Tran, A. G. Yarovoy, "An effective dielectric-contrast based technique to mitigate mutual coupling between closely spaced patch array radiators", submitted (under review) to the *IET Microwaves, Antennas and Propagations.*

J4. S. E. Valavan, D. Tran, A. G. Yarovoy, "A planar dual-band symmetric comb-slot-loaded phased array antenna", submitted (under review) to the *Electronic Letters.*

J5. S. E. Valavan, D. Tran, A. G. Yarovoy, "Dual-band planar phased array", submitted (under review) to the *IEEE Antennas and Wireless Propagations Letters.*

J6. B. Yang, A. G. Yarovoy, S. E. Valavan, K. Buisman, O. Shoykhethrod, "A Novel 60GHz LTCC differentially-fed UWB antenna for the 60GHz band", *EUMA-International Journal of Microwave and Wireless Technologies (Special Issue on 60 GHz Wireless Communication Systems)*, 2011.

Conference Proceedings

C1. S. E. Valavan, D. Tran, A. G. Yarovoy, "Bandwidth enhancement technique for dual-band phased array antennas", *prepared for submission.*

C2. S. E. Valavan, D. Tran, A. G. Yarovoy, "A dual-band magneto-electric patch antenna for X-band phased array", *submitted to the European Microwave Conference (EuMC/EuMW)* , Oct. 2014.

C3. S. E. Valavan, D. Tran, A. G. Yarovoy, "Linear dual-band phased array in K-band", *submitted to the European Radar Conference (EuRAD/EuMW)*, Oct. 2014.

C4. S. E. Valavan, D. Tran, A. G. Yarovoy, "A dielectric contrast technique for effective mitigation of mutual coupling between dual-band array radiators", *accepted to the European Conf. on Antennas and Propagation (EuCAP)*, Apr 2014 **(short listed for the Best Paper Award)**.

C5. S. E. Valavan, D. Tran, A. G. Yarovoy, "Novel dual-band magneto-electric phased array antenna with low mutual coupling characteristics", *accepted to the European Conf. on Antennas and Propagation (EuCAP)*, Apr 2014.

C6. S. E. Valavan, D. Tran, A. G. Yarovoy, "A planar tri-band phased array antenna", *accepted to the European Conf. on Antennas and Propagations (EuCAP)*, Apr 2014.

C7. S. E. Valavan, M. Simeoni, A. G. Yarovoy, "Scanning performance analysis of linear arrays of printed dual-band patch antennas", *accepted to the European Conf. on Antennas and Propagations (EuCAP)*, Apr 2014.

C8. S. E. Valavan, D. Tran, A. G. Yarovoy, "A novel circularly-polarised quad-band patch antenna for satellite applications", *Proc. of the European Microwave Conference (EuMC/EuMW)*, Oct. 2013.

C9. S. E. Valavan, D. Tran, A. G. Yarovoy, "A novel single layer quad-band patch antenna",*Proc. of the IEEE Antennas and Propagations Symposium (AP-S)*, July 2013.

C10. S. E. Valavan, D. Tran, A. G. Yarovoy, "Grid type vs scanning performance of planar dual-band arrays", *Proc. of the European Conf. on Antennas and Propagation (EuCAP)*, Apr 2013.

C11. S. E. Valavan, M. Simeoni, A. G. Yarovoy, "Impact of truncation on finite-sized linear arrays with dual-band radiators", *Proc. of the European Radar Conference (EuRAD/EuMW)*, Oct. 2012.

C12. S. E. Valavan, M. Simeoni, A. G. Yarovoy, "Comparative analysis of dual-band array radiator interactions in rectangular and triangular grids", *Proc. of the 6th European Conference on Antennas and Propagation (EuCAP), 2012*, vol., no., pp.607-610, 26-30 March 2012.

C13. S. E. Valavan and A. G. Yarovoy, "Performance study of cavity backed dual-band radiators", *URSI-Benelux Workshop*, June 2011.

C14. B. Yang, A. G. Yarovoy, S. E. Valavan, "Novel LTCC UWB 60GHz semi-shielded aperture stacked patch antenna with differential feeding", *Proc. of the European Conf. on Antennas and Propagation (EuCAP)*, March, 2011.

C15. S. E. Valavan, D. Psychoudakis, C. C. Chen, J. L. Volakis, "Low profile top-loaded cone antenna for VHF to UHF operation", *USNC-URSI National Radio Science Meeting*, Jan. 2010.

C16. J. Zhao, S. E. Valavan, C. C. Chen, J. L. Volakis, "Compact 11-Ellipse inverted hat antenna for UWB operations", *Proceedings of AMTA*, Sept. 2009.

C17. S. E. Valavan, B. Yang, A. G. Yarovoy, L.P. Ligthart, "Stacked patch UWB antenna in LTCC technology", *Proc. of the European Conf. on Antennas and Propagations (EuCAP)*, April, 2009.

C18. S. E. Valavan, B. Yang, A. G. Yarovoy, L.P. Ligthart, "An M-band differentially fed, aperture coupled stacked patch antenna in LTCC", *Proc. of the European Microwave Week Radar Conference (EuMW-EuRAD)*, Oct, 2008.

C19. A. Nezirovic, S. E. Valavan, S. Tesfay, A. G. Yarovoy, "Experimental study on human breathing cross section using UWB impulse radar", *Proc. of the European Microwave Week Radar Conference (EuMW-EuRAD)*, Oct, 2008.

Awards and Grants

EuMA student grant - *EuMC*, October 2013.

EuMA student grant - *EuRAD*, October 2008.

Vita

Shenario Ezhil Valavan (*Aged: 28*) is from Madras, India. He completed his B.E. (*Electronics and Communications*) from Anna University, Madras, and M.S. (*Electrical Engineering*) from the Delft University of Technology, Netherlands, in June 2006 and April 2008 respectively. In 2009, he spent a year as a graduate research associate (GRA) at the Ohio State University - Electroscience Lab, Columbus, Ohio, USA, working on low-profile ultra-wideband antennas. He was a doctoral student from 2010-2013 at the Delft University of Technology, focussing on the design and development of dual-band active phased arrays, within the framework of the STARS project. His primary research interests include phased arrays, radar systems, ultra-wideband, multi-band and SatComm antennas and digital beamforming. He is also a keen amateur radio astronomer and has strong interests in Tamizh literature and political economics.

Acknowledgements

I express my first, sincere and heartfelt thanks to Prof. Alex Yarovoy, my doctoral advisor and promoter. In particular, for making sure that my professional transition from the United States went smoothly. I thank him for providing me with the independent space and his confidence in my ability, both of which enabled me to develop well as a researcher. A special thanks to the STARS consortium for supporting the research throughout.

My next thanks is to Mr. Dani Tran (TU-Delft) for all his help and support, enhancing my technical understanding and positively contributing to the definition of my research. My sincere thanks to Dr. Antoine Roederer for providing lots of insights and sharing his experiences and knowledge with me. I quite enjoyed and learned a good deal through this association and the numerous technical discussions. Dr. Massimiliano Simeoni (ESA/ESTEC) deserves my thanks for his support and technical insights, especially during his time at Delft. A special thanks to Prof. Francois Le Chevalier for sharing his radar expertise, advices and feedback. I also wish to mention Prof. Leo Ligthart (TU-Delft) and Prof. Prabhakar Pathak (Ohio State) for the timely help and guidance offered when I needed them the most.

I wish to thank my committee members, Prof. Piet van Genderen, Prof. Guy Vandenbosch, Prof. Andrea Neto, Prof. Bart Smolders and Prof. Peter Hoogeboom for their meticulous reviews and support.

Pascal Aubry deserves a friendly and sincere thanks for his help with the chamber measurements, and more so, for his company. I would also like to thank my office mates Alexey, Teun and Fotios and my other colleagues Penkin, Sharavan and Takuya, for all the discussions, company and lighter moments which we've shared. A note of thanks to Yann and Francesco for the template and the patient answers to my numerous questions, saving me a lot of time.

Finally, I would like, in the most special way, to thank Sathya, Josphine Amma, Amudhan, Amalraj and my family and close friends for always being there for me. The understanding, support and appreciation which Sathya has provided need a special mention. I'm extremely glad to have her with me in this journey called life. Josphine

Amma, who has been, and continues to be, the bedrock for all my accomplishments. I consider myself very fortunate and privileged to have these two ladies in my life, who have not only supported me unconditionally, but also, during many instances, inspired and have shaped my life as well.

I would like to invoke a note from the ‘divine poet’ Thiruvalluvar, which sums up the quest for knowledge.

தொட்டனைத் தூறு மணற்கேணி மாந்தர்க்குக்
கற்றனைத் தூறும் அறிவு